DEPARTMENT OF MECHANICAL ENGINEERING

Selective permeability properties of a basal lamina model system

a thesis

presented by

Fabienna Arends

TECHNISCHE UNIVERSITÄT MÜNCHEN

Fakultät für Maschinenwesen

Professur für Biomechanik

Selective permeability properties of a basal lamina model system

Fabienna Arends

Vollständiger Abdruck der von der Fakultät für Maschinenwesen der Technischen Universität München zur Erlangung des akademischen Grades eines

Doktors der Naturwissenschaften (Dr. rer. nat.)

genehmigten Dissertation.

Vorsitzender: Univ-Prof. Dr. Wolfgang A. Wall

Prüfer der Dissertation:

1. Univ-Prof. Dr. Oliver Lieleg
2. Univ-Prof. Dr. Friedrich C. Simmel

Die Dissertation wurde am 27.08.2015 bei der Technischen Universität München eingereicht und durch die Fakultät für Maschinenwesen am 16.12.2015 angenommen.

Summary

Biological filters establish a selective permeability towards the passage of beneficial and harmful molecules in the human body. One example for such a selective filter is the vascular system consisting of a cell layer, the endothelium, and a thin extracellular matrix at the basolateral side of the endothelium, the basal lamina. This matrix separates the underlying cells from the connective tissue, mechanically supports the cells and passes signals bidirectionally between the endothelium and the connective tissue. Moreover, the basal lamina serves as a molecular filter for compounds passing from the blood stream into the connective tissue and vice versa. Despite the important function of the basal lamina for the body, the detailed physical mechanisms responsible for this selectivity are still not fully understood. An in-depth knowledge about the barrier function would help to design drug carriers which either harness or avoid binding interactions with the basal lamina.

In this thesis, commercially available basal lamina gels were analyzed to explore both, the physical interactions and the basal lamina components participating in the selective filtering process. First, particle diffusion studies with uncharged polystyrene particles were performed in those gels. The diffusion experiments showed that the mesh size, which sets the size cutoff for particles passing through those basal lamina gels, depends on the concentration of the crosslinking molecule entactin. In another set of diffusion studies performed at high salt concentrations, it was shown that a combination of hydrophobic and electrostatic interactions is responsible for the trapping of charged polystyrene particles. Moreover, the mobilization of trapped particles was dependent on the salt concentration as well as on the salt species. In addition, transient binding events of the polystyrene particles to the basal lamina gels were observed at high ion concentrations in combination with two distinct types of binding to the network: weakly bound and strongly bound particles where a strongly bound state was attributed to the simultaneous binding of the particles to several filaments of the network. A microfluidic setup was designed to test the diffusive transport of molecules from a buffer compartment into the basal lamina. It was shown that positively charged molecules accumulated at the basal lamina/buffer interface whereas for negatively charged molecules of equal size no such behavior was observed. Moreover, the height of the accumulation peak depended on the amount of positive charge present on the molecules. These findings were reproduced by a simple diffusion-reaction model in which molecules were able to transiently bind to the gel with high and low affinity, respectively. The simulations showed that the height of the accumulation peak was set by the binding affinity of the molecules to the gel. In a last step, the diffusive spreading of the test molecules in an *in vivo* tissue were compared to the results obtained in the microfluidic chip. It was verified that the *in vitro* test setup correctly reproduces key results obtained from *in vivo* experiments in the cremaster muscle of living mice.

The findings presented here extend our understanding of the physical mechanisms underlying the selective permeability of the basal lamina. In the future, this might help to design new drug carriers with surface modifications which allow them to interact with the basal lamina in a desired way and to test these new designs in a microfluidic setup which reproduces key results from *in vivo* experiments.

Content

1 Introduction

In the human body, complex barriers prevent the entrance and distribution of foreign compounds such as bacteria, viruses and other pathogens. These barriers include the skin, the oral cavity, the gastrointestinal tract, the blood-brain-barrier, and the vascular system [1-6]. The skin is one of the largest and in most cases the first barrier for compounds from the outside. The outer layer of the skin, the epidermis, consists of several layers of epithelial cells and comprises a physical as well as a chemical/biochemical barrier [1]. The basal cell layer of the epidermis is coated by a thin extracellular matrix (ECM), the basal lamina, which sets the borderline to the connective tissue of the dermis [7]. In addition to the protective function of the skin, it also has a regulatory function: the skin allows for uptake of oxygen and prevents the loss of water from the underlying tissue [1]. Another example for a complex biological barrier in the human body also comprising a cell and a basal lamina layer is the blood-brain-barrier [5]. The blood-brain barrier protects the brain tissue from pathogens and neurotoxic molecules whereas it allows the passage of other molecules such as hormones from the blood stream into the cerebrospinal fluid [8]. To show such a selectivity towards molecules, i.e. deciding which of them are allowed to pass and which are rejected from passing, an advanced molecular filter is needed. Most molecules are excluded from the surrounding extracellular space by the tight junctions between the endothelial cells which line the inner side of the blood vessels [8]. If the tight junctions between the cells are impaired, the basal lamina becomes directly accessible for blood compounds. A similar structure is present in the vascular system. Here, the first barrier is set by endothelial cells which are again coated by a thin layer of basal lamina [7]. In the vascular system, the passage of beneficial molecules such as nutrients, growth factors, proteins, hormones or polysaccharides from the blood stream into the connective tissue is mostly regulated by the endothelial cells [6,9,10]. However, for molecules entering from the connective tissue into the blood stream, first the basal lamina is encountered before they reach the endothelial cells. Although these barriers are found at different locations in the body, they all share a common structure: a cell layer, either endothelial cells or epithelial cells, coated by the basal lamina.

The basal lamina is a thin matrix located at the basolateral side of the epithelium or the endothelium, thus separating these cells from the surrounding connective tissue [7]. The basal lamina consists of different types of biopolymers, most of them are secreted by the underlying cells [7]. The main constituents of the basal lamina are laminin, collagen IV, perlecan, and entactin (nidogen) [11,12]. Laminin is a protein mainly found in basement membranes such as the basal lamina and it is composed of three polypeptide chains: α-chain, β-chain and γ-chain. The three chains assemble into a cross-like structure as illustrated in Figure 1. Laminin self-assembles into a sheet-like structure which is anchored to the underlying cell layer via integrin interactions [13,14]. Collagen IV is a type of collagen mostly found in the basal lamina and it assembles similar to collagen I into a helix [15]. Type IV collagen also self-assembles into a sheet-like structure but has no direct interaction with laminin. Both, laminin and collagen IV, bind perlecan as well as entactin (nidogen) which both act as crosslinkers between the two sheet-like structures (Figure 1), thus building the complex structure of the basal lamina [16].

In addition to the task of building a complex structure and to anchor itself to the underlying cell layer, all of these basal lamina components fulfill tasks concerning the fate of the cells: laminin,

in combination with collagen IV supports cell attachment, differentiation, migration and growth [17]. It was suggested that type IV collagen and laminin together with fibronectin are involved in the formation of tight junctions [18]. Both, laminin and collagen IV also maintain the mechanical stability of the basal lamina [7]. The proteoglycan perlecan consists of a core protein at which heparan sulfate (HS), a heavily charged glycosaminoglycan, is attached. In addition to the function as a crosslinker between laminin and collagen IV, perlecan and in particular the heavily charged HS chains act as a molecular filter and are responsible for the hydration of the matrix [19-21].

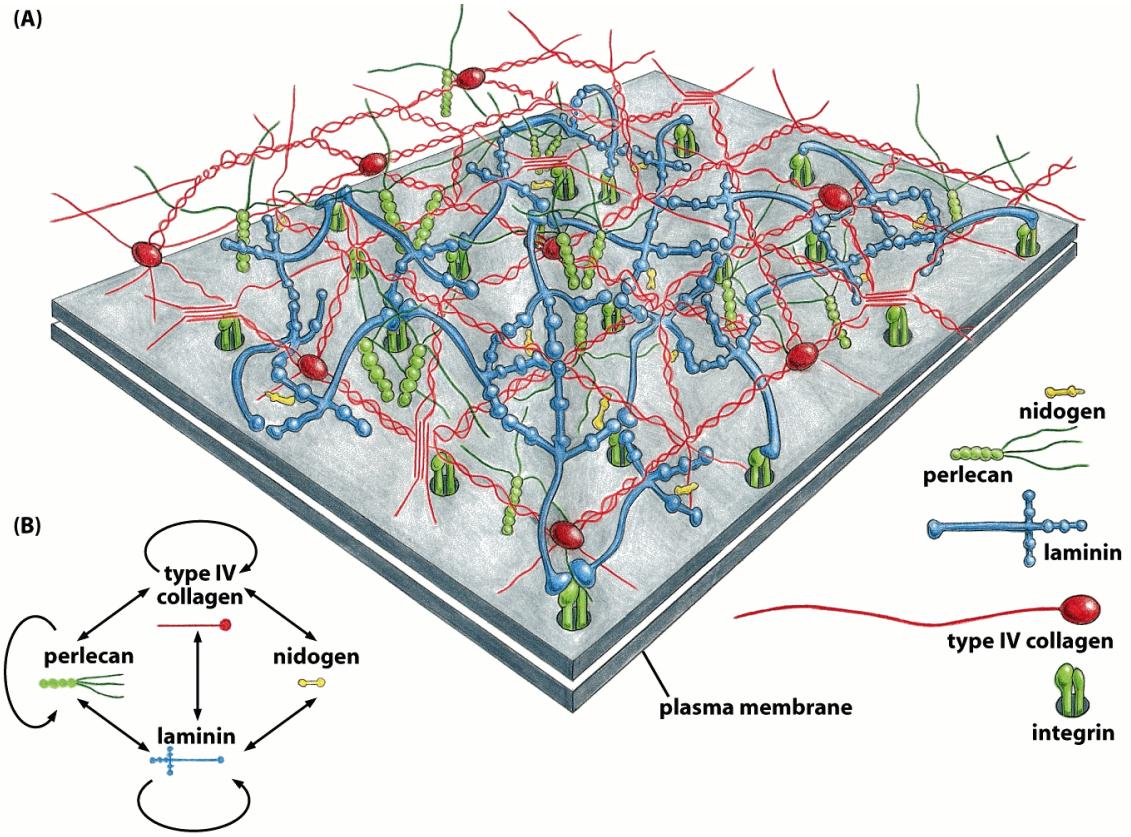

Figure 1. (A) Molecular structure of the basal lamina: The main components are laminin, collagen IV, perlecan, and entactin (nidogen). (B) Collagen IV and laminin self-assemble into networks which are connected via entactin and perlecan. Laminin also binds to integrins which are anchored in the plasma membrane. Figure taken from [7] with kind permission of Garland Science.

Despite the important function of the basal lamina for the body, the physical mechanisms responsible for the selectivity of this extracellular matrix still remain largely unknown. A detailed knowledge of those interactions are in particular interesting for the design of new drug carrier vehicles. Advanced drug delivery uses drug carrier vehicles instead of the direct administration of drugs. Those drug carriers have several advantages over the direct application of drugs: First, the drug carriers embed the drug and protect it from the surrounding body environment such as the gastric acid and blood compounds. Thus, the drug carrier ensures that the drug is not directly degraded by the body and, additionally, that the drug does not affect the body on the route to the intended site [22]. Second, an advantage of drug carriers over the directly applied drug is that

drug carriers can exhibit other physical and chemical properties than the drugs which are incorporated. As an example, drug carriers can possess a hydrophilic surface whereas the drugs embedded in the drug carrier can be hydrophobic. This can results in a faster uptake of the drug carriers compared to the drug alone. In some situations it might be advantageous to have a stable drug concentration over time instead of a concentration peak, e.g. directly after application. This can be realized by designing drug carriers with prolonged drug release [23]. However, the drug carrier is, depending on the route of administration, still present in the whole body and can interact with various body parts. Thus, the next step in the design of drug carriers is to target only specific regions of the body whereas all other regions are unaffected by the drug carriers. This is also referred to as targeting drug delivery. There are several questions which have to be asked when drug carriers should be designed for targeting drug delivery [24]: Which route of administration is chosen? Which drug should be embedded? What is the tissue of interest? Which body barriers have to be passed?

One example for targeting drug delivery is the specific targeting of tumors. Drug carriers are often injected intravenously, thus the vascular system is the barrier which the drug carriers have to pass. Here, the passage of drugs/drug carrier vehicles from the blood stream into the adjoining tissue is primarily regulated by the endothelial cells. However, in most cases the endothelium around tumors is leaky as sketched in Figure 2. This is also known as enhanced permeability and retention effect (EPR) [25-27]. Since the barrier function of the endothelium is impaired by the tumor, the basal lamina is directly accessible for compounds from the blood stream. In such a scenario, the passage of drug carrier systems and their incorporated drugs is regulated by the basal lamina. The basal lamina becomes even more important in tumors since they usually show an increased production of ECM [28].

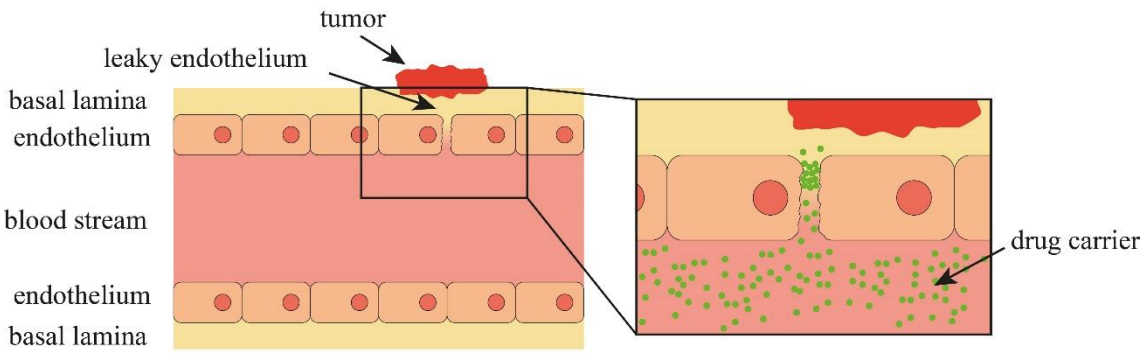

Figure 2. Schematic representation of a leaky endothelium. The tight junctions between the endothelium cells are opened due to a tumor in the vicinity of the blood vessel. This allows compounds from the blood stream such as growth factors, proteins and hormones to enter into the adjacent tissue. This also opens a route for drug carriers which are supposed to treat the tumor.

To efficiently pass the basal lamina barrier the physical interactions between drug carriers and this complex multi-component ECM need to be known. Possible physical interactions include steric hindrances, electrostatic interactions, hydrophobic interactions or specific binding motifs. The following parameters of the drug carriers can be tuned during their production to overcome or to promote interactions with the basal lamina: the choice of the material, the size, the shape, and the surface modifications of the particles [29]. To efficiently tune these parameters, the detailed physical mechanisms responsible for the interactions as well as the basal lamina

components which play a role need to be identified. The easiest type of interaction to overcome are steric hindrances imposed by the mesh size of the basal lamina. Here, the size of the drug carrier must be adjusted to be smaller than the mesh size. Electrostatic interactions can be prevented by a passivation of the particle surface groups. In most cases this is realized by binding polyethylene glycol (PEG) to the surface of the drug carrier. If electrostatic interactions are meant to harness, charged groups can be deposited on the particle surface. Similarly, specific binding molecules can be introduce which bind to certain motifs of the basal lamina. Hydrophobic interactions can be prevented by hydrophilic surfaces or surface modifications of hydrophobic drug carriers. For this, also a PEGylation of the particle surface is employed. Thus, there are ways to circumvent electrostatic and hydrophobic interactions, nevertheless an in-depth knowledge about the basal lamina components which constitute the electrostatic or hydrophobic interactions together with the strength of these interactions will result in various new design possibilities for drug carrier vehicles.

To evaluate the sort of interactions together with the strength of the interactions *in vivo* testing is not feasible. In addition to the parameters of interest, there are a wealth of other parameters which are in part unknown or impossible to influence from the outside. This makes the analysis of experiments conducted *in vivo* very hard. Furthermore, to evaluate the strength of an interaction, particles with only slight differences have to be tested in a systematic manner. Doing this *in vivo* would result in hundreds to thousands of animals needed to perform the tests. Thus, the life of many animals would be sacrificed only to study one parameter. In contrast, a robust *in vitro* setup which correctly predicts the *in vivo* outcome can be employed to conduct thousands of experiments without the ethical problems associated with animal tests. The first challenge for such an *in vitro* setup is to model the tissue of interest. The preferable way would be to purify the tissue from the organism one is interested in. For the basal lamina a well-established model system is an extracellular matrix purified from the Engelbreth-Holm-swarm sarcoma [30,31]. It was shown that this ECM maintains its biological activity and promotes cell adhesion, differentiation and migration [32]. Experiments with this ECM gels, conducted in a bulk setting showed that the mesh size of this gel is in the order of micrometers [33]. Another set of experiments showed that ECM gels show a high selectivity for nanoparticles based on their charge. Heparan sulfate was identified to mediate the selectivity towards positively charged polystyrene particles [33]. Until now, the ECM component responsible for the trapping of positively charged particles remains unknown as well as the screening for other physical interactions, such as hydrophobic interactions.

The second challenge for such an *in vitro* setup is to match the *in vivo* environment: the diffusive entry of particles into the ECM at the interface between the basal lamina and a liquid phase (such as the blood stream) cannot be characterized in the bulk experiments mentioned above. In addition to the diffusion behavior of nanoparticles also the spreading of encapsulated drug molecules, once they are released, is of great interest [34]. One promising approach for the realization of such predictive *in vitro* experiments is microfluidics [35,36]. There are already a broad range of experimental settings in which such an approach is used, e.g. for the design of a cardiac tissue model [37], for the investigation of nanoparticle translocation across a permeable endothelium [38] or through a endothelial/epithelial double layer simulating the biological interface in alveoli [39]. Those chips are able to reproduce key results obtained in living tissue in an *in vitro* setting although their setup is strongly simplified: to date, most of those microfluidic penetration assays mainly focus on the barrier function of the cell layer and neglect the influence of the adjacent

biopolymer matrix. This is partly due to the fact that it is technically challenging to deposit a soft biopolymer gel on a microfluidic chip in such a way that a stable gel/liquid interface is generated which can be used for a penetration experiment. First realizations of such a molecular penetration experiment with a biopolymer gel have been achieved for mucin gels [40,41], but are still lacking for other gels such as the basal lamina.

The following key questions are tackled in this thesis:

- How does the molecular composition of basal lamina gels influence the biophysical properties of the gels?
- Are there, in addition to electrostatic interactions, other physical interactions responsible for the trapping of nanoparticles?
- Are the same selective properties obtained, when nanoparticles are substituted by molecules with an approximated size of a few nanometers?
- Are there differences between the in-bulk diffusion of test molecules and their diffusive transport across an interface?
- Do results obtained with a simplified *in vitro* microfluidic setup successfully predict the outcome of *in vivo* experiments?

In Section 4.1 of this thesis, the biophysical properties of basal lamina gel preparations obtained from four different suppliers are used as a platform to investigate how these properties depend on the biochemical composition of the gels. The motility of differentiated HL-60 cells in those gels are analyzed, the Brownian motion of nanoparticles in the gel and the viscoelastic properties of the gels are quantified, and their biochemical constitution and microstructure are compared. Although all gel variants tested have been purified from the same tumor tissue of mice, strong differences in the gel properties ranging from decreased permeability to increased stiffness and mild cytotoxic behavior are detected. Those differences in the gel properties can be traced back to small variations in the molecular composition of the gel preparations which lead to differences in the gel architecture.

In Section 4.2, it is demonstrated that a combination of generic electrostatics and ion-specific interactions gives rise to an efficient but tunable immobilization of colloids in basal lamina hydrogels. It is shown that if the interaction strength between the colloids and the gel is sufficiently weakened by increasing the salt concentration of the hydrogel buffer, transient escape events of trapped particles occur on a time scale of several seconds. As a consequence, a particle ensemble can be divided into two general subsets: either mobile or immobile particles. Quantitative parameters obtained from the mean squared displacement (MSD) confirm this classification. It is further shown that the trapping efficiency of colloids depends not only on the ion concentration but also on the ion species demonstrating the relevance of ion-specific effects for the hydrogel permeability.

In Section 4.3, a microfluidic assay for the quantification of the diffusive transport of molecules across basal lamina interfaces is presented. The penetration efficiency of different fluorescent molecules such as dextrans with different molecular weights and net charges as well as customized peptides are analyzed. In this microfluidic setup, those molecules accumulate at the gel/buffer interface in a charge selective manner in full agreement with model calculations considering transient binding of molecules to the gel components. *In vivo* microinjection experiments conducted in mice show a similar charge selective accumulation of those molecules

around blood vessels and a colocalization with collagen IV, a key component of the basal lamina. Thus, the *in vitro* setup presented here successfully predicts the selective transport of molecules across this biological barrier.

2 Material

2.1 Basal lamina

To conduct predictive *in vitro* experiments the *in vivo* situation should be modeled as closely as possible. Accordingly, it is best to use materials purified from the site of interest. In this thesis, the focus lies on the permeability properties of the basal lamina. Therefore, a model system for native basal lamina gels is needed. Since the basal lamina constitutes only a very thin sheet of a few hundred nanometers *in vivo*, it is very challenging to purify this matrix at reasonable amounts. However, the Engelbreth-Holm-Swarm sarcoma in mice is known for a high production of ECM which led to the commercial purification of ECM from this tumor according to the protocol established by Kleinman [31,32]. This commercially available ECM contains approximately 56 % laminin, 31 % collagen IV and 8 % entactin[1] which is close to the fractions found in native basal lamina. In addition to matching the composition compared to native basal lamina also the biological activity is maintained: cells cultured in this ECM show enhanced proliferation and differentiation compared to normal cell culture or when collagen is used as a matrix [42].

2.1.1 ECM comparison

ECM purified according to Kleinman's protocol [31,32] can be bought by several vendors. However, contradictory results are obtained depending on which supplier is chosen. This motivated the first part (Section 4.1) of this thesis in which growth factor reduced ECMs from the following four suppliers were used: Sigma-Aldrich (ECM1), BD Bioscience (ECM2), Trevigen (ECM3) and Life Technologies (Invitrogen) (ECM4). The protein concentration of the ECMs was matched to 3.5 mg/mL by dilution with Iscove's Modified Dulbecco's Medium (IMDM, PAA Laboratories GmbH, Pasching, Austria). A second batch of ECM2, ECM3 and ECM4 was used to check the experimental outcome. However, no second batch of ECM1 was available. Thus, a non-growth factor reduced gel from the same vendor was used to reproduce the experimental results except the cell migration studies, since the additional growth factors may influence the outcome of this experiment and it would not be comparable to the results obtained before.

2.1.2 *Ion-specific effects*

The second study (Section 4.2) did not include cells and was based on a study conducted before [33]. Accordingly, the same ECM vendor, Sigma-Aldrich, was here chosen. For the experiments, the ECM was thawed on ice and afterwards diluted 1:1 with MEM-α (Minimum Essential Medium Alpha, Invitrogen, Karlsruhe, Germany; salt content: 117 mM NaCl, 26 mM $NaHCO_3$, 5 mM KCl, 1.8 mM $CaCl_2$, 0.8 mM $MgSO_4$; pH 6.8) to a final protein concentration of 4.3 mg/mL. The ionic strength was adjusted with different salts as indicated in the individual experiments. The addition of high amounts of salts can lead to a change of pH which could change the properties of the gel. Therefore, the pH was checked after the addition of the various ions but no significant change was observed. Moreover, macrorheological tests showed that the gelation of ECM was not impaired by the ionic conditions used here and the structural integrity of the sample was inspected by phase contrast microscopy. To induce gelation, all samples were incubated at their final protein concentrations in presence of the respective test particles at 37°C

[1] According to the manufacturer's information

for 30 min. For all ionic conditions tested here, it was ensured that no increased particle aggregation compared to low-salt conditions occurred.

2.1.3 *Microfluidics*

For the microfluidics study in Section 4.3, growth factor reduced ECM was again obtained from Sigma-Aldrich at a protein concentration of 7.37 mg/mL. This choice was made since the permeability properties of this gel variant towards polystyrene particles and liposomes have been investigated in this ECM before [33,43,44]. Prior to the experiments, the ECM was thawed on ice for several hours. It was used undiluted since a high mechanical strength is advantageous when buffer is filled into the chip perpendicular to the gel (see Section 3.5 for more details). A volume of 2 µL was inserted into the microfluidic device through inlet 1 (see Figure 5) by carefully pipetting with a pipette having a volume range from 0.1µL to 2.5 µL. This pipette has a high piston stroke length which facilitated the proper filling of the channel.

2.2 Test particles and molecules

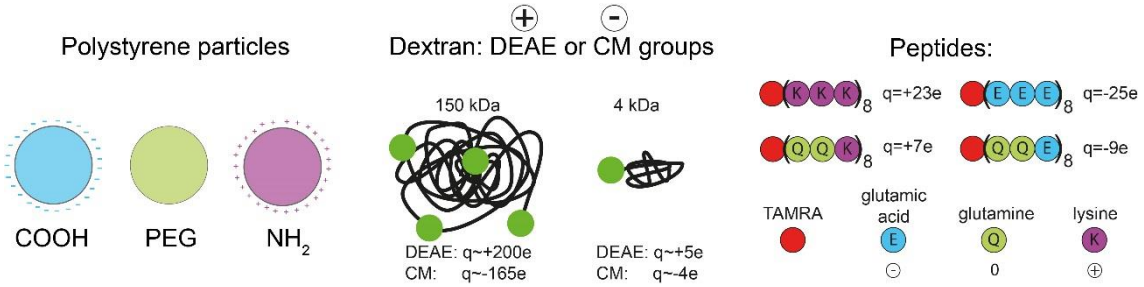

Figure 3. Three different sorts of test particles were used: Polystyrene particles, dextrans (glucose units illustrated in black, FITC molecules indicated in green) and peptides. The net charge given for the molecules is a theoretical estimation.

Throughout this thesis the diffusion of test particles and molecules was studied. As test particles fluorescent polystyrene beads with distinct surface properties were used. Those particles have a size on the order of a few hundred nanometers which makes them suitable for single particle tracking (see Section 3.2). With this method diffusion coefficients of single particles are obtained and local differences in the diffusion of those particles can be quantified. In contrast, dextrans and peptides have a Stoke's radius of only a few nanometers which enables them to diffuse faster than the polystyrene particles and also enter into regions which are inaccessible for the large particles. The peptides are customized such that the amino acid sequence was given by the customer which results in a detailed knowledge about the charge density and the charge distribution of the peptides whereas both is unknown for the polystyrene particles. Since both, dextrans and peptides, are very small single particle tracking is not applicable and only an ensemble averaged diffusion coefficient can be obtained.

2.2.1 Test particles for the ECM comparison

In Section 4.1, positively charged, negatively charged and neutral particles were used to determine differences in the diffusion behavior depending on the particle charge. Since the mesh size of ECM1 was determined to be 1-2 µm [33], 200 nm-sized fluorescent polystyrene latex particles were used for the single-particle tracking experiments. The particles were obtained from

Invitrogen. It was not possible to obtain neutral (PEGylated) particles commercially, thus a polyethyleneglycol (PEG, M_w = 750 Da, Rapp Polymere, Tübingen, Germany) coating of the carboxyl-terminated beads was performed using a carbodiimide-coupling protocol [45]: the bead suspension was vortexed and sonicated for several minutes. A volume of 100 µL of the particle suspension was centrifuged for 20 min at 5000 x g (Biofuge fresco, Heraeus, Hanau, Germany). The supernatant was discarded and the pellet was resuspended with 400 µL ultrapure water. Resuspension was performed by pipetting, vortexing und sonication until all aggregates vanished. Centrifugation and resuspension was repeated twice. The last resuspension was performed with ultrapure water containing 50 mM PEG and 100 mM N-hydroxysulfosuccinimide (Sigma-Aldrich). At the same time 600 µL borate buffer (50 mM boric acid and 36 mM sodium tetraborate, pH 8.5) containing 60 mM 1-ethyl-3-(3-dimethylaminopropyl)carbodiimide hydrochloride (EDC, Sigma-Aldrich) was prepared and added to the resuspended beads. After rotation for 4 h at room temperature the suspension was centrifuged for 20 min at 5000 x g. The supernatant was discarded and the pellet was resuspended with 1 mL ultrapure water by pipetting, vortexing and sonication. This was repeated twice and for the last resuspension only 100 µL were used to obtain the original particle concentration. Successful PEGylation was verified by zeta-potential measurements (see subsection 3.1 for details).

2.2.2 Particles used for studying ion-specific effects

In the study described in Section 4.2 fluorescent latex beads with carboxyl surface groups (negatively charged) and amine surface groups (positively charged), respectively, and a size of 300 nm were obtained from Magsphere (Pasadena, CA).

2.2.3 Test molecules used in the microfluidic setup

For the experiments conducted in the study described in Section 4.3 macromolecules were used to test the diffusive transport across a basal lamina interface. Two types of macromolecules were used: dextrans and custom-made peptides.

Table 1: Properties of the dextrans based on supplier information. All numbers given are estimates based on the molecular structure, average labeling density and pKa of the CM- and DEAE-groups, respectively.

Name	approx. number of glucose units	approx. number of FITC molecules	approx. number of CM- and DEAE-groups, respectively	maximum charge at neutral pH [e]
CM 4 kDa	22	1	3	-4
CM 150 kDa	825	3-4	161	-165
DEAE 4 kDa	22	1	6	+5
DEAE 150 kDa	825	3-4	196	+200

Dextrans are polysaccharide chains with glucose as a repeating unit. To evaluate the diffusive transport of dextrans by fluorescence microscopy a fluorescent label is attached randomly to glucose units at a ratio of 0.001-0.008 mol per mol glucose. To investigate if the size of the dextrans influences the diffusive transport, two different molecular weights of dextrans were used: 4 kDa (Stoke's radius of ~ 1.4 nm) and 150 kDa (Stoke's radius varies from ~ 5 nm to 8.5 nm

depending on the method used to determine the size). In addition to the influence of dextran size on the diffusive transport also the influence charge has on the diffusion of the dextrans is investigated. Glucose itself does not carry any charge but it can be modified by adding charged groups such as diethylaminoethyl (DEAE) and carboxymethyl (CM) to the glucose units. Both types of charged dextrans were obtained from Sigma-Aldrich and the content of charged groups amounts to 2-5 % for DEAE and 3-7 % for CM. The number of glucose units and also the maximum charge for these dextrans are listed in Table 1. For the diffusion studies dextrans were dissolved in PBS at a concentration of 10 mg/mL.

Dextrans are a convenient platform to screen if there are differences in molecular diffusion in dependence on molecule size and charge. However, for a detailed investigation dextrans are not suitable since their individual properties are not well enough defined: the molecular weight as well as the label extend and the percentage of charged groups are only average values which makes it hard to pinpoint the exact interaction responsible for the behavior observed in the experiments. The smaller 4 kDa dextrans have the same charge density as the larger dextrans which results in a lower net charge, but they also have less fluorescence molecules. Differences in the behavior of 4 kDa and 150 kDa dextrans are difficult to interpret because it is unclear if the size, the absolute charge or both are responsible for the observed behavior. The analysis of the experiments is performed by comparison of the fluorescence intensity (see Section 3.6 for more details) which is also complicated when the amount of fluorescent molecules differs. To fill this gap peptides of identical length and with a customized sequence were obtained from PEPperPRINT (Heidelberg, Germany). The length of the peptide was chosen to match the molecular weight of the 4 kDa dextrans which leads to a peptide consisting of 24 amino acids. The diffusive transport of the peptides is evaluated by fluorescence microscopy, thus a carboxytetramethylrhodamine (TAMRA) label was added to the N-termini of the peptides. In total four different peptides were designed: highly negatively charged, highly positively charged, moderate negatively charged, and moderate positively charged peptides. The corresponding amino acid sequences are: TAMRA-$(EEE)_8$, TAMRA-$(KKK)_8$, TAMRA-$(QQE)_8$ and TAMRA-$(QQK)_8$. Here, E is the 1-letter abbreviation of glutamic acid, K stands for lysine and Q is glutamine. Glutamic acid has a molecular weight of 147.13 g/mol and the free side chain carboxylic acid group has a pKa of 4.1. This results in a negatively charged group at physiological pH as used in the experiments. Lysine has a molecular weight of 146.19 g/mol and the pKa of the side chain amino group is 10.5, thus it is positively charged at neutral pH. Glutamine has a molecular weight of 146.15 g/mol and a zwitterionic side chain. It was therefore assumed to be net neutral at pH 7. More details can also be found in Table 2. For the experiments, the peptides were dissolved in PBS and used at a concentration of 1 mg/mL.

Table 2: Properties of peptides used in the study. The charge was calculated assuming that all carboxyl- and amine-groups are charged.

Name	molecular weight [kDa]	fluorophore type, fluorophore charge [e]	maximum charge [e]
$(KKK)_8$	4	TAMRA, 0	+23
$(QQK)_8$	4	TAMRA, 0	+7
$(EEE)_8$	4	TAMRA, 0	-25
$(QQE)_8$	4	TAMRA, 0	-9

3 Theoretical background and methods

3.1 Debye screening length and zeta potential

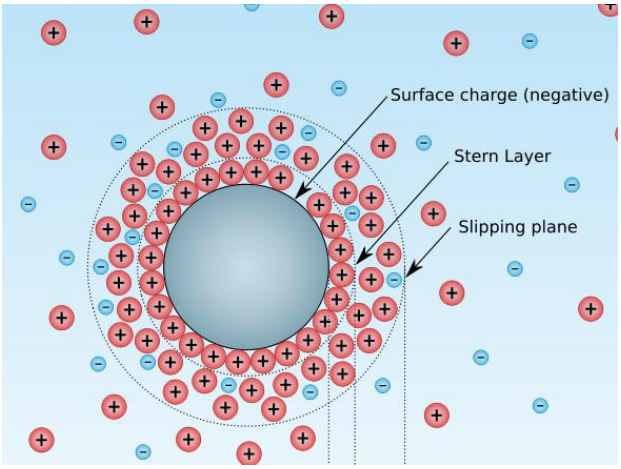

Figure 4. Illustration of the Stern model[2]: A negatively charged particle adsorbs positively charged ions from the electrolyte (Stern layer). Adjacent, a diffusive layer according to the Gouy-Chapman model is located. If the particle is moved by an external electric field, the ion cloud moves with the particle. The border at which ions stop following the particle movement is defined as the slipping plane.

The following theoretical part follows the book of Hunter [46], where a more detailed discussion can be found.

For a quantitative evaluation of electrostatic interactions between particles and the ECM, the surface charge or the surface potential of the particles should be known. However, both parameters are not directly accessible for the particles used here. Moreover, the particles are suspended in a solution containing ions which screen the charge of the particle surface. Several models have been developed to describe the screening process by counterions mathematically. The first model introduced by Helmholtz assumes a double layer consisting of a layer of fixed charges at the surface, such as electrons, followed by a monolayer of fixed counterions. This model results in a linear decrease of the surface potential with the distance. However, the assumption of a fixed double layer is very strict and neglects diffusion and mixing of ions. An improved model, introduced by Gouy and Chapman, assumes a diffusing double layer. This assumption leads to the Poisson-Boltzmann equation. For small potentials (Debye-Hückel approximation):

[2] "Diagram of zeta potential and slipping planeV2" modified and converted to SVG by Mjones1984. Original work by Larryisgood. - Modified image based upon http://en.wikipedia.org/wiki/File:Zeta_Potential_for_a_particle_in_dispersion_medium.png by Larryisgood. Licensed under CC BY-SA 3.0 via Wikimedia Commons - http://commons.wikimedia.org/wiki/File:Diagram_of_zeta_potential_and_slipping_planeV2.svg#/media/File:Diagram_of_zeta_potential_and_slipping_planeV2.svg

$$\psi < \frac{k_B T}{ze} \tag{1}$$

the exponential function of the Poisson-Boltzmann equation can be linearized and the differential equation can be analytically solved. Here, ψ is the potential at the particle surface, k_B the Boltzmann constant, T the temperature in Kelvin, e the elementary charge, and z the valency of the ions in solution. For monovalent ions at room temperature the potential has to be smaller than 25.7 mV to fulfill the assumption of small potentials. Both models, the Helmholtz and the Gouy-Chapman model, have been combined by Stern resulting in a model which allows some ions to adhere at the interface giving rise to a Stern layer whereas some form a diffusive layer according to the Gouy-Chapman model (Figure 4). This results in a linear decrease of the surface potential over the Stern layer (Helmholtz model) and then turns into an exponential decrease with the Debye screening length as characteristic length. The Debye screening length is given by:

$$\lambda_D = \sqrt{\frac{\varepsilon_r \varepsilon_0 k_B T}{N_A e^2 \sum c_i z_i^2}} \tag{2}$$

Here, ε_r is the dielectric constant of the medium, ε_0 is the permittivity of vacuum, k_B the Boltzmann constant, T the temperature in Kelvin, N_A the Avogadro constant, e the elementary charge, c_i the concentration of ion i in mol/L and z_i is the valency of ion i. There are only three parameters in this equation which can be influenced from the outside: the temperature, the concentration and the sort of ions used. Since the temperature is given in Kelvin, huge temperature changes are needed to noticeably affect the Debye screening length. That leaves the concentration as well as the valency of the ions as parameters to tune the screening length. It should be noted that the valency contributes quadratically whereas the concentration of the ions contributes only linearly to the ionic strength. Thus, for some experiments where efficient charge screening is desired, it might be advantageous to e.g. substitute Na^+ ions by Ca^{2+} ions instead of increasing the Na^+ concentration. Although, the assumption of low potentials made in the Debye-Hückel approximation is not always true, the effects of ion concentration and valency of the electrolyte solution are qualitatively consistent with results from more elaborated calculations [47].

As previously mentioned, the surface potential is often not directly accessible, however, another parameter related to the surface potential is measurable: the zeta potential which is also referred to as the electrokinetic potential of the slipping plane since it is defined as the potential between the slipping plane and the bulk solution. When the charged surface in solution experiences a shear stress, the ions within the slipping plane will remain around the surface. In contrast, ions outside the slipping plane will be sheared off the surface. A common technique to induce shear stress on the particle, is to apply an electrical field which results in the movement of the particle towards the electrode of opposite charge. The particle mobility μ can then be related to the ration of the particle drift velocity v and the electrical field strength E. The drift velocity depends on the potential at the slipping plane – the zeta potential ζ – and on the viscosity of the medium η, whereas the strength of the electrical field is influenced by the dielectric constant of the medium ε_r. From this consideration one yields the following equation for the particle mobility:

$$\mu = \frac{v}{E} = \frac{\varepsilon_r \varepsilon_0 \zeta}{\eta} \tag{3}$$

To determine the zeta potential of a particle, the drift velocity of the particle needs to be measured provided that the electric field strength, the viscosity and the dielectric constant of the medium are known. During this thesis zeta potential measurements were performed using a ZetaSizer ZS (Malvern Instruments, Herrenberg, Germany). The ZetaSizer applies an electrical field to the particle suspension, then uses laser Doppler electrophoresis and phase analysis light scattering[3] to obtain the drift velocity of the particles and calculates the zeta potential as outlined before. This technique is sensitive to high conductivity, accordingly the salt concentration of the medium used to perform the measurement should not exceed 10 mM.

For zeta potential measurements, about 1 µL of particles were suspended in 999 µL buffer (see Table 3 for more details). The success of the particle PEGylation was verified by determining the zeta potential of ζ = -38 mV for the carboxylated particles before PEGylation and ζ = -20 mV after PEGylation.

Table 3: Zeta potential of particles used in Section 4.1 and Section 4.2

Particles	**Buffer**	**Zeta potential/mV**	**Study**
200 nm COOH	20 mM Tris 10 mM NaCl pH 7	-35	Biophysical properties of basal lamina Section 4.1
200 nm NH_2	20 mM Tris 10 mM NaCl pH 7	+8	Biophysical properties of basal lamina Section 4.1
200 nm PEG	20 mM Tris 10 mM NaCl pH 7	-12	Biophysical properties of basal lamina Section 4.1
300 nm COOH	20 mM HEPES 20 mM NaCl pH 7	-87	Ion-specific effects Section 4.2
300 nm NH_2	20 mM HEPES 20 mM NaCl pH 7	+51	Ion-specific effects Section 4.2

Although it is tempting to deduce quantitative information about the surface potential from the zeta potential measurements, this is not possible since the position of the slipping plane is unknown and varies depending on parameters such as buffer type, pH and sort of ions. However, for matching buffer conditions the zeta potential gives a hint how strong a particle species is charged compared to another particle species and thus allows for making a quantitative statement.

[3] Detailed information about both techniques can be found on the Malvern website: http://www.malvern.com/de/pdf/secure/TN101104PhaseAnalysisLightScattering.pdf

3.2 Particle diffusion experiments

3.2.1 Mean squared displacement

Diffusion or Brownian motion of particles in an aqueous medium was detected already in 1827 by Robert Brown. The explanation for the random movement of particles was given by Albert Einstein in 1905 [48]: the particle motion is due to collisions with the surrounding water molecules. Since collisions are equally probable from all directions, the mean displacement of the particle is zero, however, the mean squared displacement grows with time. Thus, Einstein related the diffusion coefficient to the mean squared displacement of the particle as follows:

$$<x^2> = 2nDt \tag{4}$$

Here, n is the dimension in which the diffusion process is observed, D is the diffusion coefficient and t is the time of observation. In two dimensions, the mean squared displacement can be regarded as the mean area a particle can explore within a given time. In addition to normal diffusion, two other types of diffusion have been described: super diffusion and subdiffusion. In general, a diffusive process is described by a power law in time where the value of the exponent α is used to discriminate between the three types of diffusion:

$$<x^2> \sim t^{\alpha} \tag{5}$$

When a particle is super diffusive which occurs mostly if it is actively transported, the mean area it explores does not scale linearly in time anymore but with an exponent greater than one ($\alpha > 1$). One example for active transport is found in cells where cargo is transported by kinesin "walking" on microtubuli. In contrast, a subdiffusive particle explores a smaller area in a given time than a normal diffusive particle which leads to an exponent of t smaller than one ($\alpha < 1$). An example for subdiffusion is the diffusion of lipids in a lipid bilayer in which obstacles are present and thus spatially restrict the area of lipid movement. Only for $\alpha = 1$ the relation given by Einstein (Equation (4)) is valid, in all other cases an apparent diffusion coefficient may be calculated according to this equation; however, the value obtained for D_{app} does not reflect a truly diffusion behavior.

In this thesis, particle tracking experiments were conducted (Section 4.1 and Section 4.2) using a conventional wide-field microscope and a digital camera (see Section 3.2.2 and Section 3.2.3 for more details). This setup allows for recording the particle movement in an x-y-plane (2D) although the particle can actually move in all three spatial dimensions. If the particle movement is isotropic, which is a reasonable assumption in a homogenous gel, the 3-dimensional diffusion process can be projected into a 2-dimensional plane without loss of information about the diffusion process. Such a situation occurs when a particle is observed under a conventional microscope because only movements in the x-y-plane are observed. This leads to the impression that the particle moves slower than it would if also the movement in z-direction could be observed. However, this is corrected for by the dimensionality n which is included in the equation given by Einstein. Thus, the same diffusion coefficient is obtained for a 3-dimensional diffusion process observed only in the x-y-plane as if the particle could be followed in 3-dimensions.

To calculate a diffusion coefficient for a particle from the recorded videos, the trajectory of the particle is needed. Such trajectories were obtained using the image analysis software OpenBox

developed at TU München [35]. The particle position was followed by a tracking algorithm using a two-dimensional Gaussian fit to the particle intensity profile. For a point-source, the intensity distribution is well-approximated by a Gaussian, and an accuracy of 2 nm has been demonstrated for a particle tracking procedure using 2-dimensional Gaussian fits [36]. Whereas this Gaussian approximation does not hold true anymore for particles much larger than the wavelength of light, the intensity profiles of the 300 nm and 1 µm particles used here can still be well-approximated by a Gaussian fit, and the applied tracking procedure resulted in subpixel resolution [35].

The output from OpenBox is a text file with the x- and the y-coordinate of the particle given in pixel values for every frame. Usually, a frame rate of 15.6 frames per seconds was used resulting in a temporal resolution of 64.1 ms. The length of a movie was 20 s which leads to a total of 312 images per movie. The mean squared displacement (MSD) can then be determined from the trajectory $\vec{r}(t)$ of a particle, as follows:

$$MSD(\tau) = \frac{1}{N}\sum_{i=1}^{N}\left[\vec{r}\left(i\Delta t + \tau\right) - \vec{r}(i\Delta t)\right]^2 \tag{6}$$

Here, the trajectory $\vec{r}(t) = \left(x(t), y(t)\right)$ has an x- and a y-component, which correspond to the x- and y-coordinates given by OpenBox. For both, τ and t, only such values can occur, which are multiples of the temporal resolution of 64.1 ms. An exemplary set of values for x- and y-coordinates can be found in Table 4.

Table 4: Exemplary values obtained from a particles tracking experiment.

Frame	**Time [ms]**	**x-position [pixel]**	**y-position [pixel]**
1	0	1252.183	398.3111
2	64.1	1253.138	398.281
3	128.2	1253.549	398.093
4	192.3	1251.611	400.0533
5	256.4	1250.843	401.2951

In the next step, the mean squared displacement for the first value of τ which corresponds to one frame or 64.1 ms is calculated. The easiest way of calculating this is by generating a table according to the example given in Table 5. Here, the x- and y-coordinates for every frame are written into the second and fifth row. Those rows are copied, shifted by one entry and inserted in the first and the fourth row. Now all entries in the second row are subtracted from the entries in the first row. The same is done for the y-coordinates of the particle in row four and five. This results in four values for particle position differences $\Delta x(\tau = 64.1\ ms)$ and $\Delta y(\tau = 64.1\ ms)$. Those values are squared and then the mean is calculated. This procedure is repeated with increasing time shift τ ranging from 64.1 ms to 19.9351 s.[4] The example given in Table 5 already illustrates the problem that sets in for larger time shifts τ: the number of entries which are averaged decreases by one entry per time shift.

[4] The maximum of τ is determined by the time difference between the first and the last image of the movie.

Table 5: The first and fourth row are shifted by τ = 64.1 ms and then the second and fifth row are subtracted, respectively.

x-position [pixel] shifted by one image	**x-position [pixel]**	**Δx(τ = 64.1 ms)**	**y-position [pixel] shifted by one image**	**y-position [pixel]**	**Δy(τ = 64.1 ms)**
1253.138	1252.183	0.955	398.281	398.3111	-0.0301
1253.549	1253.138	0.411	398.093	398.281	-0.188
1251.611	1253.549	-1.938	400.0533	398.093	1.9603
1250.843	1251.611	0.768	401.2951	400.0533	1.2418
	1250.843			401.2951	

When 312 images are available, τ = 64.1 ms results in 311 entries which are averaged. For the next value of τ = 128.2 ms 310 entries are averaged until for the last τ = 19935.1 ms only one entry is left which makes averaging impossible. To avoid artifacts arising from these statistical limitations, only the first 10 % of the $MSD(\tau)$ data are used to determine the apparent diffusion coefficient and the degree of subdiffusivity α. The mean squared displacement is then fitted by [49]:

$$MSD(\tau)=4Dt+v^2t^2 \tag{7}$$

The first part of Equation (7), the diffusive part, is already known from Equation (4). In the second part, the flow part, v represents the drift or flow velocity. This function accounts for potential drift in the MSD data, which can occur in the experimental setting, e.g. because of convection. The diffusive part will dominate at earlier times ($\tau << 4D/v^2$) whereas the flow will dominate at later times ($\tau >> 4D/v^2$). To ensure a reliable value for the diffusion coefficient the following criterion should be fulfilled:

$$\tau = 2 \text{ s} < 4D/v^2 \tag{8}$$

The value of $\tau = 2$ s comes from the fact that only the first 10 % of the *MSD* data are used for the fitting procedure. As long as Equation (8) is valid, the flow is not dominant and a reasonable diffusion coefficient is obtained.

As mentioned earlier, there are three types of diffusion, and only in the case of normal diffusion Equation (4) yields the diffusion coefficient. Thus, the exponent α is determined by fitting a power law function $MSD(\tau) = A + B\tau^{\alpha}$ to the short-time regime of $MSD(\tau)$. In this thesis, *MSD* curves were classified as normal diffusive as long as $0.7 < \alpha < 1.2$.

To validate this methodology, it was applied to 1 µm particles freely floating in water. The obtained diffusion coefficient $D_{H_2O} = 0.43$ µm^{2}s^{-1} can be related to the viscosity of water η_{H_2O} using the Einstein relation $D = \frac{k_B T}{6\pi\eta R}$ where $6\pi\eta R$ denotes the Stokes friction coefficient for a spherical particle of radius R. The obtained value of $\eta_{H_2O} = 1.04\ mPas$ matches the viscosity of

water at room temperature very well. Also, we obtain an exponent $\alpha = 0.88$ for an ensemble of 1 µm particles that are freely floating in water, which is reasonably close to the theoretically expected value of 1.

3.2.2 Particle tracking experiments: ECM comparison

For the particle diffusion experiments in Section 4.1, the ECM gels were thawed on ice and afterwards diluted with IMDM to a final protein concentration of 3.5 mg/mL. To induce gelation, all samples were incubated at their final protein concentrations in presence of the respective test particles at 37 °C for 30 min. Particle trajectories were obtained and analyzed as mentioned before. The movies of particles were acquired with a digital camera (Orca Flash 4.0 C11440, Hamamatsu, Japan) using the software Hokawo provided by Hamamatsu on an Axiovert 200 (Zeiss, Oberkochen, Germany) microscope with a 32 x objective (Zeiss, Oberkochen, Germany). All particles with an apparent diffusion coefficient larger than $D_{cut} = 1\ \mu m/s^2$ which is half the diffusion coefficient of a 200 nm-sized particle in water, were classified as "diffusing". In every sample, particles from at least three different fields of view were analyzed, and every experiment was repeated three times. That way, a total of at least 1000 particles were analyzed for each particle species.

3.2.3 Particle tracking experiments: Ion-specific effects

Fluorescence microscopy for image acquisition was conducted on an Axioskop 2 MAT mot microscope (Zeiss, Oberkochen, Germany) equipped with an EC Epiplan-NEOFLUAR 50x HD-DIC objective (Zeiss). Images were acquired with a digital camera (Orca-R2 C10600, Hamamatsu, Japan) using the software HCImageLive provided by Hamamatsu. To classify particles as mobile and immobile, videos of 10 s duration were analyzed in a fast-forward mode. In this mode, one can clearly distinguish between mobile and trapped particles. After a first rough classification into a mobile or a trapped state, it was checked if the particles change their state of mobility during the duration of the video. If that was the case, the particles were assigned to the state they were in at the beginning of the video.

3.3 Computer simulations

Matlab (MathWorks, Ismaning, Germany) was used for the numerical simulations of freely diffusing particles to evaluate the level of statistical uncertainties of the experimental data. Each coordinate of a simulated particle trajectory was generated by drawing a random number from a Gaussian probability distribution which is centered around zero. This was done independently for x- and y-coordinates. Both data sets, the one numerically generated and the one experimentally acquired, were evaluated with the same routine in order to ensure maximal comparability.

3.4 Rheology

The quantification of the viscoelastic properties as well as the gelation kinetics of the different ECM gels in Section 4.1 was performed on a stress-controlled macrorheometer (MCR 302, Anton Paar, Graz, Austria) with a 25 mm plate-plate geometry at a plate separation of 200 µm using a torque of 0.5 µNm and a frequency of 1 Hz ensuring linear response. The rheometer plate was cooled to 5 °C before 150 µL of the samples were added, and gelation was induced by a sudden temperature change to 37 °C. A thin layer of polydimethylsiloxane oil (ABCR, Karlsruhe,

Germany) was applied to the outer rim of the sample to avoid drying artefacts. An applied oscillatory stress $\sigma = \sigma_0 \sin(\omega t)$ with a frequency ω resulted in an oscillatory strain with the same frequency, $\gamma = \gamma_0 \sin(\omega t + \delta)$, where δ denotes the phase shift between stress σ and strain γ. With those parameters, the storage modulus $G' = \sigma_0/\gamma_0 \cos(\delta)$ can be calculated which is a measure for the elastic properties of the gel, and the loss modulus $G'' = \sigma_0/\gamma_0 \sin(\delta)$ which is a measure for the viscous properties of the gel.

To ensure that the high salt concentrations in the study on ion-specific effects (Section 4.2) did not impair the mechanical integrity of the ECM, rheological measurements were performed on a stress-controlled macrorheometer (MCR 102, Anton Paar, Graz, Austria). The settings were chosen as described above with only small differences: only 100 µL of ECM was used which resulted on a plate separation of 175 µm.

3.5 Microfluidic channel

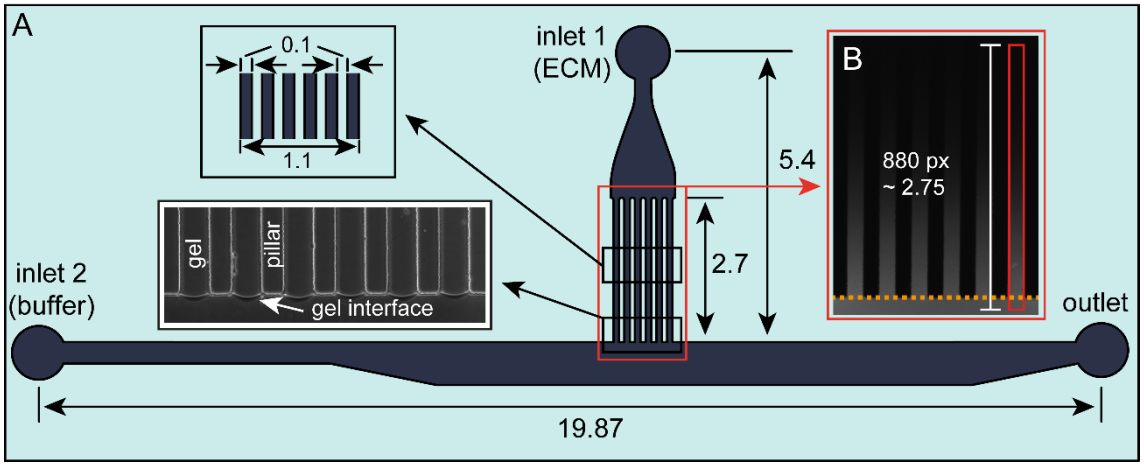

Figure 5. (A) The microfluidic chip as used in the study described in Section 4.3 has two inlets: inlet 1 for inserting the ECM and inlet 2 for inserting buffer together with fluorescent molecules of interest. The pillar structure prevents the injected ECM from entering the lower channel due to surface tension. (B) For data analysis, the fluorescence intensity within each channel is measured within a rectangular area (red rectangle) with a length of 880 pixels corresponding to 2.75 mm. The lower end of the rectangular is placed 50 pixels into the lower channel so that the bulk intensity in the buffer channel is obtained as well. The orange dotted line denotes the position of the gel/buffer interface. All dimensions in the shown scheme are given in mm.

Soft lithography was used to fabricate the microfluidic chips (Section 4.3). The channel geometry was designed using AutoCAD (Autodesk, Munich, Germany) and the mask was printed at a resolution of 64000 dpi (Zitzmann, Eching, Germany). The master was fabricated on a silicon wafer (Siegert Wafer, Aachen, Germany) with EpoCore (micro resist technology, Berlin, Germany) as a negative photoresist. First the silicon wafer was checked for cleanness and, if dust was visible, pressurized air was used to remove it. Next, 3-5 mL of the photoresist was dispensed carefully, to avoid air bubbles, into the center of the clean silicon wafer. The wafer was placed onto the spin coater (Laurell, North Wales, USA) such that the dispensed photoresist droplet was centered on the axis of rotation. The wafer was spun for 15 s at low rotation speed (300 rpm) but

high acceleration to spread the photoresist. After this initial spin, the wafer was spun at the final rotation speed of 1000 rpm for 35 s to obtain the desired thickness of about 125 µm. The wafer was immediately placed on a 65 °C hotplate for 5 min and covered with a glass petri dish to avoid contaminations. Subsequently, the wafer was placed onto a 95 °C hotplate for 10 min and again covered with a petri dish. The wafer was cooled down (still covered with a petri dish) for 10 min to prevent the photomask from sticking to the photoresist. The crosslinking of the EpoCore was achieved via UV irradiation for 7 min with the photomask placed on top of the wafer. The photoresist is crosslinked in all transparent areas of the photomask, all other spots will remain uncrosslinked. Next, the wafer was placed on a hotplate at 65 °C for 5 min and afterwards at 95 °C for 20 min. After this post exposure baking, the wafer was cooled down and all remaining uncrosslinked photoresist was develop with mr-Dev 600 (micro resist technology, Berlin, Germany). Finally, the master was rinsed with isopropanol to remove remaining developer.

For the microfluidic channel fabrication Sylgard 184 (Dow Corning, Midland, MI, USA) elastomer was mixed at a 10:1 ratio with curing agent, i.e. 20 g elastomer was mixed with 2 g of curing agent. Mixing of both components results in a high amount of air bubbles which were removed by applying a vacuum for 30 min. The now clear but very viscous solution was carefully poured onto the master without creating any air bubbles. This is achieved best when the PDMS is poured into the center of the master since potential air bubbles are then transported to the edge of the petri dish distant from the region of interest. The PDMS will cure at room temperature for 48 h, however, the curing process can be accelerated by increasing the temperature. Here, 80 °C was chosen as a curing temperature for 1 h. The cured PDMS was carefully cut around the channel geometry with a scalpel. During the cutting, the channel structure of the master should not be touched by the scalpel, to avoid damage. The cut PDMS was peeled off and inlets were punched into the PDMS using a biopsy puncher with a diameter of 1 mm. The side of the PDMS on which the channel geometry is printed on, was protected from dust by applying a stripe of adhesive tape to it. When several PDMS stamps were manufactured, they were bonded to a glass slide using oxygen plasma at 20 W for 30 s. When PDMS is exposed to oxygen plasma polar silanol groups, mainly SiOH are introduced to the PDMS surface. This introduction of polar surface groups results in a change from hydrophobic to hydrophilic surface properties of the PDMS [50]. The silanol groups on the PDMS surface react with the same type of groups on the glass surface resulting in a Si-O-Si covalent bond between glass and PDMS [51]. The PDMS regains the hydrophobic properties by diffusion of low molecular weight silicon chains from the bulk to the surface. This process is facilitated by higher temperatures [52], thus the bonded device was stored in an oven at 120 °C overnight to restore the hydrophobic properties of the PDMS.

For the experiments, the ECM was thawed on ice for several hours. The liquid (i.e. still ice-cold) ECM was filled into the chip through inlet 1. Here, at half the channel length, a "finger-like" structure begins where five pillars divide the main channel into six smaller channels of identical width. When liquid ECM is filled into inlet 1, it can be carefully pushed into this finger-like structure until, at the end of the pillars, surface tension effects ensure stopping of the liquid (see inset of Figure 5) and prevent it from entering into the buffer channel which is oriented perpendicular to the pillars. With this setup, a well-defined liquid/air interface is created which is important for the following experiments. As the ECM was inserted into the chip in its liquid state, gelation has to be induced on chip. Such a gelation of ECM is usually achieved by a heating step to 37 °C for 30 minutes. Here, the gelation was induced at room temperature since all following experiments were conducted at this temperature. During gel formation, it is important to prevent

drying of the ECM - especially at the interface to the compartment which will be filled with fluorescent solutes. A naive approach to avoid such drying of the ECM interface might be to induce gel formation at a water interface. This could be achieved by inserting an aqueous solution, e.g. buffer, through inlet 2 directly after loading the chip with the liquid ECM. However, as gelation requires some time, the mechanical strength of the ECM is still weak when the buffer is inserted, and thus the integrity of the ECM compartment is disturbed by buffer influx. Furthermore, when placed at an aqueous interface during gelation, the ECM tends to swell and locally dissolves which in turn results in a diffuse gel interface. A better solution would be to perform gelation at an interface with a hydrophobic fluid that is immiscible with the ECM (and thus does not dissolve the ECM matrix) but still prevents drying. Thus a polydimethylsiloxane oil (PDMS) was chosen which fulfills those requirements and is based on the same polymer used for crafting the microfluidic chip. The PDMS oil was inserted through inlet 2 into the lower channel and it was kept in this compartment until ECM gelation was finished. The oil was then removed from the chip through the outlet and replaced by PBS buffer. Buffer containing test molecules was carefully inserted into inlet 2 with a Hamilton syringe (1702 sleeve type), which ejects a volume of 0.33 µL per rotation. The buffer was inserted very slowly and carefully especially when it approached the finger-like structure. Here, it was very important move the front of the PBS only a few micrometers per second to ensure minimal forces acting on the ECM interface in the finger-like structure.

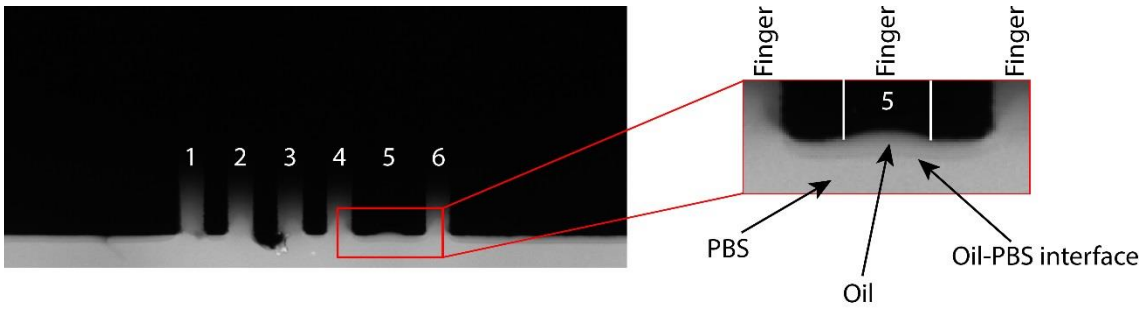

Figure 6. Left: The six fingers of the microfluidic channel are shown shortly after the PBS with test molecules was inserted. **Right:** Zoom into the 5th finger at whose interface the oil was not removed. The finger remained dark as no buffer with fluorophores could enter this finger.

When the channel was completely filled with buffer the flow was stopped. When the PBS was inserted into the channel, a clear interface between PBS and PDMS oil was visible under the microscope. This feature allowed to monitor the proper removal of the oil from the channel. In some rare cases, the PDMS oil was not fully removed from the border of the gel at the end of the finger-like structure. However, such an event can easily be detected under the microscope (see Figure 6). If a thin layer of oil remains at the gel interface, the test molecules are not able to enter the gel phase at all, and those channels were excluded from the analysis. With this approach, intact gel/buffer interfaces were generated with which reproducible penetration profiles with different test molecules were obtained.

In the first experiments conducted with this microfluidic chip, it was observed that the fluorescence in the outermost channels of the finger-like structure appeared to be lower than in

their neighboring channels. It was suspected that those outermost channels are subjected to drying effects since they are mostly surrounded by PDMS. In general, PDMS is hydrophobic but it is permeable to water vapor. Thus, water from the outermost channels could vaporize and leave through the PDMS. To prevent this drying effect, a water reservoir was placed on top of the PDMS at the position of the finger-like structure (Figure 7). The water reservoir should not come into contact with inlet 1 since this resulted in unwanted influx of PBS buffer into the finger-like structure upon insertion.

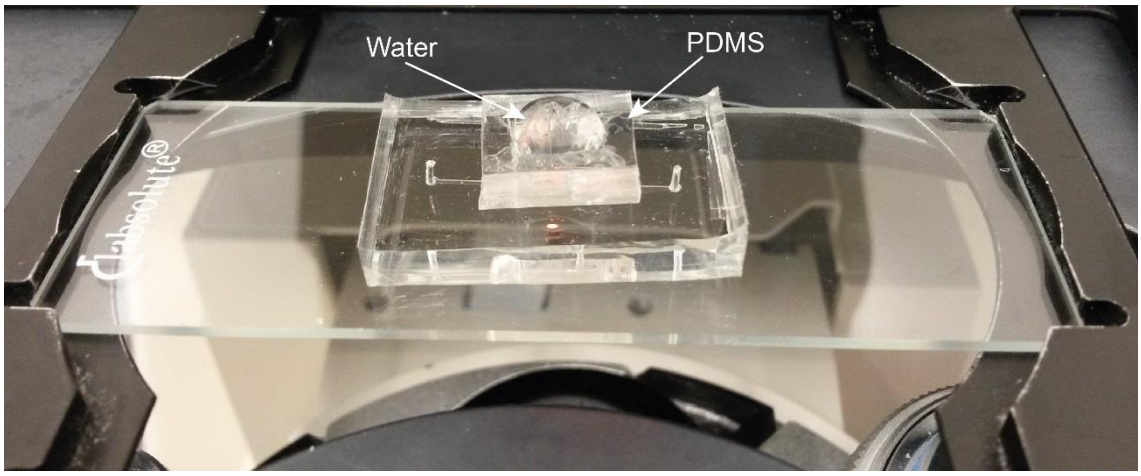

Figure 7. A water reservoir was placed on top of the microfluidic chip to prevent drying.

3.6 Data acquisition and evaluation

Images were acquired with a digital camera (Orca Flash 4.0 C11440, Hamamatsu, Japan) using the software Hokawo provided by Hamamatsu on an AxioVert 200 (Zeiss, Oberkochen, Germany) microscope using a 4x objective (Zeiss, Oberkochen, Germany). To account for the inhomogeneous illumination of the microfluidic chip, two steps were performed prior to the start of the experiment: First, an image was taken without any illumination. This image served as background image $IMG_{\text{background}}$ and contains the pixel bias offset level and the noise acquired from electronic and thermal sources. Second, an image was obtained with a fluorescent sample in the field of view and the illumination turned on. For this, a glass slide was prepared with 40 µL of PBS buffer containing fluorescent test molecules and a cover slip on top of it. Since the illumination was inhomogeneous, the acquired image of the fluorescent sample showed heterogeneous grey values. This image IMG_{Shading} was stored as a reference for the shading correction. Both, the background image and the shading correction were used to compensate for the inhomogeneous illumination. This was realized by a built-in function of the software Hokawo. This function calculates the grey value of the live image according to the following equation:

$$IMG = \frac{RAW - IMG_{background}}{IMG_{Shading} - IMG_{background}} \times RAW_{Mean} \tag{9}$$

To obtain the live image (*IMG*), the background image is subtracted from both the raw image (*RAW*) and shading correction image, followed by the division of the resulting values. This is then multiplied by the mean pixel value of the raw image in order to corrected image intensities.[5]

For a proper evaluation of the intensity values, two things have to be considered: First, the grey values of the pixels should not be at their saturation value. Second, the camera detector should also not operate at its minimum photon count since then noise is not negligible anymore. The potential gray values of the single pixels range from 0 to 65535 for a 16 bit image where 65535 is the saturation value. The amount of photons and thus the grey value of the pixel can be tuned either by binning of pixels or by an increase of the exposure time. The first method, binning, decreases the spatial resolution whereas the second method decreases the temporal resolution. In the study conducted in Section 4.3 the images were acquired every 5 min, accordingly the temporal resolution was not important. Thus, the exposure time was chosen such that no pixel saturation occurred. Each of the six channels was analyzed individually with ImageJ. A rectangular with a height of 880 pixels corresponding to 2.75 mm and a width of 30 pixels (0.09 mm) was placed in the channel such that 50 pixels (0.16 mm) of this rectangular were located in the lower channel (Figure 5 B). This procedure allows to account for the bleaching of the fluorescent label of the test molecules. Since no continuous flow was applied, the fluorophores in the buffer compartment are subjected to same rate of bleaching as the molecules within the ECM. Therefore, the fluorescence intensity in the buffer channel (calculated from the 50 pixels of the rectangular in the lower channel) was used as a reference to normalize the intensity in the finger-like structure. This ensures the comparability of the calculated intensity profiles at different time points during the experiments.

The intensity within the chosen rectangular was averaged per pixel line with a function implemented in ImageJ. Thus, one intensity value per line was obtained. In a next step, these average intensity values per line were averaged again, first over the six finger channels of a chip and then over three different microfluidic chips.

[5] Information from the Hokawo software help center, „Shading correction“

4 Summaries of publications

4.1 The Biophysical Properties of Basal Lamina Gels Depend on the Biochemical Composition of the Gel

The extracellular matrix (ECM) purified from the Engelbreth-Holm-Sarcoma of mice serves as a model system for the basal lamina. It is widely used in cell culture and as a 3D matrix in cell migration experiments. The ECM can be obtained from different suppliers which all use the same purification protocol established by Kleinman [31,32]. However, results obtained with these gels often contradict each other and the reason for this remains unknown. In this publication, the biophysical properties of ECM gels from four different suppliers are investigated and differences between the gels are related to their biochemical composition.

When cell migration experiments are conducted with HL-60 cells in these ECMs, drastic differences between the gels are obtained. In ECM3 and ECM4 fast migration is observed, in ECM2 the migration is retarded and in ECM1 the cells show no migration activity but a high number of dead cells compared to the other gel variants is observed. The retarded migration activity of the HL-60 cells in ECM2 is related to a difference in microstructure of the network obtained by diffusion studies with tracer particles. PEGylated 200 nm-sized polystyrene particles are mobile in ECM1, ECM3 and ECM4 but not in ECM2. As no electrostatic or hydrophobic interactions are expected for PEGylated particles, the lack of diffusion results from a smaller mesh size in ECM2 compared to the other ECM variants.

The microstructure of the ECM network is further investigated by imaging techniques such as confocal fluorescence microscopy, where key components of the ECMs are stained by antibodies, and scanning electron microscopy. Both approaches show similar results concerning differences in the microstructure of the gel variants: ECM1, ECM3 and ECM4 are very similar, whereas for ECM2 a much denser network is obtained. The same trend is observed in macrorheological measurements where ECM2 shows a several fold higher storage modulus than the other three gel variants which are again very similar to each other. Both, the higher storage modulus and the denser network, is due to a higher amount of the crosslinking molecule entactin in ECM2 which is revealed by densiometric analysis.

The higher amount of dead cells in ECM1 compared to the other gels is further investigated by an analysis of the macromolecular components of the ECMs using SDS-PAGE with coomassie staining. ECM1 shows an additional band which is further analyzed by mass spectroscopy. The laminin subunits alpha1 and beta1 are detected but at a smaller molecular size than normal. This suggests that a proteolytic breakdown has occurred during the purification process. Further, it is speculated that these laminin fragments are cytotoxic and therefore responsible for the higher amount of dead cells in ECM1.

This study underlines the impact single proteins and their fragments can have on the biophysical properties of biological hydrogels.

Individual contributions of the candidate: I contributed to the conception and design of the original study. I performed the particle diffusion studies as well as the rheological measurements and analyzed the data from both experiments. I wrote the article.

4.2 Ion-Specific Effects Modulate the Diffusive Mobility of Colloids in an Extracellular Matrix Gel

Understanding the physical principles which regulate the diffusive transport of nanoparticles through biological barriers such as the basal lamina is important for the design of drug delivery vehicles. Previous experiments have shown that charged polystyrene particles are trapped by an extracellular matrix (ECM) gel which serves as a model system for the basal lamina. The trapping of particles was attributed to electrostatic interactions between the particles and the ECM constituents.

In this publication, these interactions are further investigated by diffusion studies with negatively and positively charged polystyrene particles at increasing concentrations of mono- and divalent ions. The addition of these ions results in an effective charge screening, and - as a result - a fraction of formerly trapped polystyrene particles is mobilized. The fraction of mobile particles increases with increasing ion concentrations. Divalent ions are more efficient in mobilizing particles compared to monovalent ions which results in a higher fraction of mobile particles for divalent ions than for monovalent ions at matching concentrations. Moreover, this mobilization effect is ion-specific: at intermediate salt concentrations of the divalent cations Mg^{2+} and Ca^{2+} the mobile fraction of negatively charged particles is higher for Ca^{2+} than for Mg^{2+}, although both ions have the same valency and should screen electrostatic interactions with similar efficiency. This efficiency of Mg^{2+} and Ca^{2+} to mobilize particles is inverted when positively charged particles are used for the experiments. The observed Hofmeister-like ion-specific effects underline the previous notion that in addition to electrostatic interactions also hydrophobic interactions play a key role in the immobilization of polystyrene particles in this ECM gel.

Single particle tracking is employed to evaluate the trajectories of individual particles at high concentrations of KCl. A rigorous analysis of these trajectories leads to a discrimination between three states of particle motion: freely diffusing particles, particles which are weakly bound to the ECM and strongly bound particles. The particles are able to dynamically switch between the mobile and immobile state as well as between the weakly and the strongly bound state. Moreover, selected particles even exhibit all three states of motion within an observation time of several minutes. The mean squared displacement curve of such a particle which transiently binds to the network during the tracking indicates subdiffusive behavior although the particle exhibits normal diffusion between the binding events. This underlines the importance of a detailed analysis of particle trajectories in single particle tracking experiments to identify the physical mechanism leading to subdiffusive behavior.

The results obtained here about electrostatic and hydrophobic interactions contributing to the trapping of nanoparticles in basal lamina gels, might help in the design of new drug carrier vehicles. Furthermore, the salt dependent mobilization of nanoparticles might also find an application in the tattoo removal industry.

Individual contributions of the candidate: In this publication, I designed, performed and analyzed the experiments with the different ions and obtained the transient binding events. I wrote the article.

4.3 A microfluidics approach to study the accumulation of molecules at basal lamina interfaces

The passage of molecules such as nutrients, growth factors and drugs from the blood stream into the connective tissue is regulated by a complex barrier, the blood vessel wall. This barrier consists of a cell layer of endothelial cells and a layer of basal lamina. In the case of a leaky endothelium which occurs e.g. during inflammation or when a tumor is present, blood compounds can easily pass the endothelium, and the only barrier to overcome before they reach the connective tissue is the basal lamina.

In this study, a microfluidic setup is designed to investigate the diffusion of molecules across a basal lamina interface. As model system for the basal lamina, an extracellular matrix purified from the Engelbreth-Holm-Swarm sarcoma is used. This biological material is liquid at temperatures below 15 °C and becomes a soft gel at temperatures above 15 °C. The design of the microfluidic chip is chosen such that the ECM can be filled into the chip in its liquid state and stops at the end of pillars because of surface tension effects. To prevent the ECM from drying during the gelation process, which has to take place on chip, polydimethylsiloxane oil is inserted into the channel perpendicular to the ECM and a water reservoir is placed on top of the channel. Oil is used since it does not mix with the hydrophilic ECM. After gelation is finished the mechanical stability of the ECM is high enough so that the oil can be replaced by an aqueous buffer containing test molecules without damaging the gel. With this method, it is possible to produce stable buffer/ECM interfaces in a reproducible manner.

The diffusive transport of test molecules across this stable buffer/ECM interface is analyzed by fluorescence microscopy. As test molecules, FITC-labeled dextrans with two different molecular weights are used. Both dextrans carry a certain percentage of either positively charged or negatively charged groups. Negatively charged dextrans of both molecular sizes enter from the buffer compartment into the gel compartment as one would expect from Fick's law of diffusion. The same in-bulk behavior is observed for the positively charged dextrans. However, at the buffer/ECM interface positively charged dextrans of both molecular sizes show an accumulation peak whereas no accumulation is observed for the negatively charged dextrans. Further experiments with custom-made peptides show that the height of the accumulation peak depends on the amount of positive charge. Transient binding events of positively charged molecules to the ECM along with the high concentration of molecules in the buffer compartment are responsible for this accumulation peak at the buffer/ECM interface. This interface behavior is reproduced by numerical calculations in which molecules can transiently bind to the gel with high and low affinity, respectively. The accumulation peak height is then set by the binding affinity of the molecules to the gel.

In vivo experiments in which the test molecules are microinjected into the cremaster muscle of mice show an accumulation of positively charged test molecules around blood vessels. Subsequent immunohistological staining shows that the accumulation co-localizes with collagen IV, a key component of the basal lamina. Thus, the *in vitro* setup designed here correctly predicts the diffusive transport of molecules in an *in vivo* setting and can therefore serve as a test setup for the spreading of molecules without the need for animal experiments.

Individual contributions of the candidate: In this publication, I designed the experiment, developed the microfluidic setup, performed and analyzed the *in vitro* experiments. I wrote the article.

5 Discussion and Outlook

In this thesis the following key results have been found and will be discussed in more detail:

- The proteolytic breakdown of laminin results in decreased cell viability.
- The mesh size and the mechanical stability of a basal lamina gels depend on the amount of the crosslinker entactin.
- Basal lamina gels and nanoparticles interact via electrostatic and hydrophobic interactions, and ion-specific effects.
- Transient binding events occur between polystyrene particles and the basal lamina
- At buffer/basal lamina gel interfaces, positively charged molecules show an accumulation peak whose height is determined by the amount of charge whereas negatively charged molecules show no such accumulation. In contrast, both types of molecules show similar diffusive transport in-bulk
- A simplified microfluidic chip is sufficient to predict key results for the diffusive distribution of molecules as obtained in *in vivo* experiments in living mice

It was shown in Section 4.1 that a proteolytic breakdown of laminin had occurred in ECM1 gel samples. In the same ECM no migratory activity of HL-60 cells was observed along with a higher amount of dead cells. It was suspected that laminin fragments, as they were found in this ECM by mass spectroscopy, are responsible for the retarded cell migration and also for the decreased cell viability and the cell death, respectively. In general, proteolysis of ECM components and thus the remodeling of this matrix is a process permanently present in the body. Remodeling of the ECM is e.g. a crucial part of wound healing and cell differentiation [53]. In addition, the degradation of ECM components can be responsible for cell apoptosis but, depending on the ECM component degraded, it can also enhance cell viability [54]. In particular, the degradation of laminin seems to be responsible rather for apoptosis than for the enhancement of cell viability. In a study conducted in mice it was determined that the breakdown of laminin by the matrix metalloproteinase 9 (MMP-9) induces neuronal apoptosis but can be prevented by the addition of MMP-9 inhibitors [55]. In principle, the degradation of laminin in the basal lamina could be used to increase the mesh size of the matrix. This would be advantageous for drug delivery application since larger particles could be used and therefore a higher amount of drugs could be delivered. However, the degradation of laminin does not only result in cell apoptosis but has also an impact on the mechanical stability of the basal lamina since removal of laminin results in a mechanical breakdown of the basal lamina [56]. In addition to the important role of laminin for the mechanical stability, it also interacts with the integrins on the cell surface and is the anchor between cells and basal lamina. A breakdown of laminin results in the detachment of the basal lamina from the underlying cell layer which results in a loss of cell-matrix communication [57,58]. Thus, enzymatic digestion of laminin might result in a higher particle mobility but is likely accompanied by unwanted side effects such as cell death. Such severe consequences as a result of protein degradation are, however, not observed for other basal lamina constituents. It was reported that the inactivation or mutation of the gene encoding entactin results in a normal basal lamina phenotype without any indication that the viability of the organism is impaired [59-61]. Exceptions are the lung and the kidney, both are organs which fulfill important filtering tasks; consequently, they contain a huge amount of basal lamina [62]. In Section 4.1, no correlation between the amount of entactin and the behavior of cells was found, except for a slow-down of cell migration velocity due to the smaller mesh size. This is in good agreement with the notion that the removal of entactin does not impair cell viability. In addition it was also shown that a

higher concentration of entactin results in a smaller mesh size of the ECM gel which hindered the diffusion of the PEGylated polystyrene particles due to steric hindrances.

The results presented here might help to circumvent steric hindrances in future applications. The exclusion of particles or molecules by the size of the particles is one of the simplest mechanism for retarding particle diffusion: a mesh size smaller or on the order of the particle diameter will efficiently trap particles. A straightforward way to circumvent steric hindrances would be to choose a particle size smaller than the mesh size. However, this might not be applicable in all situations especially when large amounts of drugs need to be incorporated. Another possibility to facilitate the diffusion of uncharged particles in the basal lamina could be to increase the mesh size. As mentioned above, entactin plays a major role in the determination of the mesh size of basal lamina gels. If entactin could be removed by the particles, the mesh size would increase locally. An approach for the removal of entactin could be the enzymatic digestion of the crosslinker molecules. To harness such a strategy for drug delivery, one could devise a combination of particles: one particle species with incorporated enzymes and a specific binding motif for collagen IV on the surface in combination with PEGylated particles (Figure 8). When the first particle species binds to collagen IV, which mostly occurs in basal lamina, the enzymes are released and digest the crosslinker entactin. Thus, the PEGylated particles could diffuse through the basal lamina without steric hindrances. The removal of entactin would result in a mechanical weakening of the gel. This effect, however, should not be as pronounced as if e.g. collagen IV or laminin would be digested.

As discussed previously, no negative influence on cells is expected when entactin is locally removed. Moreover, the production of entactin is not impaired by its local digestion. Thus, the removed crosslinkers can be replaced by newly produced entactin. Still, the influence of the enzyme on cell viability needs to be investigated and the following challenges need to be dealt with: First, an enzyme is needed which only cleaves entactin whereas laminin and collagen IV remain intact. Most enzymes used for the degradation of the basal lamina belong to the family of metalloproteinases, e.g. matrilysin. This enzyme degrades entactin but it acts also on collagen IV [63,64], which is unwanted for reasons previously mentioned. Another family of enzymes, known to degrade entactin, are the serine proteases [65]. However, those enzymes can also breakdown other ECM components, thus their specificity has to be tested. Second, if a proper enzyme is found, the influence of the enzyme on the cell viability needs to be investigated. To test this, cells can be embedded in a basal lamina gel and the cell viability is monitored by a WST-assay with and without the addition of entactin digesting enzymes. Third, if the cell viability is unchanged in the present of the enzyme, the incorporation of the enzyme into a particle and the release triggered by specifically binding to collagen IV needs to be tackled. Liposomes could be used as a carrier particle since incorporation of macromolecules into the phospholipid bilayer is easy, they are biodegradable and are already used in many drug delivery applications. A collagen IV antibody could be inserted into the lipid bilayer and the enzymes would be deposited inside the liposome. Still, a trigger is needed which opens the liposome upon binding to collagen IV.

In Section 4.2 it was shown that a combination of electrostatic and hydrophobic interactions is responsible for the trapping of charged polystyrene particles. At physiological salt concentrations, charged particles of both algebraic signs were efficiently trapped. Such a behavior has been reported before for polystyrene particles and for liposomes in basal lamina gels [33]. Similar results were obtained for other biological hydrogels such as mucus and the vitreous humor [66-68]. In all of these gel environments, PEGylation of the test particles resulted in nearly free

diffusion within the gels. In general, the covalent attachment of PEG chains to the carboxyl-groups of the particle surface has two effects: First, the particles become uncharged since the charged COOH groups are used for the covalent binding of the PEG chains. Second, PEGylation decreases the hydrophobicity of drug carriers [69,70]. Thus, PEGylation of particles alone does not suffice to entangle the contribution of electrostatic and hydrophobic interactions to particle trapping in hydrogels. To achieve such an entanglement of those interactions, high amounts of salts were added in Section 4.2 which results in an efficient charge screening. If only electrostatic interactions were responsible for particle trapping, all particles should be mobile at ion concentrations as high as 1 M NaCl. However, a significant fraction of particles remained trapped. This high fraction might be a result of Manning condensation, also referred to as counterion condensation. The concept of Manning condensation assumes that ions are recruited to a charged polymer to obtain an equilibrium between electrostatic energy and entropy [71]. The charged polymer is modelled as a line of charges with a certain charge density. If this charge density is very high, e.g. when DNA is considered, the polymer is restricted in the possible conformations it can assume. This results in an entropic penalty. The entropy can be increased when the charge of the polymer is screened, e.g. by counterions. This results in an entropy decrease for the ions since they are "bound" to the polymer but an increase in entropy for the polymer because more conformations are conceivable. It might be entropically even more favorable if the ions "bound" to the polymers are replaced by other charged objects, e.g. polystyrene particles, since the decrease in entropy for one particle is lower than the decrease of entropy for many ions. The polymers considered here are dissolved in an aqueous solution; thus, electrostatic forces between neighboring charges are decreased due to the high dielectric constant of water. A measure for the impact of electrostatic interactions compared to the thermal energy is given by the Bjerrum length [72] which is the ratio of the force acting between two elementary charges and the thermal energy. For water, the Bjerrum length has a value of 0.7 nm; accordingly, if two charges are closer to each other than 0.7 nm, electrostatic forces dominate. In contrast, if the distance between neighboring charges is greater than 0.7 nm thermal energy dominates. Thus, Manning condensation can only play a role, when the line charges are closer to each other than the Bjerrum length; this is also referred to as the Manning criterion. Thus, if the ratio Bjerrum length and the distance between two neighboring charges is greater than 1, Manning condensation is observed. To decide whether Manning condensation is applicable for the situation described in Section 4.2, the basal lamina constituents responsible for the binding of particles need to be known and evaluated. In a previous study, the molecule responsible for the trapping of the positively charged particles was identified to be heparan sulfate [33]. This glycosaminoglycan is strongly negatively charged and constitutes one of the main components of the basal lamina. For heparan sulfate, the ratio of Bjerrum length and line charge results in 2.1-2.8 depending on the degree of sulfonation which fulfills Manning's criterion. However, the fraction of mobile particles increased with increasing salt concentrations whereas the effect of counterion condensation is independent of the salt concentration [73]. Thus, Manning condensation effects are highly unlikely to significantly contribute to the strong particle trapping observed here.

In Section 4.2 it was shown, that the fraction of mobile particles increases with increasing ion concentration. This effect is even more pronounced when divalent ions instead of monovalent ions are used. It was argued that hydrophobic interactions are responsible for this observation since the observed effect is ion-specific (probably related to the Hofmeister effect). More than 100 years ago, Franz Hofmeister studied the effect of salts on the solubility of proteins [74]. In

his experiments with egg white, he observed that the precipitation of the egg white proteins depends on the cations and anions he chose for his experiments. Moreover, he observed a difference in the efficiency of precipitation between the anions and cations: In his experiments, the anions showed a larger effect on the protein precipitation than the cations. From his experimental results, he deduced the following order of anions and cations according to their efficiency of precipitating proteins (also referred to as the "Hofmeister series"):

Anions:

$$F^- \approx SO^{2-}_4 < HPO^{2-}_4 < CH_3COO^- < Cl^- < NO_3- < Br^- < ClC^-_4 < SCN^- < Cl_3CCOO^-$$

Cations:

$$NH^+_4 < K^+ < Na^+ < Li^+ < Mg^{2+} < Ca^{2+}$$

In this series the anions and cations are ordered from increasing hydrophobic effects (kosmotropes, left) to decreasing hydrophobic effects (chaotropes, right). When the hydrophobic interactions are increased, proteins form aggregates because the hydrophobic parts of the proteins tend to accumulate to minimize the contact area with the water molecules surrounding them. In contrast, the anions and cations further to the right in the Hofmeister series decrease the hydrophobic interactions. This results in a higher solubility of proteins since the folding of the proteins is driven by hydrophobic interactions, and when those interactions are decreased the proteins denature. The series presented above is not universally valid but depends on several parameters which are described below. In addition to the occurrence of ion-specific effects in protein systems, ion-specific effects are also observed in other systems, such as surfactant and polymer systems, at interfaces and in colloidal systems [75]. The detailed origin of ion-specific effects is still not fully understood because diverse interactions, such as ion-particle, ion-hydrogel as well as particle-hydrogel interactions, have to be considered [76]. These interactions are governed by a broad range of parameters, such as charge density, surface tension, structure and the chemical composition of macromolecules [76]. Molecular dynamics simulations along with spectroscopy techniques and light scattering are used to explore the influence of these parameters but up to now only simple systems were investigated with those approaches and still the detailed mechanism remains unknown [77-80].

Although the detailed mechanism underlying ion-specific effects still needs to be identified, ion-specific effects and their ability to solubilize proteins and to mobilize particles might be used for drug delivery applications. Two scenarios can be imagined: first, the mobilization of charged particles as it was seen in Section 4.2 and second, circumvention of steric hindrances imposed by the mesh size of the basal lamina by a local gel-solution transition of the basal lamina constituents. For the first scenario two particle species are needed: charged particles with incorporated drugs and a second particle species with embedded ions. Upon release of the ions the charge of the first particle species is screened and the drug carrying particles can further diffuse into the network. Two particle species are used because of the limited loading capacity and to exclude interactions between the salt ions and the drugs within the drug carrier. The second scenario would act on the side of the basal lamina and would need higher salt concentrations than the first scenario. As mentioned in Section 2.1 the gelation of the basal lamina gels is induced by an increase in temperature. A temperature triggered solution-gel transition is usually found for gel assembly as the result of hydrophobic interactions. Water molecules which are located at hydrophobic spots on the polymers of the matrix are forced into an ordered structure which results in a decrease in entropy. When the temperature is increased, the entropic penalty is increased which eventually results in an assembly of hydrophobic spots of polymers next to each other. As explained above,

chaotropic ions decrease hydrophobic interactions and can therefore reverse the solution-gel transition. This can be used for the delivery of large drug carriers through the basal lamina. When a high concentration of chaotropic ions is released, this could result in a local increase in mesh size since hydrophobic interactions responsible to maintain this mesh size are weakened. The ions have to be chosen carefully to keep the influence on the underlying cells to a minimum. Upon ion release a high local salt concentration is achieved which is depleted quickly since ion diffusion is very fast. When the salt concentration is back to its physiological concentration, the basal lamina should regain its former structure. In both scenarios, liposomes could be used to release the ions upon binding e.g. to collagen IV. When a high concentration of ions is incorporated into liposomes the osmotic pressure needs to be matched, otherwise the lipid bilayer can rupture and release the ions. If the osmotic pressure between liposomes, blood, and interstitial fluid is too high another ion carrier such as mesoporous polystyrene particles enclosed into an envelope which opens upon contact with e.g. collagen IV, might be used.

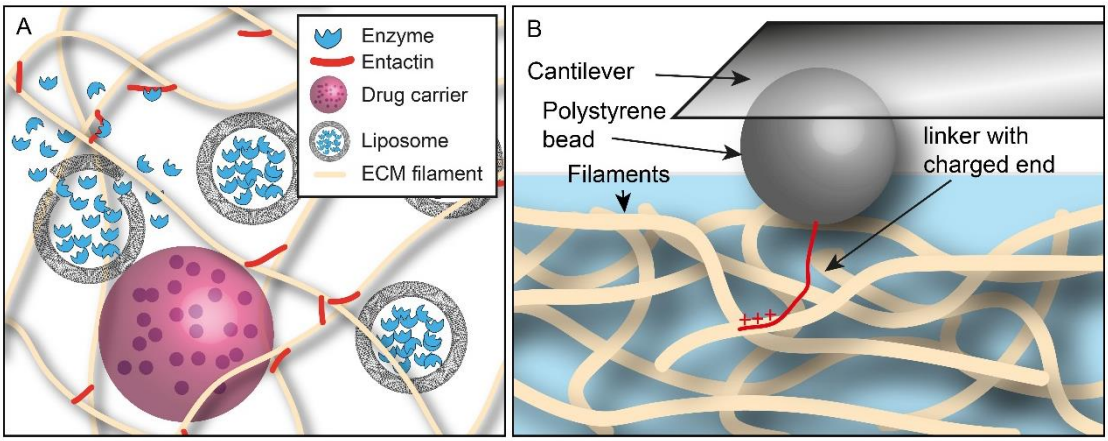

Figure 8. (A) Enzymes are released from liposomes upon binding to a basal lamina component, e.g. collagen IV. The enzymes digest the crosslinking molecules resulting in an increased mesh size. Larger drug carriers are then able to pass the matrix. (B) A long linker molecule with a charged group at the end is attached to a polystyrene bead at a cantilever. The linker is brought into contact with the ECM and the retraction force is measured.

In Section 4.2, a combination of electrostatic and hydrophobic interactions was identified to trap polystyrene particle in basal lamina gels. In a next step, it would be desirable to measure the exact interaction strength between the particles and the basal lamina gel. An instrument commonly used to measure forces in the range of pN is an atomic force microscope (AFM) [81]. An AFM basically consists of three components: a cantilever, a laser, and a position sensitive photo detector. The laser beam is reflected from the cantilever onto the detector which consists of four domains (quad-cell). Those four domains detect variations in the position of the laser beam which is changed by a deflection of the cantilever. The degree of the deflection depends on the force acting on the cantilever and can be calculated from the laser beam position on the photo detector [82]. AFM measurements can be conducted to determine e.g. the force acting between different materials [83,84], the force to extract lipids from a lipid bilayer [85] or the force needed to unfold a protein [86]. Such a force spectroscopy measurement might also be used to determine the force acting between particles and the basal lamina. An approach might be to attach components of the basal lamina to the cantilever tip and use polystyrene as a surface. In this case the polystyrene can be used without functional groups and solely the hydrophobic interactions between single basal lamina components and the polystyrene can be measured. When those forces are known, the

experiments can be repeated with a functionalized polystyrene surface, e.g. by introducing charged groups such as carboxyl or amino groups. Those experiments would then determine the total interaction strength. The strength of the electrostatic force acting between polystyrene and basal lamina components might be calculated by subtracting the hydrophobic part, measured with polystyrene alone, from the total interaction strength. One disadvantage of this approach is that every component has to be provided separately which can be challenging. In addition, only the individual contributions of the single components are determined, however, when acting together as a network the interactions strength might be different since not all potential binding spots might be available in a network. Another approach might be to attach a polystyrene particle to the cantilever tip and coat the basal lamina gel to a surface (Figure 8). With this experiment, the interaction strength of the whole network with the polystyrene particles would be measured. However both, electrostatic and hydrophobic interactions would contribute to the measured force. To entangle these two contributions, polystyrene particles without surface modifications might be used. Another possibility would be to attach a long linker molecule to the particle such that the particle has no contact with the basal lamina surface. In this scenario, the short-ranged hydrophobic interactions should not contribute to the interaction strength. However, multiple binding of linkers to the cantilever tip have to be considered. At the end of the linker a defined amount of charge would be deposited interacting with the basal lamina. This would gain insight into the strength of electrostatic interactions. Together with experiments in which polystyrene particles without linker are used, the contributions of hydrophobic and electrostatic interactions might be disentangled.

With the exact interactions strength between polystyrene particles and the basal lamina known, nanoparticles might be designed such that the interaction strength is on the order of the thermal energy. This would result in transient binding of the particles to the basal lamina network which would give rise to a decreased bulk diffusion coefficient in the gel. The exact value of this diffusion coefficient might be tuned by the interaction strength and thus by the time the particles are bound to the matrix. With this design of nanoparticles, retarded drug delivery might be achieved where the retardation depends on the amount of surface charge of the particles. Differently charged particles might be applied at once in a high concentration, however, due to their varying diffusion constants they would arrive at their intended target at different times.

In Section 4.3 it was shown that the positively charged peptides and dextrans accumulate at the basal lamina interface. Moreover, it was observed that within the basal lamina gel all peptides and dextrans showed a similar penetration profile. The height of the intensity peak and thus the amount of peptides bound at the interface was shown to depend on the amount of charge present on the peptides. The experimental results were reproduced by a simple diffusion-reaction equation which was numerically solved. For the reaction part of the equation, both a binding and unbinding constant were introduced. The numerical calculations showed that the height of the peak scales with the binding affinity and thus with the ratio of the binding and unbinding rate. This effect might be harnessed to increase the concentration of drug carriers at the basal lamina interface above its value in solution (partitioning effect). In principle, an optimal ratio between the binding affinity and the diffusion rate, which should be decreased when the binding affinity is increased, should exist such that with a lower drug carrier concentration in the “blood stream” a high concentration of drug carrier at the basal lamina interface is achieved. Despite the potentially retarded diffusion within the basal lamina the high concentration at the interface might result in a more efficient transport, i.e. higher drug carrier concentration within the basal lamina compared to non-interaction particles as illustrated in Figure 9. To find the optimal combination of binding, unbinding and diffusion rate, more numerical calculation need to be performed. With the results from those calculations the surface charge of particles might be adjusted, accordingly. The

microfluidic setup presented in Section 4.3 is well-suited to test if the numerically calculated profiles are also obtained experimentally and predict the diffusive spreading of “sticky” particles *in vivo*.

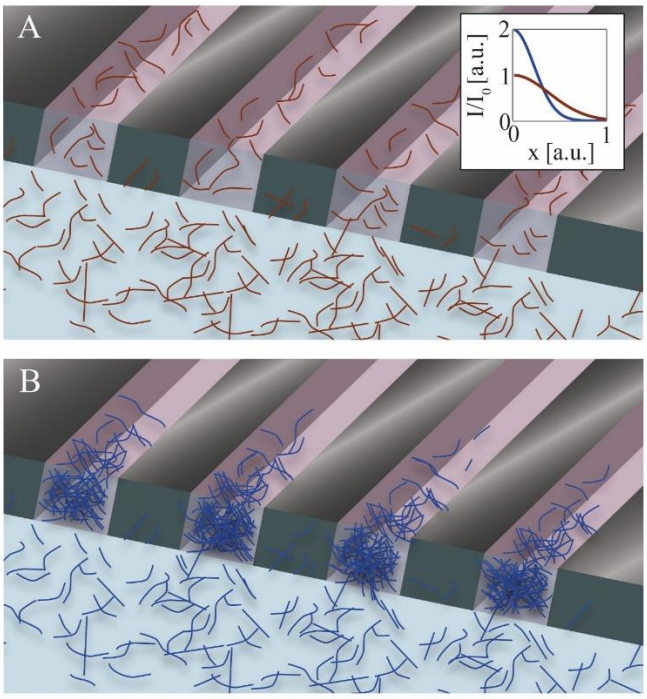

Figure 9. Illustration of the partitioning effect: (A) Test molecules (red rods) show no interaction with the basal lamina and diffuse fast from the buffer (light blue) into the gel compartment (light pink). (B) Test molecules (blue rods) accumulate at the basal lamina/buffer interface resulting in a high concentration at the interface and a slower diffusion into and in the gel. Inset: two exemplary penetration profiles for test molecules with weak (red line) and strong (blue line) binding affinity. The overall concentration of the accumulating molecules is higher in the first third of the gel compartment compared to the fast diffusing molecules. At longer distances from the interface, the highly mobile test molecules show a higher concentration.

The setup presented in Section 4.3 was designed to be as simple as possible but still be able to reproduce key results from *in vivo* experiments. However, to approach the complexity of an *in vivo* system, a more sophisticated setup design is needed. So far, only a basal lamina gel is incorporated in the chip, but the endothelial cell layer, which takes also part in the filter function of the vascular system, is still missing. Thus, the next step would be to design a microfluidic chip with a cell compartment adjacent to the already existing basal lamina compartment. For the incorporation of a cell layer into a microfluidic chip, a stable environment with a temperature of 37 °C, a cell-type dependent concentration of CO_2, and a continuous supply of fresh medium is required. Additionally, a robust filling method has to be established such that the gel and the cell compartment remains mechanically intact. When those challenges are overcome, various cell types can be cultured in such a microfluidic setup. In contrast to traditional cell culture, the microfluidic channel offers the possibility to apply a continuous flow to the cells. This is in particular interesting for endothelial cells since they are subject to shear stress in their natural environment. It was shown that endothelial cells need this shear stress to build up their *in vivo*

morphology [87]. Moreover, the *in vivo*-like production of certain components such as the glycocalyx layer is only observed when endothelial cells experience a shear stress exerted e.g. by a continuous flow [88-90]. However, it must be ensured that the cells are attached to the inner walls of the channel before a continuous flow is applied to prevent the cells from being flushed out of the channel. A compartment filled with basal lamina adjacent to the cell compartment will support cell adhesion and thus should reduce cell removal due to buffer flux. To even better mimic the *in vivo* situation, a layer of collagen I should be incorporated as well. With this setup, the overall structure of the vascular system together with the connective tissue should be reasonable well matched. The fine-tuning of parameters such as the flow velocity, the concentration of basal lamina and collagen I need to be done experimentally. When all challenges of the proposed setup are overcome, *in vivo* situations such as an inflammation could be mimicked. An inflammation response of endothelial cells is initiated by the tumor necrosis factor alpha (TNF-α) and results in a leakiness of the endothelium due to a disruption of intercellular junctions [38]. After the inflammation induction, particles might be inserted into the microfluidic channel and their translocation from the "blood stream" into the connective tissue can be observed. The influence of the basal lamina on the particle/molecule translocation is already known from previous experiments, thus any deviation from the previous results would be due to the newly introduced cell layer. A next step to add more complexity to this setup might be to introduce leukocytes into the channel and monitor their migration from the blood stream into the connective tissue. With this setup, the influence of drug carriers on leukocyte migration can be investigated. All these improvements of the setup presented in Section 4.3 might result in a model vascular system on chip with a high predictive power for *in vivo* behavior. In the long run, such a microfluidic tissue-on-chip platform has the potential to reduce the need for *in vivo* experiments by pre-testing drug delivery strategies on chip.

A Appendix

A.1 The Biophysical Properties of Basal Lamina Gels Depend on the Biochemical Composition of the Gel

PLOS ONE

RESEARCH ARTICLE

The Biophysical Properties of Basal Lamina Gels Depend on the Biochemical Composition of the Gel

Fabienna Arends[1,2☯], Constantin Nowald[1,2☯], Kerstin Pflieger[3], Kathrin Boettcher[1,2], Stefan Zahler[3], Oliver Lieleg[1,2]*

1 Institute of Medical Engineering IMETUM, Technische Universität München, Boltzmannstrasse 11, 85748, Garching, Germany, **2** Department of Mechanical Engineering, Technische Universität München, Boltzmannstrasse 15, 85748, Garching, Germany, **3** Department of Pharmacy—Center for Drug Research, Ludwig-Maximilians-Universität München, Butenandtstrasse 5–13, 81377, München, Germany

☯ These authors contributed equally to this work.
* oliver.lieleg@tum.de

OPEN ACCESS

Citation: Arends F, Nowald C, Pflieger K, Boettcher K, Zahler S, Lieleg O (2015) The Biophysical Properties of Basal Lamina Gels Depend on the Biochemical Composition of the Gel. PLoS ONE 10(2): e0118090. doi:10.1371/journal.pone.0118090

Academic Editor: Stephane Germain, Center for Interdisciplinary Research in Biology (CIRB) is a novel Collège de France / CNRS / INSERM, FRANCE

Received: July 17, 2014

Accepted: January 5, 2015

Published: February 17, 2015

Data Availability Statement: All relevant data are available at http://dx.doi.org/10.5282/ubm/data.64.

Funding: This work was supported by the Deutsche Forschungsgemeinschaft through project B7 "Nanoagents in 3-dimensional biopolymer hydrogels" and project B8 "Controlling Cellular Function by Structured Surfaces: Artificial Angiogenesis" in the framework of SFB 1032 (http://www.dfg.de/). The funders had no role in study design, data collection

Abstract

The migration of cells within a three-dimensional extracellular matrix (ECM) depends sensitively on the biochemical and biophysical properties of the matrix. An example for a biological ECM is given by reconstituted basal lamina gels purified from the Engelbreth-Holm-Swarm sarcoma of mice. Here, we compare four different commercial variants of this ECM, which have all been purified according to the same protocol. Nevertheless, in those gels, we detect strong differences in the migration behavior of leukocyte cells as well as in the Brownian motion of nanoparticles. We show that these differences correlate with the mechanical properties and the microarchitecture of the gels which in turn arise from small variations in their biochemical composition.

Introduction

In cell culture studies or tissue engineering applications, two different types of scaffolds are used to support cell proliferation, morphogenesis and differentiation: reconstituted matrices with purified biomacromolecules obtained from animal tissue or synthetic extracellular matrices (ECM). Both systems can be applied as surface coatings to promote cell adhesion, or they are used as a 3D environment for embedding cells to offer a more *in vivo*-like environment than a 2D system [1–3]. A critical advantage of an engineered scaffold is the opportunity to tune certain biophysical parameters, e.g. the mechanical properties or the permeability of the matrix and to investigate the influence of certain stimuli. On the other hand, ECM extracts from living cells may be better suited to approximate an *in vivo* environment in detail, especially if the biological macromolecules used to construct the scaffold are obtained from the same organism as the cells that are integrated into the matrix [4–6].

One of the simplest biopolymer model systems in use for constructing such a 3D scaffold is a reconstituted gel formed by collagen type I fibers. Macromolecules of the collagen family are

and analysis, decision to publish, or preparation of the manuscript.

Competing Interests: The authors have declared that no competing interests exist.

key constituents found in various tissues such as the connective tissue (collagen type I), the basal lamina (collagen type IV) and cartilage (collagen type II) [7–9]. The major part of the collagen in animals consists of type I, II and III which forms long thin fibrils. Collagen type IV molecules on the other hand assemble into a two-dimensional reticulum [9, 10]. However, they are not the only macromolecular components in those tissues, so the predictive strength of results obtained from cell culture experiments in such simple collagen matrices is limited. Of course, the degree of variability and the ensuing range of biophysical properties of a scaffold comprising only one macromolecular component are much lower compared to a scaffold consisting of several components. A more complex multi-component ECM model system is given by basal lamina gels that are typically purified from murine tissue. The basal lamina is situated at the basolateral side of the endothelium and separates the endothelial cells from the connective tissue. This specialized extracellular matrix is composed of three main macromolecular constituents, i.e. laminin, collagen IV and the perlecan complex, the latter of which combines three heparin sulphate chains into a finger-like structure which is attached to the biopolymer network. In addition to those macromolecular components, the cross-linking protein entactin (nidogen) is found in those basal lamina gels where it connects the collagen network with the laminin macromolecules [11]. Thus, such a basal lamina gel offers a much higher complexity and biologically more relevant environment than simple collagen gels [8,12–14].

There are several commercially available variants of basal lamina gels, and those variants are all purified from Engelbreth-Holm-Swarm sarcoma tissue of mice. Nevertheless, it is common practice not to mix and match basal lamina gels from different vendors or batches for a set of experiments. This practice is mostly based on experience and the notion that, even though those basal lamina gels all originate from the same tissue type and the preparation procedure applied is based on the same protocol established by Kleinman et al.[15,16], variations in the gel properties might still occur and thus affect the experimental outcome. However, to our knowledge, those putative variations in the gel properties have not been systematically quantified yet. A detailed understanding of how variations in the biophysical properties of those gels are regulated on a molecular level and how the gel properties in turn affect the behavior of embedded cells is still missing. Such information will not only simplify the interpretation of cell culture experiments but also provide important insights for the design of synthetic hydrogel scaffolds with tailored biophysical properties.

Here, we use basal lamina gel preparations obtained from four different suppliers as a platform to investigate how the biophysical properties of these gels depend on their biochemical composition. We analyze the motility of differentiated HL-60 cells in those gels, quantify the Brownian motion of nanoparticles in the gel and the viscoelastic properties of the gels, and compare their biochemical constitution and microstructure. Although all gel variants tested have been purified from the same tumor tissue of mice, we detect strong differences in the gel properties ranging from decreased permeability to increased stiffness and mild cytotoxic behavior. Those differences in the gel properties can be traced back to small variations in the molecular composition of the gel preparations which lead to differences in the gel architecture.

Materials and Methods

Basal lamina gels

All basal lamina gels used in this study are growth factor reduced and have been purified from the Engelbreth-Holm-Swarm sarcoma of mice. We note that, besides the main macromolecular components described in the main text, those basal lamina gels are also likely to contain minor amounts of molecules that originate from other tissue types [17] which is due to the particular purification process. The gels were obtained from the following four suppliers: Sigma Aldrich

(ECM1), BD Bioscience (ECM2), Trevigen (ECM3) and Life Technologies (Invitrogen) (ECM4). The protein concentration of the ECMs varied from c = 7.37 mg/mL (ECM1) to c = 15.65 mg/mL (ECM3) but was adjusted for the experiments to 3.5 mg/mL by dilution with Iscove's Modified Dulbecco's Medium (IMDM, PAA Laboratories GmbH, Pasching, Austria). Experimental results were checked with a second batch of gels from BD, Invitrogen and Trevigen. It was, however, not possible to obtain a second gel batch from Sigma-Aldrich. Thus, as an alternative, we used a non-growth factor reduced gel from Sigma to repeat all experiments except the cell migration studies, since the additional growth factors influence the outcome of this experiment and it would not be comparable to the results obtained before.

Polystyrene particles

Fluorescent polystyrene latex particles (carboxyl-terminated or amine-terminated) with a diameter of 200 nm were obtained from Invitrogen. Polyethyleneglycol (PEG, M_w = 750 Da, Rapp Polymere, Tübingen, Germany) coating of fluorescent 200 nm carboxyl-terminated latex beads was performed using a carbodiimide-coupling protocol [18]. Successful PEGylation was verified by determining the zeta-potential of the particles using dynamic light scattering implemented in a Zetasizer ZS (Malvern Instruments, Herrenberg, Germany). When suspended in 20 mM HEPES (Carl Roth, Karlsruhe, Germany) buffer at pH 7, we measured a zeta-potential of ζ = -38 mV for the carboxylated particles before PEGylation and ζ = -20 mV after PEGylation.

Particle diffusion experiments

For particle diffusion experiments, the ECM gels were thawed on ice and afterwards diluted with IMDM to a final protein concentration of 3.5 mg/mL. To induce gelation, all samples were incubated at their final protein concentrations in presence of the respective test particles at 37°C for 30 min. Particle trajectories were obtained and analyzed as described before [19]. In brief, movies of particles were acquired with a digital camera (Orca Flash 4.0 C11440, Hamamatsu, Japan) using the software Hokawo provided by Hamamatsu on an Axiovert 200 (Zeiss, Oberkochen, Germany) microscope with a 32 x objective (Zeiss, Oberkochen, Germany). The particle position was then determined for each frame by fitting a Gaussian to the x- and y-section of the intensity profile of each particle. Then, the mean-square displacement (MSD) was determined from the trajectory $\vec{r}(t)$ of a particle, as follows:

$$MSD(\tau) = \frac{1}{N}\sum_{i=1}^{N}\left[\vec{r}(i\Delta t + \tau) - \vec{r}(i\Delta t)\right]^2$$

Assuming normal diffusion, the mean-square displacement is related to the diffusion coefficient via $MSD(\tau) = 2nD\tau$, where $n = 2$ applies for the quasi-two-dimensional trajectories $\vec{r}(t) = (x(t), y(t))$ analyzed here. All particles with an apparent diffusion coefficient larger than D_{cut} = 1 $\mu m^2/s$, which is half the diffusion coefficient of a 200 nm-sized particle in water, were classified as "diffusing". In every sample, particles from at least three different fields of view were analyzed, and every experiment was repeated three times. That way, a total of at least 1000 particles were analyzed for each particle species.

Cell migration experiments

For cell migration experiments, the human promyelocytic leukemia cell line HL-60 (CCL-240, ATCC, Wesel, Germany) was used. This cell line was developed as a simple model system to study neutrophil cell migration without the need to derive cells from primary tissue [20]. HL-60 cells have several advantages over primary neutrophils, which include a significantly

longer life span and a higher reproducibility in their behavior. HL-60 cells can be maintained in culture, and can be terminally differentiated into migration-competent neutrophil-like cells (dHL-60) using dimethylsulfoxide (DMSO, Carl Roth, Karlsruhe, Germany). In brief, HL-60 cells were cultivated in IMDM supplemented with 15% heat-inactivated fetal bovine serum (FBS, PAA Laboratories GmbH, Pasching, Austria) at 37°C and 5% CO_2. Cells were grown in suspension until they reached a density between 1-2x10^6 cells/mL before they were passaged. To differentiate cells, 1.3% (v/v) DMSO was added to 2x10^5 cells/mL suspended in fresh IMDM+FBS. Upon differentiation, cells underwent clear morphological changes which were detected under a light microscope. Because cells are most active 4-5 days post-differentiation they were used after 4 days for cell migration experiments. An amount of 1x10^4 dHL-60 cells were suspended in ice-cold ECM samples as obtained from the four different suppliers and diluted with IMDM supplemented with N-formyl-methionine-leucine-phenylalanine (fMLP, Sigma-Aldrich, Schnelldorf, Germany) to a final concentration of 3.5 mg/mL ECM and 50 nM fMLP. The uniformly distributed chemoattractant fMLP triggered spatially homogeneous cell migration. A volume of 50 µL of each ECM/cell mixture was then transferred into one lane of a µ-Slide VI 0.4 (ibidi, Planegg/Martinsried, Germany) and incubated for 30 min at 37°C and 5% CO_2 in a cell incubator to allow for gel formation. After gelation, 50 µL of IMDM supplemented with 50 nM fMLP were added on top of the gel both at the inlet and outlet of the lane to allow for continuous nutrient supply and to minimize drying effects. Image acquisition for the migration experiments was performed on an Axiovert 200M microscope (Zeiss, Oberkochen, Germany) using a 10 x objective (Zeiss, Oberkochen, Germany). An incubation chamber mounted onto the microscope was used to control temperature and CO_2 concentration. Movies of migrating cells were recorded with an AxioCam digital camera (Zeiss, Oberkochen, Germany) using the software AxioVision V.4.8.20 (Zeiss, Oberkochen, Germany). To avoid artefacts arising from gel swelling, an initial adjustment time of 4 hours was provided. Then, phase contrast images were acquired every minute for 2 hours at different gel locations. The position of the cells in the gel matrices was determined with ImageJ 1.47d for every frame of the migration video, and the migration velocity was then calculated by multiplying the average migrated distance per frame with the frame rate. The Euclidean distance (*ED*) between the cell position at the start and the end of the evaluation was calculated with Chemotaxis and Migration Tool V2.0 (ibidi, Planegg/Martinsried, Germany) and averaged over all cells in the respective gel.

Rheology

The quantification of the viscoelastic properties as well as the gelation kinetics of the different ECM gels was performed on a stress-controlled macrorheometer (MCR 302, Anton Paar, Graz, Austria) with a 25 mm plate-plate geometry at a plate separation of 200 µm using a torque of 0.5 µNm and a frequency of 1 Hz ensuring linear response. The rheometer plate was cooled to 5°C before 150 µL of the samples were added, and gelation was induced by a sudden temperature change to 37°C. A thin layer of polydimethylsiloxane oil (ABCR, Karlsruhe, Germany) was applied to the outer rim of the sample to avoid drying artefacts. An applied oscillatory stress $\sigma = \sigma_0 \sin(\omega t)$ with a frequency ω resulted in an oscillatory strain with the same frequency, $\gamma = \gamma_0 \sin(\omega t + \delta)$, where δ denotes the phase shift between stress σ and strain γ. With those parameters, the storage modulus $G' = \sigma_0 / \gamma_0 \cos(\delta)$ can be calculated which is a measure for the elastic properties of the gel, and the loss modulus $G'' = \sigma_0 / \gamma_0 \sin(\delta)$ which is a measure for the viscous properties of the gel.

Western blots

For detection of proteins in western blot the following primary antibodies were used: the mouse monoclonal anti-fibronectin C6F10 (1:200 dilution), the rat monoclonal anti-nidogen

ELM1 (1:500 dilution) (sc-73611, sc-33706; Santa Cruz, Heidelberg, Germany), the rabbit polyclonal anti-collagen type IV (1:200 dilution) (AB756P; Millipore, Darmstadt, Germany) and the rabbit polyclonal anti-laminin (1:500 dilution) (L9393; Sigma-Aldrich, St.Louis, USA). The following secondary antibodies were used: anti-mouse IgG, HRP-linked (1:2000 dilution) (7076; Cell Signaling Technologies, Cambridge, UK), anti-rabbit IgG (H+L), HRP-linked (1:2000 dilution) (111–035–144; Dianova, Hamburg, Germany), anti-rat IgG (H+L), HRP-linked (1:2000 dilution) (6180–05; SouthernBiotech, Birmingham, USA) and anti-rabbit IgG (H+L), IRDye 800 (1:5000 dilution) (611–132–122; Rockland, Gilbertsville, USA). The ECM gels were thawed on ice and heated in Laemmli buffer at 95°C for 5 min. Equal amounts of protein were loaded on polyacrylamide gels. The proteins were separated by SDS-PAGE and transferred to nitrocellulose membranes using tank blotting. For the detection of protein levels, the ECL detection system (Amersham Pharmacia Biotech, Uppsala, Sweden) or Odyssey Infrared system version 2.1 (LI-COR Biosciences, Lincoln, USA) was used.

Confocal microscopy

The following antibodies were used for imaging applications: the goat polyclonal anti-collagen type IV (1:100 dilution) (sc-167526; Santa Cruz, Heidelberg, Germany) and the Alexa Fluor 680 donkey anti-goat IgG (H+L) (1:200 dilution) (A-21084; Life Technologies, Carlsbad, USA). For determining the gel microarchitecture with confocal microscopy, the ECM gels were thawed on ice and afterwards diluted with DMEM (Life Technologies, Carlsbad, USA) to a final protein concentration of 3.5 mg/mL. The gels were stained in μ-Slide Chemotaxis^{3D} (ibidi, Planegg/Martinsried, Germany). 6 μL of gel were injected into the observation channel of the slide and incubated for 30 minutes at 37°C, 5% CO_2. Afterwards the gels were fixed with 2% glutaraldehyde for 40 minutes and blocked with 1% bovine serum albumin (BSA) for 24 hours at 4°C. Subsequently, gels were incubated with primary antibodies, diluted 1:100 with 1% BSA for 72 hours at 4°C. Samples were washed three times with PBS (20 minutes) before incubation with secondary antibodies, diluted 1:200 with 1% BSA for 48 hours at 4°C. Images were obtained using a SP8 SMD confocal microscope (Leica, Wetzlar, Germany) and a 63 x HC PL APO 1.2 NA water objective (Leica, Wetzlar, Germany). The thickness of the optical slices was 0.9 μm.

Scanning electron microscopy

For scanning electron microscopy (SEM, JEOL-JSM-6060LV, Jeol, Eching, Germany) images, the gels were thawed on ice and diluted afterwards with IMDM to a final protein concentration of 3.5 mg/mL. A volume of 30 μL was pipetted onto a sample holder and incubated for 30 min at 37°C to induce gelation. The samples were fixed in 2.5% glutaraldehyde (in 50 mM HEPES, pH 7.4) for one hour and washed with ddH_2O for another hour. For dehydration, the samples were incubated in an increasing ethanol series of 50%, 70%, 80% and 99.8% ethanol for 30 min, each. Then, the samples were critical point dried, sputtered with a conductive gold film (40 mA, 40 s) and imaged at 5 kV.

Life-dead assay

For the life-dead assay tissue-culture treated 96-well plates were loaded with 50 μL of the different ECM gels at a final concentration of 3.5 mg/mL containing 50 nM fMLP and 1×10^4 dHL-60 cells as described above (see cell migration section). After gel formation for 30 min at 37°C and 5% CO_2 in a cell incubator 100 μL fresh IMDM containing 15% FBS and 50 nM fMLP were added on top to prevent drying effects. After additional 24 h of incubation in a cell incubator a live-dead staining was performed. For this 150 μL of a 4 μM calcein-AM/ethidium homodimer-

1 mix (Life Technologies, Darmstadt, Germany) in IMDM was added. Calcein-AM is green fluorescent in its activated conformation in the cytoplasm of vital cells activated by intracellular esterases. Ethidium homodimer-1 binds to DNA in the cell nucleus of dead cells possessing a damaged cell membrane. Accordingly, green appearing vital cells can easily be distinguished from dead red cells and counted by means of a fluorescent microscope. Image acquisition was performed after 1 h of incubation on an Axiovert 200M (Zeiss, Oberkochen, Germany) microscope using a 10 x objective (Zeiss, Oberkochen, Germany). Images were analyzes using ImageJ 1.47d.

Mass spectroscopy

The ECM gels were thawed on ice and heated in Laemmli buffer supplemented with 250 mM DTT (Sigma-Aldrich, Schnelldorf, Germany) at 95°C for 5 min. An amount of 30 μg of protein were loaded on a 4 – 20% gradient polyacrylamide gel (Bio Rad, München, Germany) respectively. The proteins were separated by SDS-PAGE and stained with a coomassie brilliant blue R-250 staining solution (Bio Rad, München, Germany). The band of interest was cut out and sent to the chemistry department (TUM, Garching, Germany) for trypsin digestion and subsequent MALDI TOF/TOF fingerprint mass spectroscopy.

Results and Discussion

Cell migration studies

Reconstituted extracellular matrices such as basal lamina gels are mostly used for embedding cells and analyzing their migration behavior as a function of distinct knock-out mutations or external (bio)chemical stimuli. There, the unperturbed migration activity of the cells in the gel matrix is typically used as a reference. Thus, in a first step, we conduct 3D cell migration experiments with dHL-60 cells using the four different ECM systems. Together with the cells, the chemoattractant fMLP is added to the gels before gelation is induced. Fig. 1 shows the trajectories of migrating dHL-60 cells as obtained 4 hours after gelation of the ECMs. This delayed observation time is chosen to exclude an influence of gel swelling (as it occurs during the first hours of the experiment) on the cell migration data. Each trajectory shown denotes the time-dependent cell position for a time course of 2 hours. The start point of all trajectories is shifted to the origin for clarity, and the end point is marked by a dot. As depicted in Fig. 1, the cells are able to efficiently migrate in ECM2, ECM3 and ECM4. Due to the uniform distribution of the chemoattractant, we observe random cell migration without any spatially oriented preference. The area covered by the trajectories varies depending on the gel used and is a measure for the migration activity. This area is similar for ECM3 and ECM4 whereas it is significantly smaller for ECM2. For ECM1, we are not able to detect any migratory activity, and the area covered by the trajectory ensemble is on the order of our tracking error. Another measure for the migratory activity is the Euclidean distance (*ED*) which is only $ED = (4 \pm 4)$ μm for cells embedded in ECM1 and $ED = (41 \pm 43)$ μm for ECM2. Again, ECM3 and ECM4 return very similar results with $ED = (112 \pm 90)$ μm for ECM3 and $ED = (132 \pm 92)$ μm for ECM4. An analysis of this data shows that only a fraction of $f = 10\%$ of the cells embedded in the ECM2 have an Euclidean distance greater than 105.5 μm (depicted by a red circle in Fig. 1) whereas in the gels of ECM3 and ECM4 we find $f = 44\%$ and $f = 51\%$. In ECM1 no cell has an ED greater than 105.5 μm, therefore $f = 0\%$. To further quantify those differences in the migratory behavior of the dHL-60 cells, the cell migration speed is calculated from the individual trajectories. When this velocity data is pooled for each cell population and compared in a box plot (Fig. 1e), the following differences between the distinct gel environments are observed: First, the median velocity of cells within ECM3 and ECM4 is higher than in ECM2, and the migration speeds determined for cells in ECM1 is close to zero. These findings agree well with our analysis of the total

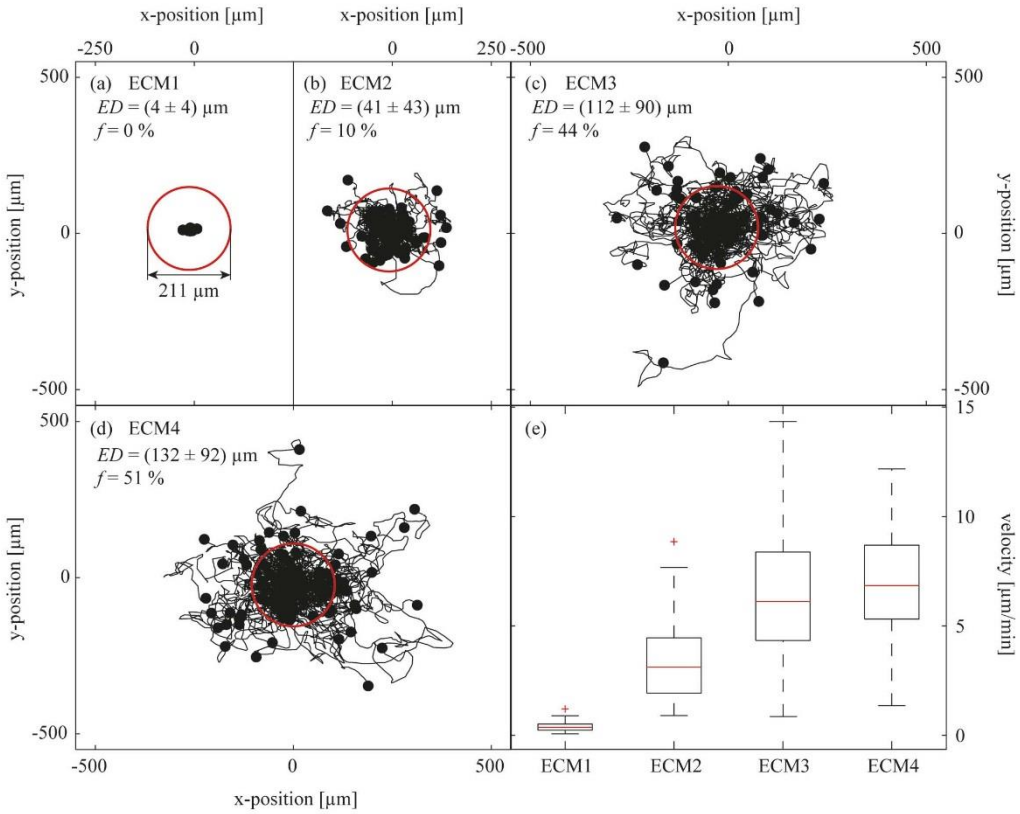

Fig 1. Migration trajectories of dHL-60 cells tracked from hours 4–6 after the cells are embedded into the four different basal lamina matrices. The starting point of all trajectories is shifted to the origin for clarity, and the end point is marked by a dot. The average start-to-end distance (Euclidean distance) travelled by the cells and the respective standard deviation is denoted by *ED*. The fraction of cells with an *ED* greater than *ED* = 105.5 µm (red circle) is denoted by *f*. (e) Comparison of the migration velocity of dHL60 cells in different ECM gels. The red line denotes the median of the velocity distribution, the box includes 25% of the observed velocities above and below this median, respectively. The remaining 25% of slower as well as the 25% of faster cells are indicated by the dashed lines. Outliers are denoted by a red cross.

doi:10.1371/journal.pone.0118090.g001

area explored by the migrating cell populations and the *ED*. Second, the distribution of migration speeds is quite broad both in ECM3 and ECM4, but more homogeneous in ECM2. Together, this data suggests that ECM3 and ECM4 offer the most efficient environment for dHL-60 migration whereas ECM2 seems to slow down the cellular migration activity and ECM1 completely suppresses dHL-60 cell migration. Apart from the suppressed migration we observe more dead cells in the ECM1 than in the other ECMs. To quantify this observation, a live/dead assay is performed. We determine a fraction of dead cells in the range of 5–10% for ECM2, ECM3 and ECM4, but at least twice as much, i.e. about 20% dead cells, are observed for ECM1 (see S1 Fig.). Whereas this finding already demonstrates that there are significant differences between the four gel variants, it cannot explain the differences in permeability of the gels towards migrating cells as only living cells are included in our analysis.

Particle diffusion and gel microarchitecture

As a next step, we further quantify the microscopic permeability properties of the different gels. Therefore, we choose fluorescent 200 nm-sized polystyrene beads as tracer particles, embed them into the gels and investigate their Brownian motion. Two important gel properties can be derived from such diffusion experiments with nanoparticles: First, information about the gel microstructure can be obtained when passivated nanoparticles are used that do not bind to the gel constituents. Second, the selective properties of the gel matrix can be mapped when particles with identical size but different surface modifications are compared [21]. Accordingly, we here compare the diffusion behavior of polystyrene particles carrying either COOH, NH_2 or polyethylenglycol (= PEG) groups on their surface. In a previous study with ECM1, we have observed that only particles with neutral or weakly charged surfaces are able to diffuse through those gels—provided that their size is smaller than the mesh size, i.e. the average spacing between neighboring macromolecule strands of the gel. However, the diffusion of strongly charged particles can be completely suppressed even for small particles. This behavior was attributed to binding events of the particles to the gel constituents [19,22]. Indeed, we observe similar charge dependent diffusion behavior here. We find that particles with COOH and NH_2 surface groups are immobilized in all gels demonstrating that the ECMs exhibit similar selective permeability properties towards charged nanoparticles. In contrast, the experiments with PEGylated particles show both diffusing and immobilized particles and exemplary trajectories are shown in Fig. 2a. The fraction of diffusing particles was (80 ± 1) % in ECM1, (77 ± 3) % in ECM3 and (73 ± 4) % in ECM4 (see also S1 Table). In contrast, all of those PEGylated particles are completely immobilized in ECM2. As particle PEGylation is expected to shield nanoparticles from adhesive interactions established by both electrostatic and hydrophobic forces [23–25], this suggests that the microarchitecture of ECM2 might be significantly different from that of the other gel variants, and that the Brownian motion of the PEGylated particles is obstructed by geometric hindrance effects imposed by a small mesh size.

If the average mesh size of ECM2 is indeed significantly smaller than in the other three gel variants, we might be able to directly detect differences in the gel architecture using fluorescence microscopy. To visualize the micromorphology of the four gels, collagen is stained with antibodies and images of the gel structure are obtained with a confocal microscope. The results shown in Fig. 2b confirm our previous notion based on the particle diffusion experiments: although all gels are diluted to the same final protein concentration of 3.5 mg/mL, ECM2 shows a much more homogeneous microstructure and a smaller mesh size than the other ECMs (for a higher magnification see S2 Fig. and for a second batch see S3 Fig.). However, the microstructure of ECM1, ECM3 and ECM4 appears to be very similar to each other with pores that seem to be at least tenfold larger than those found in ECM2.

To consolidate our findings obtained by fluorescence microscopy, we next analyze the microarchitecture of the gels by using scanning electron microscopy (SEM). In contrast to fluorescence microscopy, the whole network instead of only one component of the network is visualized. Fig. 2c and S2 Fig. show the SEM images obtained for the four gels. Again, ECM1, ECM3 and ECM4 have a similar microarchitecture whereas ECM2 shows a smaller pore size. In general, the mesh size of a gel can be decreased by increasing the concentration of protein. However, in our experiments the total protein amount is fixed at 3.5 mg/mL for all four gels, accordingly a smaller mesh size can only be achieved by thinner strands. Indeed, the fibers setting up the local meshwork in ECM2 are thinner than in the other gels and seem to contain less molecules per strand.

Viscoelastic properties of the gels

As the four gels seem to differ significantly in terms of their mesh size, one would also expect differences in their macroscopic viscoelastic properties. This expectation is based on our

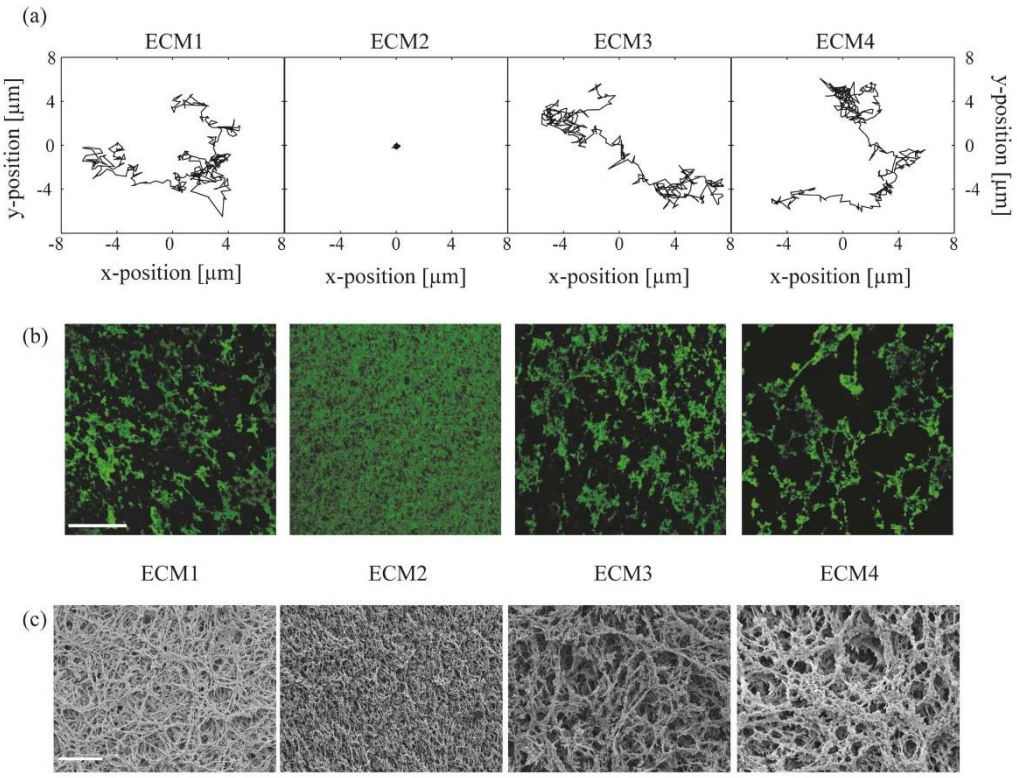

Fig 2. Micromorphology of the four gels determined by three different methods. (a) Exemplary trajectories of PEGylated particles with a diameter of 200 nm in the four different gels. Trajectories are shifted for clarity. (b) Micromorphology of the four different basal lamina gel variants as determined by confocal fluorescence microscopy. Representative staining of the matrix component collagen IV. The scale bar in the upper left image denotes 50 µm and applies to all images. (c) Micromorphology of the whole network of the four gel variants imaged by SEM. The scale bar corresponds to 25 µm and applies to all images.

doi:10.1371/journal.pone.0118090.g002

experience with other biological hydrogels where the macromechanical properties of the gels depend on a range of factors. Those parameters include the concentration and micromechanical properties of the macromolecules, and the microarchitecture of the gel. The latter is described by the type of spatial configuration in the gel—be it a homogeneous or heterogeneous distribution of elements—and the mesh size [26,27]. We here assess the influence of the mesh size variations observed between ECM2 and the three other variants by quantifying the viscoelastic properties of the gels with a macrorheometer. Such a rheometer exerts shear forces on a given sample and measures the resulting sample deformation. From these two quantities, the storage modulus G' as well as the loss modulus G'' is calculated, where the former serves as a measure for the elastic properties of the material and the second gives a measure for the viscous properties of the sample.

The ECM gels used here are typically stored as a liquid at temperatures of 5°C or below and are known to form a viscoelastic gel at physiological temperatures. Thus, we first investigate the gelation kinetics of the gels. According to the manufacturers' information, all ECM variants

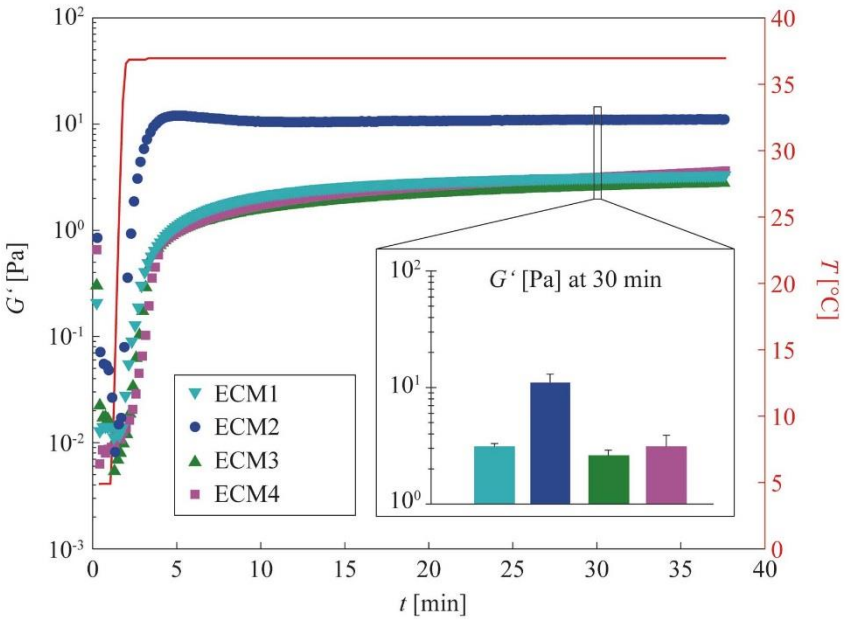

Fig 3. Gelation kinetics of the four different gels measured with a macrorheometer. The temperature is increased from 5°C to 37°C after one minute to induce gelation. The curves shown represent averages of three independent measurements. The inset shows the storage moduli *G'* of the four gels at 30 min. The error bars denote the error of the mean.

doi:10.1371/journal.pone.0118090.g003

should gel within the first few minutes when the samples are heated to 37°C. Again, all basal lamina variants are adjusted to the same total protein concentration of 3.5 mg/mL for experimental comparison. We observe efficient gel formation for all four gel variants, and no significant differences in the gelation kinetics are detected (Fig. 3).

Second, we compare the final elasticity the gels reach after complete gelation. We find that ECM1, ECM3 and ECM4 reach nearly identical final elasticities of $G' \sim 3$ Pa, whereas ECM2 shows a fourfold higher stiffness (inset of Fig. 3 and S4, S5 Figs.). This agrees with our notion that differences in the gel mesh size should manifest themselves in the viscoelastic properties of the gel.

Molecular composition of the gels

In our comparison of the four different basal lamina gel variants, we have observed strong differences in the migration activity and viability of embedded dHL-60 cells, the Brownian motion of nanoparticles and the macromechanical properties. Those findings are surprising considering that all gels are adjusted to the same total protein concentration and identical experimental conditions are chosen for each set of experiments: all cell migration experiments are conducted with the same cell population on the same microscope within an incubation chamber where the temperature as well as CO_2 concentration are controlled. Indeed we find that the gel stiffness, cell migration speed and particle diffusion correlate to a certain degree, and that this can be largely attributed to differences in the gel microarchitecture: small pore sizes cause higher gel stiffness and increased hindrance towards migrating cells and diffusing particles (ECM2),

while larger pores facilitate migration and diffusion (ECM3, ECM4). The only discrepancy in this correlation occurs for ECM1: here, on the one hand, mesh size, particle diffusion and stiffness are comparable with those of ECM3 and ECM4; on the other hand, the cell migration efficiency differs dramatically as compared to these gels.

In order to address this puzzling observation we examine the composition of the gels by electrophoresis. Whereas the overall pattern of protein bands in the coomassie staining is similar in all four gels (Fig. 4a and S6 Fig.), we detect some additional bands in ECM1, which are further analyzed by a proteomics approach. From mass spectroscopy analysis, the laminin subunits alpha1 and beta1 are identified in the additional band from ECM1 together with some proteins unrelated to the extracellular matrix (see S2 Table). These laminin subunit proteins have a molecular weight around 300 kDa and 200 kDa, respectively [28], but are detected at a size of approximately 50 kDa. This suggests that a proteolytic breakdown has occurred during the purification process. Already in the early times of laminin research, cellular activities of proteolytic laminin fragments with exposed cryptic motifs have been described [29]. This has been meanwhile corroborated by many publications [30,31]. However, a clear and systematic analysis of biological effects of the different fragments is still missing. We can only speculate that due to the manufacturing procedure proteolytic cleavage of laminin might have occurred in ECM1 and that the resulting fragments perhaps are responsible for the suppressed cell migration (e.g. via increased substrate adhesion).

Still, the question remains why ECM2 would be stiffer than the other gels. The stiffness of a biopolymer-based hydrogel is governed by several parameters: First, the concentration of biopolymers determines the elasticity, the more polymers the higher this value. However, the concentration of biological macromolecules with high molecular weight is comparable for all gels when the total protein concentration is adjusted—which rules out this simple explanation. Second, the amount of cross-linking molecules determines the stiffness of the gel: the gel stiffness is increased with increasing concentrations of cross-linking molecules. Therefore, the higher stiffness of ECM2 could be due to a higher concentration of entactin, which acts as cross-linker between laminin and collagen IV in the basal lamina. The coomassie staining already hints towards quantitative differences in the gel composition which are further analyzed by western blot. The comparison of four main matrix constituents (fibronectin, laminin, entactin, and collagen IV) shows that in tendency all of them are more concentrated in ECM2 (Fig.4b, Fig. 4c, S7 Fig. and S8 Fig.). The most dramatic difference is detected for entactin, which is nearly absent in ECM1, ECM3 and ECM4. This finding supports our previous notion that indeed the entactin concentration is responsible for the observed differences in macromechanical properties and also in the microarchitecture of the gels.

Conclusion

Here, we have investigated four commercially purified reconstituted variants of the basal lamina which were obtained from the same murine tissue following similar purification protocols. We detected variations in the concentration of the cross-linking protein entactin which entailed altered macromechanical properties as well as differences in the microarchitecture of the gels. This led to differences in the migration activity of dHL-60 cells and the Brownian motion of nanoparticles. Our findings demonstrate how sensitively the biophysical properties of a multi-component scaffold can depend on the concentration of a single component. In fact, entactin—compared to the content of the other macromolecular components of the basal lamina, i.e. laminin, collagen IV and heparan sulfate—is often considered to be a minor player only. Our results also suggest that proteolytic break-down of laminin observed in one of the gel variants led to the presence of protein fragments that severely hampered leukocyte migration activity—a mechanism that might also play an important role *in vivo*.

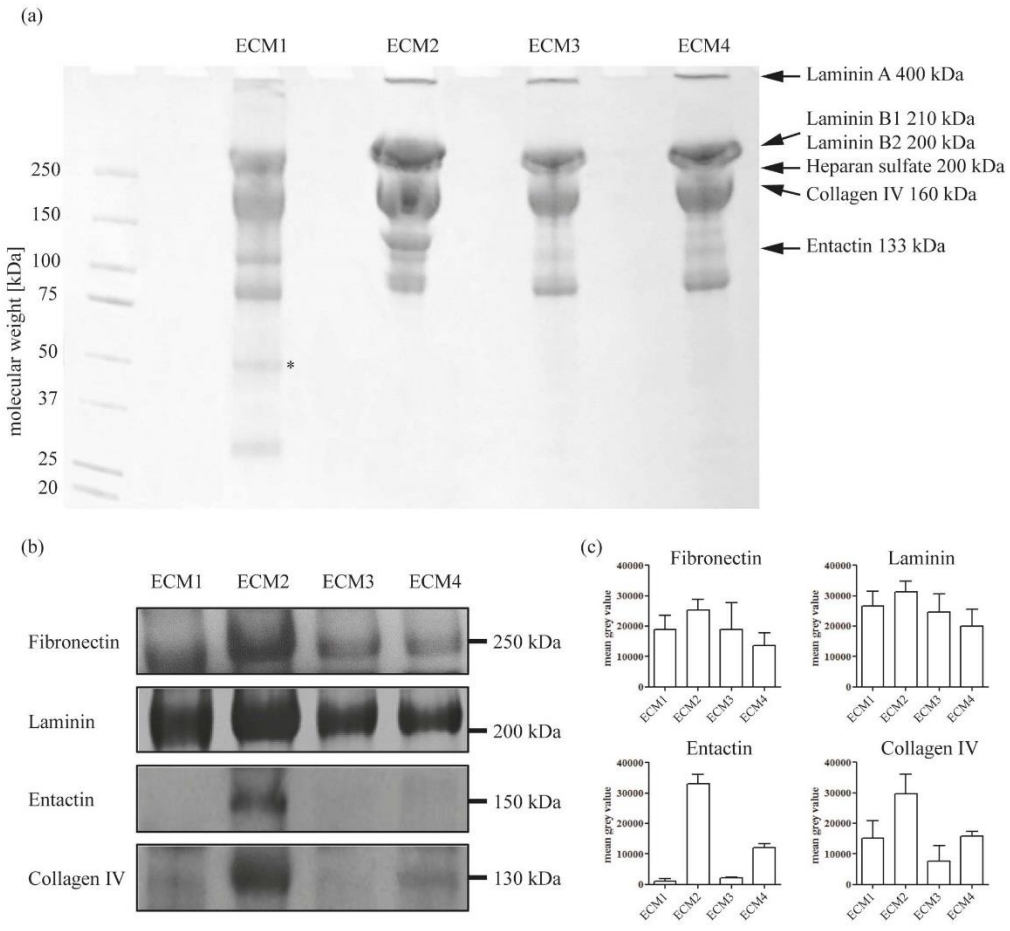

Fig 4. Content of selected ECM proteins in the four different ECM gel variants. (a) A coomassie staining of the four gel variants shows extra bands in ECM1 at low molecular weight. The star denotes the band which is further investigated by mass spectroscopy (see S2 Table for details). (b) The content of fibronectin, laminin, entactin and collagen type IV in the four different ECM gels is analyzed by western blot (for uncropped blots see S7 Fig.). (c) Densiometric analysis of fibronectin, laminin, entactin and collagen IV signals. The error bars denote the standard deviations as obtained from four independent gel runs.

doi:10.1371/journal.pone.0118090.g004

Supporting Information

S1 Fig. Life dead assay for dHL-60 cells embedded in the four basal lamina variants. Dead cells are obtained in all gels, but the amount differs drastically between ECM1 (about 20% dead cells) and the other three variants (about 5-10% of dead cells).
(DOCX)

S2 Fig. Micromorphology of the four gel variants. (a) Magnification of the images obtained by fluorescence microscopy. The bar corresponds to 10 μm and applies to all images in the first row. (b) Images obtained with SEM at magnifications of 500x and 5000x. The scale bar in the upper row corresponds to 50 μm and in the lower row to 5 μm.
(DOCX)

S3 Fig. Micromorphology of the second batch of the ECM variants as determined by confocal fluorescence microscopy. Representative staining of the matrix component collagen IV. The scale bar in the upper left image denotes 50 μm and applies to all images.
(DOCX)

S4 Fig. Viscoelastic frequency spectrum obtained for the basal lamina variants. The storage moduli G' (full circles) dominate over the loss moduli G" (empty circles) for all gel variants. Moreover, the storage moduli of all gels are nearly constant over two decades of frequency. This allows us to define a plateau modulus G_0 for each of the gels: $G_{0,\ ECM1}$ = 3 Pa, $G_{0,\ ECM2}$ = 11 Pa, $G_{0,\ ECM3}$ = 3 Pa, $G_{0,\ ECM4}$ = 4 Pa. The measurement was performed on a stress-controlled macrorheometer (MCR 302, Anton Paar, Graz, Austria) with a 25 mm plate-plate geometry at a plate separation of 200 μm after 30 min gelation time at 37°C.
(DOCX)

S5 Fig. Rheological results for the second batch of the gels. Again, ECM2 shows a significant higher G' than the other three gel variants. The error bar denotes the error of the mean.
(DOCX)

S6 Fig. SDS-PAGE for second batch. There was no second batch of growth factor reduced ECM1 available therefore we used non-growth factor reduced (ngfr) ECM1 as a control. In ECM1 there is an additional band at 50 kDa which was not detected in the other ECMs.
(DOCX)

S7 Fig. Uncropped blots for detection of the ECM proteins entactin, laminin, collagen IV and fibronectin. The entactin blot shows non-specific bands at 130 kDa, 110 kDa and 100 kDa, which were identified by Paulsson et al (*Purification and structural characterization of intact and fragmented nidogen obtained from a tumor basement membrane*, Eur. J. Biochem. 156, 467–478 (1986)), as entactin fragments obtained under conditions with less stringent control of endogenous proteolysis. The unspecific bands occurring in the laminin blot might show laminin B1 and B2 (>200 kDa) as well as shorter proteolytic laminin fragments (130 and 72 kDa). Short proteolytic fragments might also occur in the collagen IV blot (72 kDa). This blot additionally shows non-specific bands in the region between 300 kDa and 180 kDa, which might be explained by cross-reactivity of the collagen IV-antibody with laminin and fibronectin. The non-specific bands in the fibronectin blot might be also due to short proteolytic fragments.
(DOCX)

S8 Fig. The content of fibronectin, laminin, entactin and collagen type IV in the second batch of the four different ECM gels is analyzed by western blot. Densiometric analysis of fibronectin, laminin, entactin and collagen IV signals. The error bars denote the standard deviations as obtained from three independent gel runs. ECM2 shows again the significantly highest amount of entactin.
(DOCX)

S1 Table. Analysis of particle tracking experiments for a second batch of the gels. Again, amine-terminated as well as carboxyl-terminated particles are immobile in all ECMs. ECM1,

ECM3 and ECM4 show a similar fraction of diffusing PEGylated particles whereas in ECM2 only immobile particles are detected.
(DOCX)

S2 Table. Results from mass spectroscopy analysis of the additional band of ECM1. Database: NCBInr 20140323, Taxonomy: Mus musculus, Type of search: Peptide mass fingerprint, Enzyme: Trypsin
(DOCX)

Author Contributions

Conceived and designed the experiments: FA CN KP KB SZ OL. Performed the experiments: FA CN KP KB. Analyzed the data: FA CN KP KB. Contributed reagents/materials/analysis tools: FA CN KP KB SZ OL. Wrote the paper: FA CN KP KB SZ OL.

References

1. Tibbitt MW, Anseth KS (2009) Hydrogels as extracellular matrix mimics for 3D cell culture. Biotechnol Bioeng 103: 655–663. doi: 10.1002/bit.22361 PMID: 19472329
2. Cukierman E, Pankov R, Stevens DR, Yamada KM (2001) Taking cell-matrix adhesions to the third dimension. Science 294: 1708–1712. PMID: 11721053
3. Abbott A (2003) Cell culture: biology's new dimension. Nature 424: 870–872. PMID: 12931155
4. Kleinman HK, Luckenbill-Edds L, Cannon FW, Sephel GC (1987) Use of extracellular matrix components for cell culture. Anal Biochem 166: 1–13. PMID: 3314585
5. Lutolf MP, Hubbell JA (2005) Synthetic biomaterials as instructive extracellular microenvironments for morphogenesis in tissue engineering. Nat Biotechnol 23: 47–55. PMID: 15637621
6. Rowley JA, Madlambayan G, Mooney DJ (1999) Alginate hydrogels as synthetic extracellular matrix materials. Biomaterials 20: 45–53. PMID: 9916770
7. Alberts B, et al. (2002) Molecular Biology of the Cell: Garland Science.
8. Kleinman HK, Martin GR (2005) Matrigel: Basement membrane matrix with biological activity. Seminars in Cancer Biology 15: 378–386. PMID: 15975825
9. LeBleu VS, MacDonald B, Kalluri R (2007) Structure and Function of Basement Membranes. Experimental Biology and Medicine 232: 1121–1129. PMID: 17895520
10. Lodish H, et al. (2000) Molecular Cell Biology: Macmillan education
11. Yurchenco PD, Patton BL (2009) Developmental and pathogenic mechanisms of basement membrane assembly. Curr Pharm Des 15: 1277–1294. PMID: 19355968
12. Nicosia RF, Ottinetti A (1990) Modulation of microvascular growth and morphogenesis by reconstituted basement membrane gel in three-dimensional cultures of rat aorta: a comparative study of angiogenesis in matrigel, collagen, fibrin, and plasma clot. In Vitro Cell Dev Biol 26: 119–128. PMID: 1690206
13. Philp D, Chen SS, Fitzgerald W, Orenstein J, Margolis L, et al. (2005) Complex extracellular matrices promote tissue-specific stem cell differentiation. Stem Cells 23: 288–296. PMID: 15671151
14. Kleinman HK, Philp D, Hoffman MP (2003) Role of the extracellular matrix in morphogenesis. Curr Opin Biotechnol 14: 526–532. PMID: 14580584
15. Kleinman HK, Mcgarvey ML, Hassell JR, Star VL, Cannon FB, et al. (1986) Basement-Membrane Complexes with Biological-Activity. Biochemistry 25: 312–318. PMID: 2937447
16. Kleinman HK, Mcgarvey ML, Liotta LA, Robey PG, Tryggvason K, et al. (1982) Isolation and Characterization of Type-Iv Procollagen, Laminin, and Heparan-Sulfate Proteoglycan from the Ehs Sarcoma. Biochemistry 21: 6188–6193. PMID: 6217835
17. Hughes CS, Postovit LM, Lajoie GA (2010) Matrigel: A complex protein mixture required for optimal growth of cell culture. Proteomics 10: 1886–1890. doi: 10.1002/pmic.200900758 PMID: 20162561
18. Schuster BS, Suk JS, Woodworth GF, Hanes J (2013) Nanoparticle diffusion in respiratory mucus from humans without lung disease. Biomaterials 34: 3439–3446. doi: 10.1016/j.biomaterials.2013.01.064 PMID: 23384790
19. Arends F, Baumgartel R, Lieleg O (2013) Ion-specific effects modulate the diffusive mobility of colloids in an extracellular matrix gel. Langmuir 29: 15965–15973. doi: 10.1021/la404016y PMID: 24320773

20. Collins SJ, Gallo RC, Gallagher RE (1977) Continuous growth and differentiation of human myeloid leukaemic cells in suspension culture. Nature 270: 347–349. PMID: 271272

21. Lieleg O, Ribbeck K (2011) Biological hydrogels as selective diffusion barriers. Trends in Cell Biology 21: 543–551. doi: 10.1016/j.tcb.2011.06.002 PMID: 21727007

22. Lieleg O, Baumgärtel RM, Bausch AR (2009) Selective Filtering of Particles by the Extracellular Matrix: An Electrostatic Bandpass. Biophysical Journal 97: 1569–1577. doi: 10.1016/j.bpj.2009.07.009 PMID: 19751661

23. Otsuka H, Nagasaki Y, Kataoka K (2003) PEGylated nanoparticles for biological and pharmaceutical applications. Adv Drug Deliv Rev 55: 403–419. PMID: 12628324

24. Jokerst JV, Lobovkina T, Zare RN, Gambhir SS (2011) Nanoparticle PEGylation for imaging and therapy. Nanomedicine (Lond) 6: 715–728. doi: 10.2217/nnm.11.19 PMID: 21718180

25. Owens DE 3rd, Peppas NA (2006) Opsonization, biodistribution, and pharmacokinetics of polymeric nanoparticles. Int J Pharm 307: 93–102. PMID: 16303268

26. Lieleg O, Claessens MMAE, Heussinger C, Frey E, Bausch AR (2007) Mechanics of bundled semiflexible polymer networks. Physical Review Letters 99. PMID: 18233608

27. Lieleg O, Claessens MMAE, Bausch AR (2010) Structure and dynamics of cross-linked actin networks. Soft Matter 6: 218–225.

28. Aumailley M (2013) The laminin family. Cell Adh Migr 7: 48–55. doi: 10.4161/cam.22826 PMID: 23263632

29. Aumailley M, Timpl R, Risau W (1991) Differences in laminin fragment interactions of normal and transformed endothelial cells. Exp Cell Res 196: 177–183. PMID: 1893933

30. Miyazaki T, Futaki S, Suemori H, Taniguchi Y, Yamada M, et al. (2012) Laminin E8 fragments support efficient adhesion and expansion of dissociated human pluripotent stem cells. Nat Commun 3: 1236. doi: 10.1038/ncomms2231 PMID: 23212365

31. Desban N, Lissitzky JC, Rousselle P, Duband JL (2006) alpha1beta1-integrin engagement to distinct laminin-1 domains orchestrates spreading, migration and survival of neural crest cells through independent signaling pathways. J Cell Sci 119: 3206–3218. PMID: 16847051

A.2 Supporting Information: The Biophysical Properties of Basal Lamina Gels Depend on the Biochemical Composition of the Gel

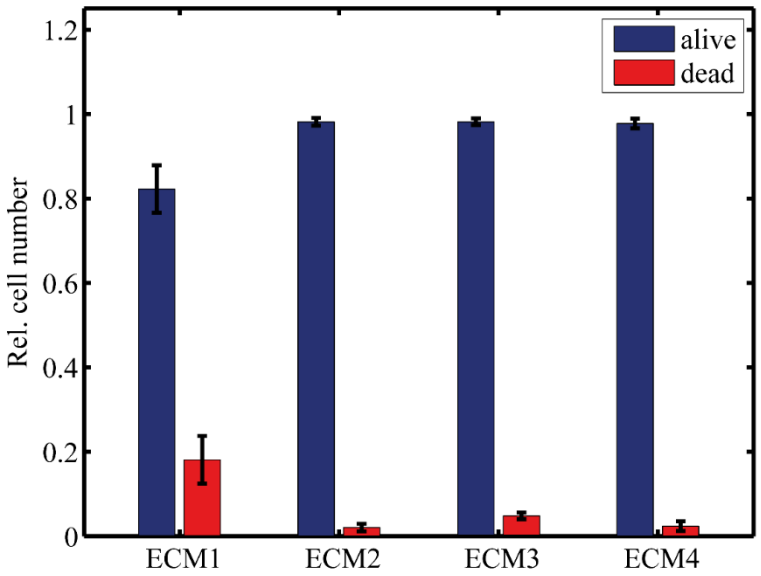

Figure S1. Life dead assay for dHL-60 cells embedded in the four basal lamina variants. Dead cells are obtained in all gels, but the amount differs drastically between ECM1 (about 20 % dead cells) and the other three variants (about 5-10 % of dead cells).

Table S1. Analysis of particle tracking experiments for a second batch of the gels. Again, amine-terminated as well as carboxyl-terminated particles are immobile in all ECMs. ECM1, ECM3 and ECM4 show a similar fraction of diffusing PEGylated particles whereas in ECM2 only immobile particles are detected.

	Amine	Carboxyl	PEG
ECM1	0	0	(84 ± 12) %
ECM2	0	0	0 %
ECM3	0	0	(71 ± 7) %
ECM4	0	0	(74 ± 2) %

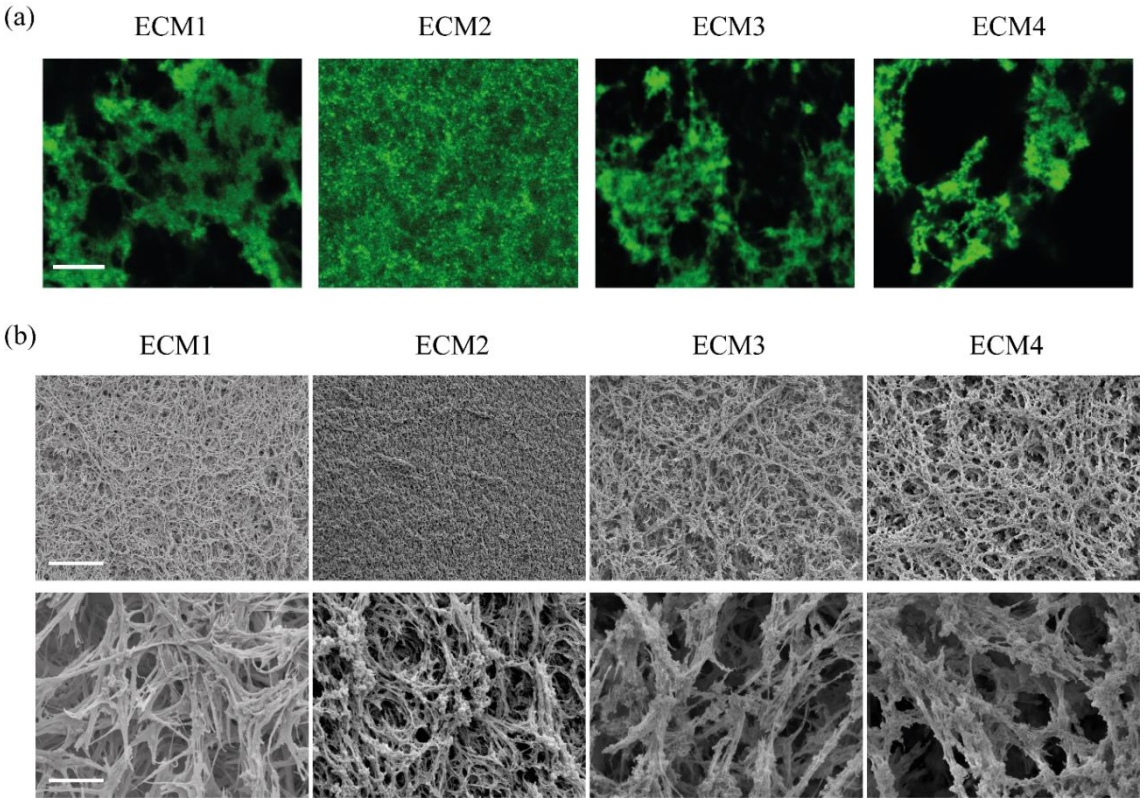

Figure S2. Micromorphology of the four gel variants. (a) Magnification of the images obtained by fluorescence microscopy. The bar corresponds to 10 µm and applies to all images in the first row. (b) Images obtained with SEM at magnifications of 500x and 5000x. The scale bar in the upper row corresponds to 50 µm and in the lower row to 5 µm.

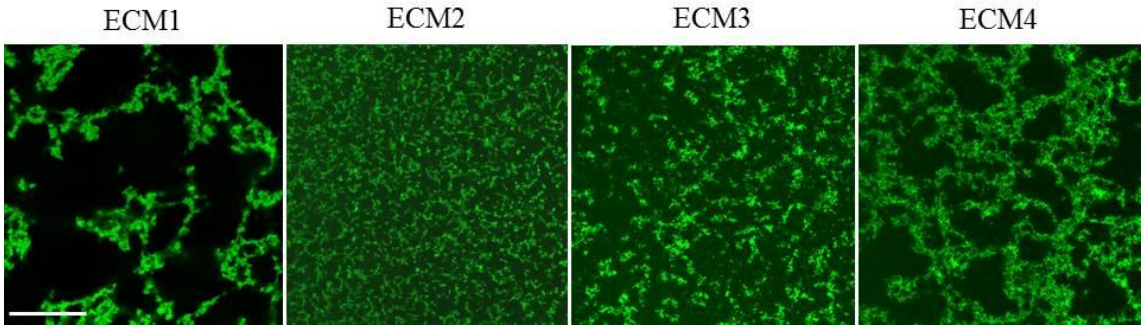

Figure S3. Micromorphology of the second batch of the ECM variants as determined by confocal fluorescence microscopy. Representative staining of the matrix component collagen IV. The scale bar in the upper left image denotes 50 µm and applies to all images.

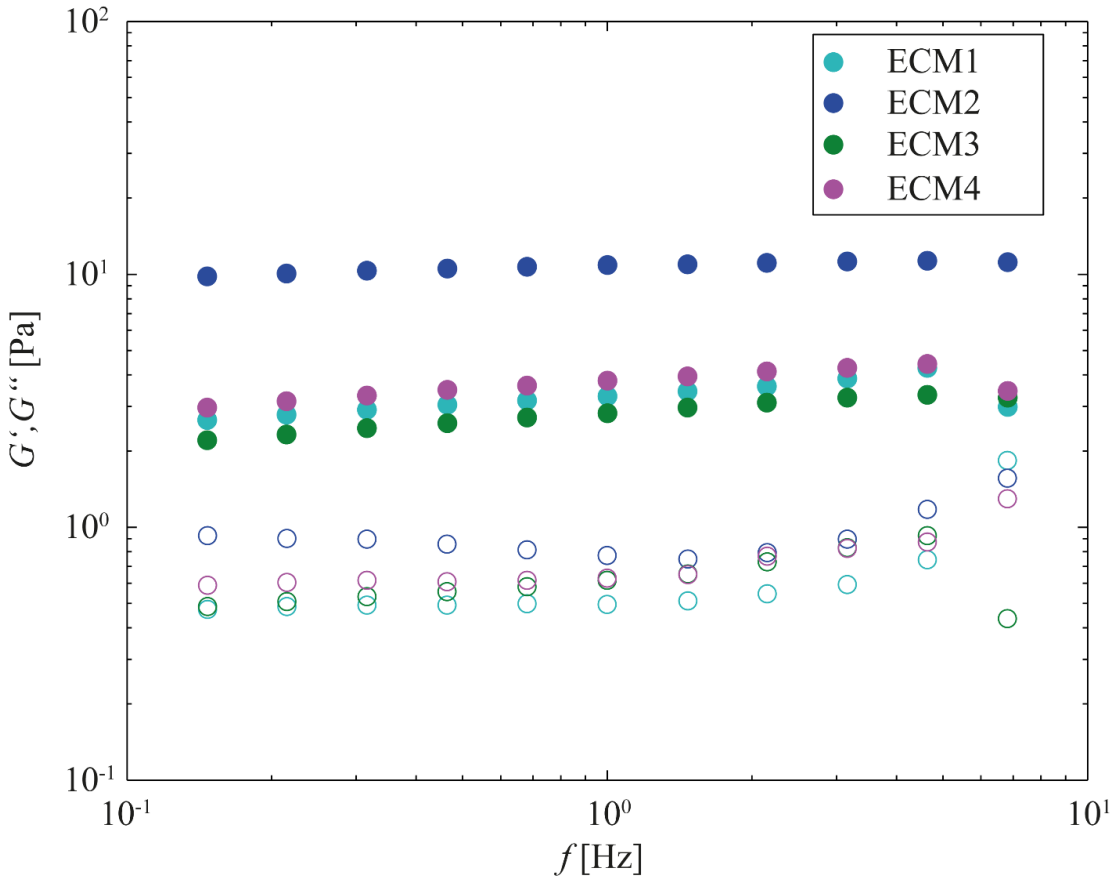

Figure S4. Viscoelastic frequency spectrum obtained for the basal lamina variants. The storage moduli G' (full circles) dominate over the loss moduli G'' (empty circles) for all gel variants. Moreover, the storage moduli of all gels are nearly constant over two decades of frequency. This allows us to define a plateau modulus G_0 for each of the gels: $G_{0,ECM1}$ = 3 Pa, $G_{0,ECM2}$ = 11 Pa, $G_{0,ECM3}$ = 3 Pa, $G_{0,ECM4}$ = 4 Pa. The measurement was performed on a stress-controlled macrorheometer (MCR 302, Anton Paar, Graz, Austria) with a 25 mm plate-plate geometry at a plate separation of 200 µm after 30 min gelation time at 37 °C.

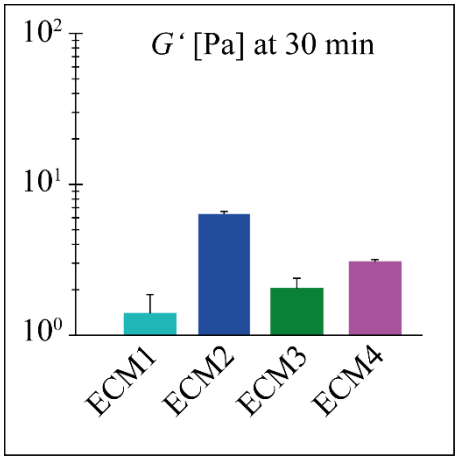

Figure S5. Rheological results for the second batch of the gels. Again, ECM2 shows a significant higher *G'* than the other three gel variants. The error bar denotes the error of the mean.

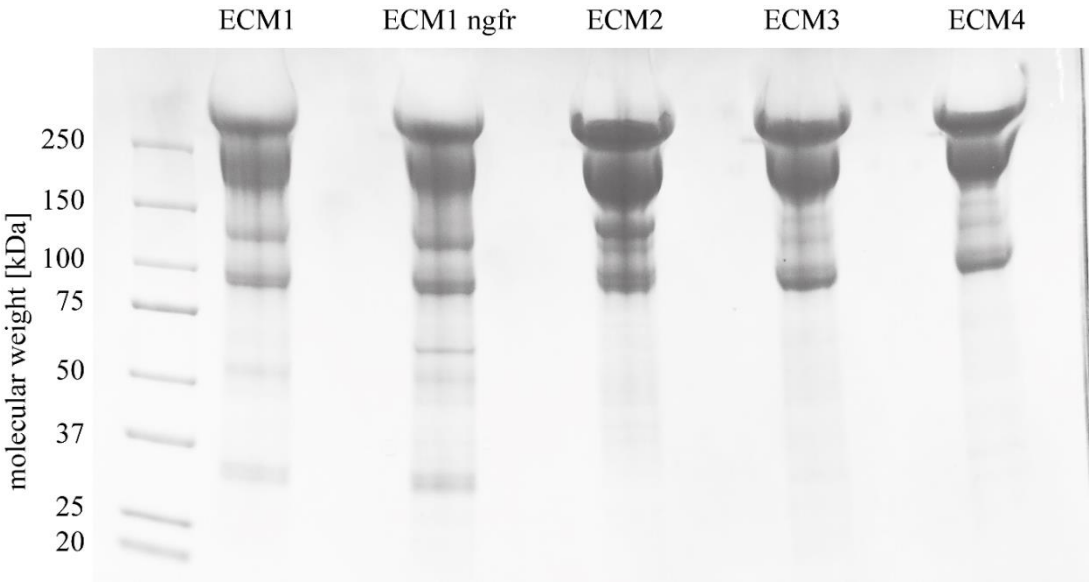

Figure S6. SDS-PAGE for second batch. There was no second batch of growth factor reduced ECM1 available therefore we used non-growth factor reduced (ngfr) ECM1 as a control. In ECM1 there is an additional band at 50 kDa which was not detected in the other ECMs.

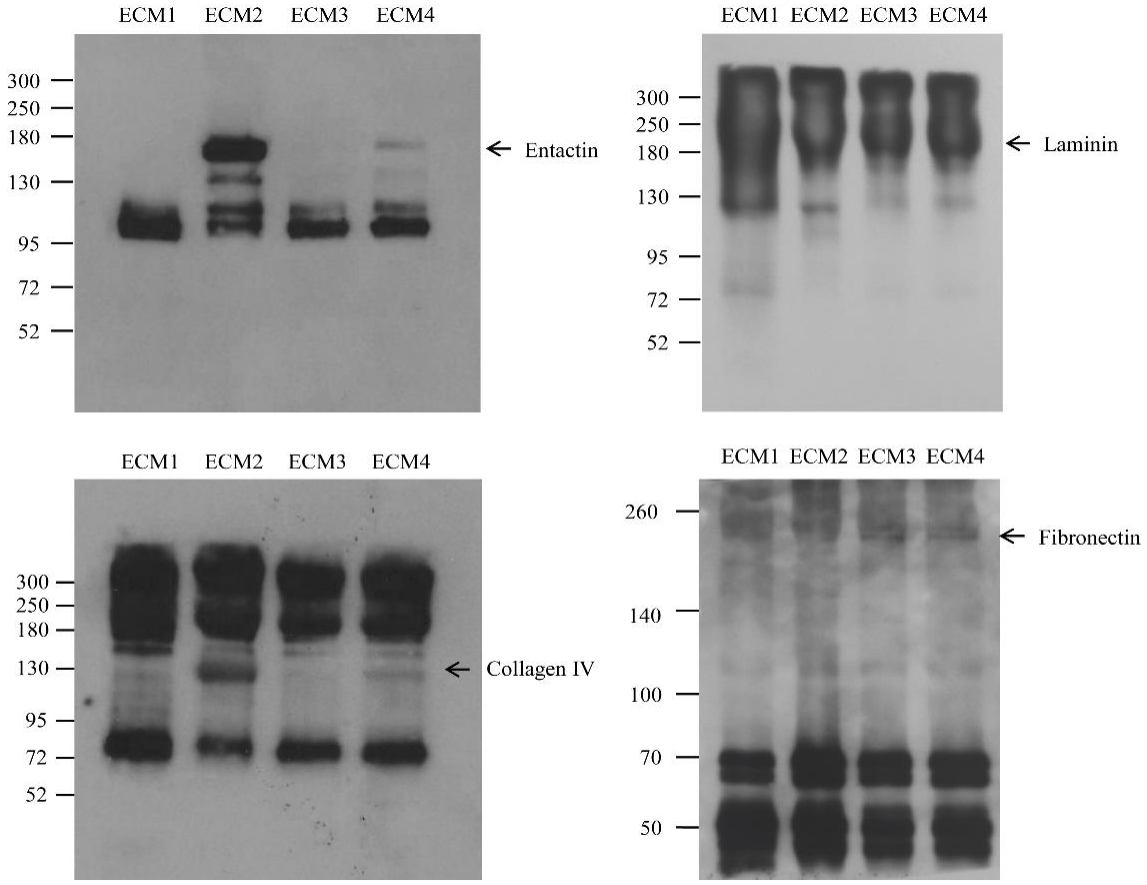

Figure S7. Uncropped blots for detection of the ECM proteins entactin, laminin, collagen IV and fibronectin. The entactin blot shows non-specific bands at 130 kDa, 110 kDa and 100 kDa, which were identified by Paulsson et al (*Purification and structural characterization of intact and fragmented nidogen obtained from a tumor basement membrane*, Eur. J. Biochem. 156, 467-478 (1986)), as entactin fragments obtained under conditions with less stringent control of endogenous proteolysis. The unspecific bands occurring in the laminin blot might show laminin B1 and B2 (>200 kDa) as well as shorter proteolytic laminin fragments (130 and 72 kDa). Short proteolytic fragments might also occur in the collagen IV blot (72 kDa). This blot additionally shows non-specific bands in the region between 300 kDa and 180 kDa, which might be explained by cross-reactivity of the collagen IV-antibody with laminin and fibronectin. The non-specific bands in the fibronectin blot might be also due to short proteolytic fragments.

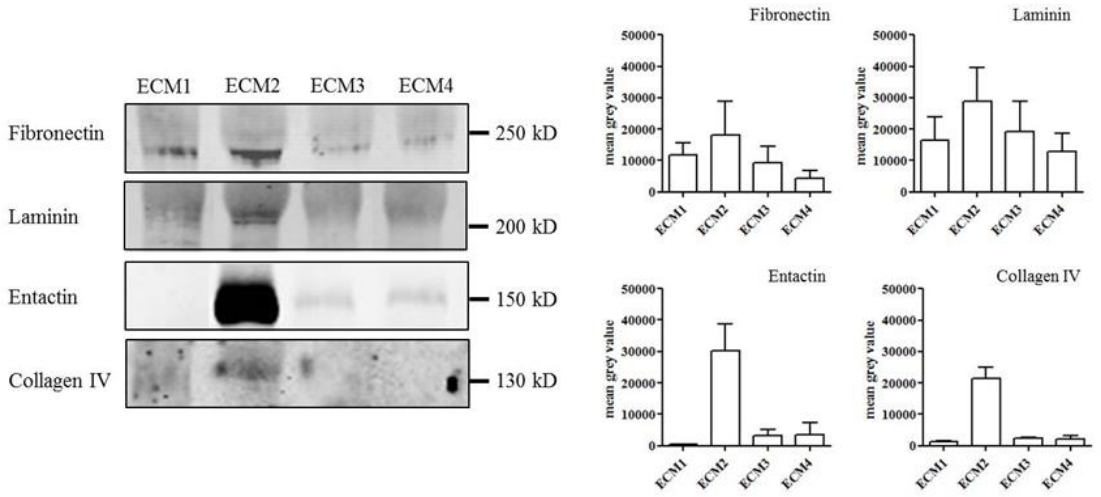

Figure S8. The content of fibronectin, laminin, entactin and collagen type IV in the second batch of the four different ECM gels is analyzed by western blot. Densiometric analysis of fibronectin, laminin, entactin and collagen IV signals. The error bars denote the standard deviations as obtained from three independent gel runs. ECM2 shows again the significantly highest amount of entactin.

Table S2. Results from mass spectroscopy analysis of the additional band of ECM1. Database: NCBInr 20140323, Taxonomy: Mus musculus, Type of search: Peptide mass fingerprint, Enzyme: Trypsin

	Mass	**Score**	**Expected**	**Matches**
gi|52858	37712	63	0.087	8
Hartl,L., Oberbaumer,I. and Deutzmann,R., *The N terminus of laminin A chain is homologous to the B chains*, Eur. J. Biochem. 173 (3), 629-635 (1988)				
gi|74224878	37746	46	4.1	8
gi|400977322	58595	31	1.5e+02	8
gi|111305466	63060	27	3.7e+02	7
gi|119226206	11651	45	5.2	5
gi|6531381	10720	32	1.2e+02	4
gi|74152705	12396	43	9.1	4
gi|74224092	15468	36	39	4
gi|148666045	54791	34	63	6
gi|15126700	33604	33	87	6
gi|19353516	48696	26	4.7e+02	6
gi|26346418	48757	26	4.7e+02	6
gi|269308251	48742	26	4.7e+02	6
gi|148694651	3714	33	95	2
gi|9837303	12897	32	1.2e+02	3
gi|347943574	6034	31	1.3e+02	3
gi|12853295	22326	30	1.7e+02	4
gi|18845005	17541	30	1.9e+02	4
gi|159162515	14644	30	1.9e+02	3
gi|148685215	33776	29	2e+02	4
gi|83627687	11276	29	2.2e+02	3
gi|289526642	4440	29	2.3e+02	2
gi|568912134	54738	29	2.3e+02	5
gi|568912132	55153	28	2.4e+02	5
gi|568912128	55368	28	2.5e+02	5
gi|568912108	60167	27	3.5e+02	5
gi|568912106	60582	27	3.7e+02	5
gi|568912104	60796	27	3.8e+02	5
gi|568912102	61195	26	3.9e+02	5
gi|568935374	102356	28	2.4e+02	6
gi|26343501	108941	27	3.1e+02	6
gi|164519057	108914	27	3.1e+02	6
gi|2558835	108928	27	3.1e+02	6
gi|50511047	64568	28	2.5e+02	6
gi|18044474	55932	28	3e+02	5
gi|67010061	56108	27	3.2e+02	5
gi341940401	55727	27	3.6e+02	5

gi|4249595	55743	27	3.6e+02	5
gi|254281186	59054	26	4.3e+02	5

A.3 Ion-Specific Effects Modulate the Diffusive Mobility of Colloids in an Extracellular Matrix Gel

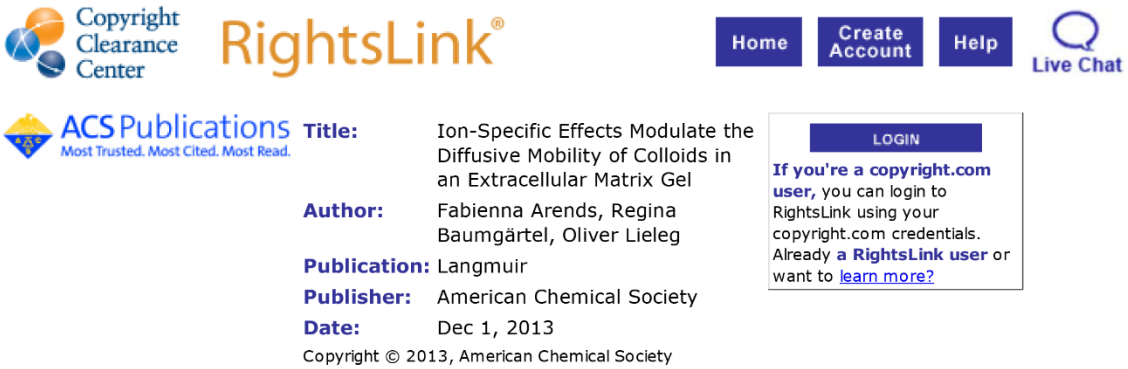

Copyright Clearance Center RightsLink®

Home | Create Account | Help | Live Chat

ACS Publications
Most Trusted. Most Cited. Most Read.

Title: Ion-Specific Effects Modulate the Diffusive Mobility of Colloids in an Extracellular Matrix Gel

Author: Fabienna Arends, Regina Baumgärtel, Oliver Lieleg

Publication: Langmuir

Publisher: American Chemical Society

Date: Dec 1, 2013

Copyright © 2013, American Chemical Society

LOGIN

If you're a copyright.com user, you can login to RightsLink using your copyright.com credentials. Already **a RightsLink user** or want to learn more?

PERMISSION/LICENSE IS GRANTED FOR YOUR ORDER AT NO CHARGE

This type of permission/license, instead of the standard Terms & Conditions, is sent to you because no fee is being charged for your order. Please note the following:

- Permission is granted for your request in both print and electronic formats, and translations.
- If figures and/or tables were requested, they may be adapted or used in part.
- Please print this page for your records and send a copy of it to your publisher/graduate school.
- Appropriate credit for the requested material should be given as follows: "Reprinted (adapted) with permission from (COMPLETE REFERENCE CITATION). Copyright (YEAR) American Chemical Society." Insert appropriate information in place of the capitalized words.
- One-time permission is granted only for the use specified in your request. No additional uses are granted (such as derivative works or other editions). For any other uses, please submit a new request.

BACK | CLOSE WINDOW

Langmuir

Article

pubs.acs.org/Langmuir

Ion-Specific Effects Modulate the Diffusive Mobility of Colloids in an Extracellular Matrix Gel

Fabienna Arends,[†,‡,⊥] Regina Baumgärtel,[§,⊥,∥] and Oliver Lieleg*[,†,‡]

[†]Zentralinstitut für Medizintechnik, Technische Universität München, Boltzmannstrasse 11, 85748 Garching, Germany

[‡]Fakultät für Maschinenwesen, Technische Universität München, Boltzmannstrasse 15, 85748 Garching, Germany

[§]Department of Biological Engineering, Massachusetts Institute of Technology, 77 Massachusetts Avenue, Cambridge, Massachusetts 02139, United States

Supporting Information

ABSTRACT: The diffusion of colloids in complex biological hydrogels is regulated by a broad range of factors including geometric constraints and different types of physical interactions between the particles and the hydrogel constituents. As a consequence, the particle mobility depends not only on the hydrogel microarchitecture but also on the detailed chemical composition of the hydrogel solvent. Here, we employ single particle tracking techniques to quantify the diffusion behavior of submicrometer-sized particles in such a biological hydrogel. We observe three states of colloid mobility: free diffusion, tightly and weakly bound particles, and transitions between those states. Finally, by comparing the efficiency of particle trapping in Matrigel as a function of the ionic strength of the hydrogel buffer, we show that ion-specific effects regulate the efficiency of this trapping process.

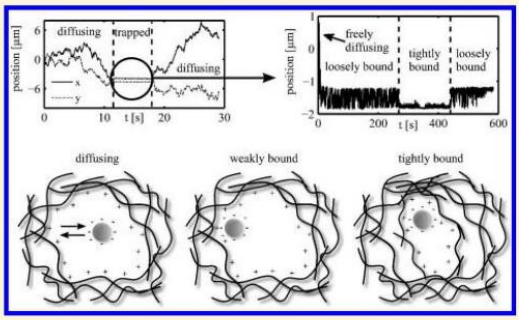

INTRODUCTION

Diffusion is a key mechanism in nature that helps to distribute molecules and particles in aqueous and gaseous environments. The physical laws of free diffusion are well understood, and the diffusion coefficient of a freely diffusing particle can be predicted with high accuracy on the basis of the fluctuation−dissipation theorem.[1] However, in more complex environments, where obstacles give rise to either geometric hindrance or particle binding effects, a detailed quantitative description of the ensuing particle diffusion behavior is difficult. To a large extent, this difficulty is based on a lack of clear experimental data that allow for distinguishing the impact of geometrical hindrance effects and particle binding events.[2]

A prominent example of such a complex biological environment is given by the basal lamina, a hydrogel that plays an important role in regulating diffusive processes. It is a specialized extracellular matrix which is located at the basolateral side of the endothelium and separates the endothelial cells from the connective tissue. This basal lamina is a multicomponent biological hydrogel which comprises several macromolecules, i.e., proteins and proteoglycans, including laminin, collagen IV, perlecan, and entactin.[3−5] A model system for native basal lamina gels is Matrigel, a complex mixture of macromolecules that is purified from the Engelbreth−Holm−Swarm sarcoma tissue of mice. Matrigel is commercially available and contains approximately 56% laminin, 31% collagen IV, and 8% entactin (according to the manufacturer's information). This commercial gel mimics the complex architecture of native basal lamina gels where the spatial relation between the two main components laminin and collagen IV is maintained by the small cross-linking molecule entactin. The glycosaminoglycan (GAG) molecule heparan sulfate is organized by the protein perlecan into the perlecan complex, which in turn links those GAG molecules to the collagen IV network. Due to its high protein content, Matrigel carries a negative net charge at neutral pH;[6] however, the pI values of its main constituents range from 4.82 to 8.85 (see Supporting Information for details). Furthermore, the amino acid sequence of the different hydrogel proteins combines both negative and positive residues, so the local charge distribution inside the hydrogel matrix can be expected to be heterogeneous.[7] Because of its ability to promote angiogenesis, cell differentiation, and proliferation of many cell types,[8−10] Matrigel is widely used as 3D matrix in cell culture experiments. However, the biophysical properties of Matrigel and how these properties depend on the detailed ionic content of the hydrogel buffer remain poorly understood.[11] One of those biophysical properties of Matrigel that has recently gained increased attention is the permeability of the gel.[12] This property plays an important role in drug delivery applications, where a drug carrier such as liposomes and polymeric or magnetic particles is applied via the bloodstream and needs to cross the basal lamina

Received: August 13, 2013
Revised: December 3, 2013
Published: December 9, 2013

in order to reach the connective tissue. When single particle tracking is used to analyze the diffusion of different micrometer-sized polystyrene particles in Matrigel hydrogels, an unexpected behavior is observed. At a total protein concentration of 4.3 mg/mL, where the mesh size of the hydrogel matrix is around 2−3 μm,[7,13] particles significantly smaller than this mesh size show a diffusion behavior that depends on their net charge: Only neutral particles can diffuse efficiently in the hydrogel. In contrast, charged particles of both algebraic signs are trapped in the hydrogel matrix.[7] However, it remains to be shown how this particle trapping process depends on the detailed chemical composition of the hydrogel buffer, and on what time scale trapping or escape events of particles occur in this biological hydrogel.

Here, we demonstrate that a combination of generic electrostatics and ion-specific interactions gives rise to an efficient but tunable immobilization of colloids in basal lamina hydrogels. We show that if the interaction strength between the colloids and the gel is sufficiently weakened by increasing the salt concentration of the hydrogel buffer, transient escape events of trapped particles occur on a time scale of several seconds. As a consequence, a particle ensemble can be divided into two general subsets: either mobile or immobile particles. Quantitative parameters obtained from the mean-square displacement (MSD) confirm this classification. We further show that the trapping efficiency of colloids depends not only on the ion concentration but also on the ion species demonstrating the relevance of ion-specific effects for the hydrogel permeability.

■ MATERIALS AND METHODS

Polystyrene Particles. Fluorescent polystyrene particles (carboxyl- or amine-terminated) with a diameter of 1 μm were obtained from Sigma-Aldrich. Carboxyl-terminated particles with a diameter of 0.3 μm were obtained from Magsphere (Pasadena, CA). Poly(ethylene glycol) (PEG) coating of 1.1 μm carboxyl-terminated latex beads (Interfacial Dynamics, Eugene, OR) was performed using a carbodiimide-coupling protocol as outlined in Valentine et al.[14]

Sample Preparation. Matrigel was obtained from Sigma-Aldrich. The complex Matrigel purified from the Engelbreth−Holm−Swarm sarcoma of mice has maintained its biological complexity[3,4] and is widely used as a model system for native basal lamina. For experiments, Matrigel was thawed overnight on ice and afterward diluted 1:1 with 20 mM HEPES buffer (pH 7.5) to a final protein concentration of 4.3 mg/mL. The ionic strength was adjusted with different salts as indicated in the individual experiments. To test the effect of mono- and divalent ions on the mobility of the particles, Matrigel was diluted 1:1 with MEM-α (Minimum Essential Medium Alpha, Invitrogen, Karlsruhe, Germany; salt content: 117 mM NaCl, 26 mM $NaHCO_3$, 5 mM KCl, 1.8 mM $CaCl_2$, 0.8 mM $MgSO_4$; pH 6.8), and again, ionic strength was adjusted as desired by adding appropriate amounts of salts. The pH was checked after the addition of the various ions, but no significant change was observed. To induce gelation, all samples were incubated at their final protein concentrations in the presence of the respective test particles at 37 °C for 30 min. Macrorheological tests showed that the gelation of Matrigel was not impaired by the ionic conditions used in the experiments discussed here. For all ionic conditions tested here, the structural integrity of the sample was verified by phase contrast microscopy, and it was ensured that no increased particle aggregation compared to low-salt conditions occurred.

Data Acquisition. Bright-field and phase contrast images were obtained on a Nikon eclipse TE300 (Nikon, Tokyo, Japan) microscope with a 40× Plan Fluor LD 0.60 NA PH2 objective (Nikon). Movies were acquired with a digital camera (ProSilica GE680, Allied Vision Technologies, Stadtroda, Germany) in high-speed image acquisition mode at frame rates of typically 300 fps using an image acquisition software developed by Steve Wasserman at MIT.

Fluorescence microscopy for low-speed image acquisition (i.e., at frame rates of about 16 fps) was conducted on an Axioskop 2 MAT mot microscope (Zeiss, Oberkochen, Germany) equipped with an EC Epiplan-NEOFLUAR 50× HD-DIC objective (Zeiss). Images were acquired with a digital camera (Orca-R2 C10600, Hamamatsu, Japan) using the software HCImageLive provided by Hamamatsu.

In all cases, particle trajectories were obtained using the image analysis software OpenBox developed at TU München.[15] All trajectories obtained are 2-dimensional projections of 3-dimensional particle movements. The particle position was followed by a tracking algorithm using a two-dimensional Gaussian fit to the particle intensity profile. For a point source, the intensity distribution is well-approximated by a Gaussian, and an accuracy of 2 nm has been demonstrated for a particle tracking procedure using 2-dimensional Gaussian fits.[16] Whereas this Gaussian approximation does not hold true anymore for particles much larger than the wavelength of light, the intensity profiles of the 300 nm and 1 μm particles used here can still be well-approximated by a Gaussian fit, and the applied tracking procedure resulted in subpixel resolution.[15] From the two-dimensional intensity profile, single particles could clearly be distinguished from smaller aggregates (which were not evaluated).

Computer Simulations. Numerical simulations of freely diffusing particles were performed to evaluate the level of statistical uncertainties of the experimental data. Each coordinate of a simulated particle trajectory was generated by drawing a random number from a Gaussian probability distribution which is centered around zero. This was independently done for x- and y-coordinates. Both data sets—the one numerically generated and the one experimentally acquired—were evaluated with the same routine in order to ensure maximal comparability.

Data Analysis. To quantify the microscopic mobility of the test particles, the mean-square displacement is determined from the trajectory of motion of the particles as described before.[7] In brief, the mean-square displacement (MSD) can be determined from the trajectory $\vec{r}(t)$ of a particle, as follows:

$$\mathrm{MSD}(\tau) = \frac{1}{N}\sum_{i=1}^{N}[\vec{r}(i\Delta t + \tau) - \vec{r}(i\Delta t)]^2$$

To avoid artifacts arising from statistical limitations, only the first 10% of the MSD(τ) data are used to determine the apparent diffusion coefficient and the degree of subdiffusivity α (see main text). However, the portion of data sampled by these 1 s time windows does encompass the entire video length of 10 s. Assuming normal diffusion (α = 1), the mean-square displacement is related to the diffusion coefficient via $\mathrm{MSD}(\tau) = 2nD\tau$, where n = 2 applies for the quasi-two-dimensional trajectories $\vec{r}(t) = (x(t), y(t))$ analyzed here. The degree of subdiffusivity α can be determined by fitting a power law function $\mathrm{MSD}(\tau) = A + B\tau^{\alpha}$ to the short-time regime of MSD(τ). According to the value of α, the diffusive motion can be classified as subdiffusive (α < 1), normally diffusive (α = 1), or superdiffusive (α > 1).

To validate this methodology, it is applied to 1 μm particles freely floating in water. The obtained diffusion coefficient D_{H_2O} = 0.43 μm^2 s^{-1} can be related to the viscosity of water η_{H_2O} using the Einstein relation $D = k_BT/6\pi\eta R$, where $6\pi\eta R$ denotes the Stokes friction coefficient for a spherical particle of radius R. The obtained value of η_{H_2O} = 1.04 mPa·s matches the viscosity of water at room temperature very well. Also, we obtain an exponent α = 0.88 for an ensemble of 1 μm particles that are freely floating in water, which is reasonably close to the theoretically expected value of 1.

Classification of Mobile and Trapped Particles. To classify particles as mobile and immobile, videos of 10 s duration were analyzed in a fast-forward mode. In this mode, one can clearly distinguish between mobile and trapped particles. After a first rough classification into a mobile or a trapped state, it was checked if the particles change their state of mobility during the duration of the

video. If that was the case, the particles were assigned to the state they were in at the beginning of the video.

RESULTS AND DISCUSSION

So far, due to a lack of high enough temporal resolution during the image acquisition process, the mobility of test particles in Matrigel has been quantified under the assumption that the measured MSD curves are approximately linear in time, $\langle x^2 \rangle = 4D_{app}\tau$. Based on this assumption, an apparent diffusion coefficient D_{app} has been determined from the MSD curves of individual particle trajectories, and this apparent diffusion coefficient has been used to compare the diffusion behavior of charged and neutral particles.[7] A more detailed characterization of the particle trajectories requires a much larger amount of data points so that the calculated MSD curves are statistically robust. In principle, the amount of experimentally acquired data can be increased by two methods: either by increasing the observation time of the experiment or by increasing the temporal resolution of the imaging process. The first approach is not useful for our system for two reasons: First, at the high magnification necessary for good spatial resolution, particles that show a nearly free diffusion behavior leave the focal plane of the microscope after a few tens of seconds, and thus a prolonged observation is hardly feasible. Second, for colloids that are only 2−3 times smaller than the hydrogel mesh size, geometric hindrance effects will influence the particle diffusion behavior on long time scales—which might result in a lower D_{app}. Thus, we here conduct high-speed microscopy using image acquisition rates of typically 300 fps. With this technique, we increase the temporal resolution by a factor of ∼20 compared to our previous study,[7] enabling us to determine not only an apparent diffusion coefficient but also the detailed time dependence of the MSD curves.

Apparent Diffusion Coefficient and the Slope of the MSD Curves of Particles Diffusing in Matrigel Are Correlated. Our previous experiments with Matrigel showed that at low salt concentrations both amine- and carboxyl-terminated particles were efficiently trapped within the hydrogel, whereas PEGylated particles showed nearly free diffusion. To investigate if this binary behavior changes on shorter time scales, we conduct high-speed microscopy with charged and neutral polystyrene particles in Matrigel buffered with HEPES to a pH of 7.5 and a final ionic strength of 100 mM KCl. As depicted in Figure 1 and Figure S1, this binary behavior is confirmed by our high-speed particle tracking experiments. We observe only two types of behavior for 1 μm sized polystyrene particles: both amine- and carboxyl-terminated (and thus strongly charged) polystyrene particles are trapped and therefore do not diffuse, whereas PEGylated (and thus weakly charged) particles of the same size show rapid diffusion. This finding demonstrates that on short time scales as studied here geometric hindrance effects do not significantly influence the diffusion of micrometer-sized particles in Matrigel.

Increasing the ionic strength of the buffer can entail a remobilization of formerly trapped particles.[7] This finding underscores the importance of electrostatic interactions occurring between charged particles and the hydrogel matrix since the addition of counterions results in charge screening effects (referred to as Debye screening in the literature). It is *a priori* unclear whether a binary behavior as observed for low-salt conditions also applies for the diffusion behavior of charged particles in Matrigel at high ionic strengths. Thus, in a next step, we aim at analyzing the trajectories of such particles in high-salt samples.

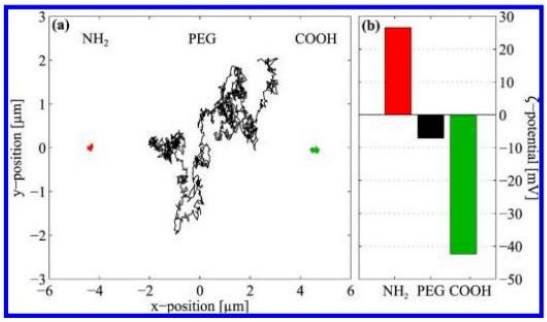

Figure 1. Diffusive mobility of 1 μm sized particles in Matrigel is determined by their net charge. (a) Trajectories in the x−y-plane of three exemplary particles recorded with high-speed microscopy (300 fps) in Matrigel diluted with HEPES buffer at pH 7.5 containing 100 mM KCl (trajectories are shifted for clarity). The respective ζ-potential of the particles is shown in (b). The particles possess distinct surface groups, i.e., NH_2 (red), COOH (green), and PEGylated (black). Amine-terminated particles have a highly positive ζ-potential and are completely immobilized in the gel matrix. The same behavior is obtained for carboxyl-terminated particles whose ζ-potential is highly negative. In contrast, the ζ-potential of PEGylated particles is only weakly negative and those particles show an efficient diffusion behavior.

For freely diffusing particles, the mean-square displacement scales linearly with time, $\langle x^2 \rangle \propto D\tau$, and the coefficient D is referred to as the diffusion constant. However, in complex environments such as hydrogels, the time dependence of the MSD may be more complicated exhibiting a power law behavior, $\langle x^2 \rangle \propto \tau^{\alpha}$. In the case of subdiffusion, the exponent α would be smaller than one whereas active transport processes, as they e.g. occur in living cells, will return α-values larger than one. The data obtained by high-speed microscopy now enable us not only to determine the apparent diffusion coefficient for our particles as in previous experiments but also allow us to clearly assess the exponent α and hence to differentiate between free and restricted diffusion. Such a detailed examination of our tracking data shows that at high-salt conditions, i.e. at an ionic strength of 1 M KCl, the PEGylated polystyrene particles are not only almost all mobile, but their MSD curves also exhibit an exponent in the range of 0.6−1 (Figure 2). In contrast, for particles with NH_2 surface groups we find not only a broad range of apparent diffusion coefficients but also a broad distribution of α-values. A similar result is obtained for particles with COOH groups on their surface, yet here the majority of particles remains trapped.

The broad range of α-values observed with high-speed imaging seems to challenge our previous approach where we described, due to lack of high enough statistics, the mobility of particles with an apparent diffusion coefficient assuming a linear time dependence of the MSD. However, the particle trajectories and their associated MSD curves shown in Figure 2 imply a distinct relation between the apparent diffusion coefficient D_{app} and the exponent α. Indeed, as the exponent α decreases, the apparent diffusion coefficient decreases monotonously as well (Figure 2d). This result, in retrospect, justifies our approach to use D_{app} as a simplified measure for the mobility of particles diffusing in Matrigel.

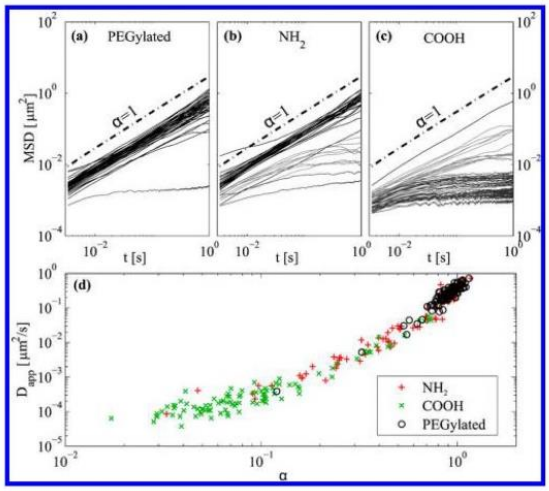

Figure 2. From the particle trajectories, mean-square displacement curves are calculated for (a) PEGylated, (b) amine-terminated, and (c) carboxyl-terminated polystyrene particles of 1 μm diameter. Matrigel was diluted with HEPES buffer (pH 7.5), and the ionic strength was adjusted to 1 M KCl. (d) The exponent α characterizing the time dependence of the MSD curves is compared for PEGylated (black circles), amine-terminated (red crosses), and carboxyl-terminated (green tilted crosses) particles. α exhibits a distinct mathematical relation to the apparent diffusion coefficient.

The existence of a broad distribution of apparent diffusion coefficients and α values depicted in Figure 2 suggests the existence of three distinct regimes: fully immobilized particles, subdiffusive particles, and freely diffusing particles. To test whether those variations in D_{app} are indeed meaningful or whether they rather arise from statistical uncertainties, we performed numerical simulations of freely diffusing particles and quantified their trajectories in comparison to the experimental ones (see Materials and Methods and Supporting Information for details). The apparent diffusion coefficients as well as the respective exponents α obtained from numerical simulations show similar variations as a subset of the experimental data; i.e., they return α-values in the range of 0.7−1.2. This allows us to conclude that we can classify all particles with experimental α-values larger than 0.7 as "mobile". Another subset of our particle MSD curves yields α-values close to zero—and indeed the trajectories of such particles are confined to an area close to the resolution limit of our tracking technique, demonstrating complete immobilization. We also find particles whose MSD curves exhibit α-values between 0.1 and 0.7 which are not easy to classify without further analysis. However, all curves with intermediate α-values approach a plateau after ∼0.5 s. This plateau value is on the order of 5×10^{-2} μm^2, which is at least 1 order of magnitude smaller than the corresponding value obtained for particles with approximately linear MSD curves. Also, the corresponding $x-y$ plots show a highly localized thermal motion for those particles. This suggests that those particles whose MSD curves return α-values between 0.1 and 0.7 can also be classified as "trapped".

In conclusion, our analysis indicates that also at high-salt conditions no real subdiffusive behavior occurs for colloids in Matrigel. Instead, even when screening effects by counterions weaken electrostatic interactions, there are still only two possible states for a given particle: either the particle is "trapped", or it shows nearly free diffusion; i.e., it can be classified as "mobile".

Transient Particle Trapping and Escape Events Take Place on Time Scales of a Few Seconds. We next ask if and under which conditions a given particle might be able to switch between its trapped and mobile state. Such escape and retrapping events would indicate binding of particles to and unbinding of particles from the hydrogel matrix. However, from our high-speed data, such escape/trapping events could not be observed. This suggests that putative binding/unbinding events occur either on time scales much shorter or much longer than

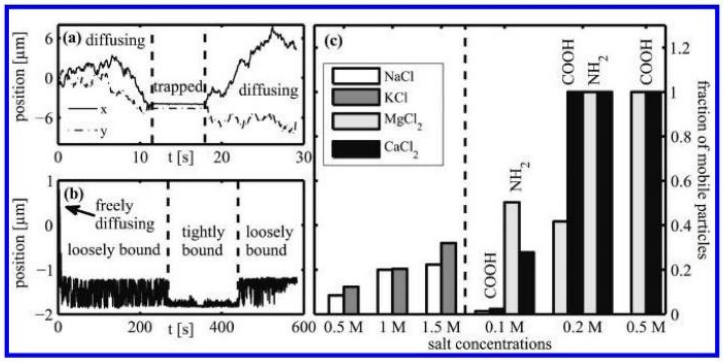

Figure 3. (a) The x- (solid line) and y-coordinates (dashed-dotted line) of a trajectory of a 300 nm polystyrene particle obtained from a Matrigel sample containing 1.5 M KCl is plotted as a function of time. The observed particle switches between a trapped and a freely diffusing state within several seconds. In (b) the x-coordinate of a particle trajectory obtained from a Matrigel sample containing 1.5 M KCl sample is shown over the course of several minutes. This particle exhibits three different states: free diffusion, a loosely bound and tightly bound state. Please note the different x- and y-scaling compared to subpanel (a). (c) The fraction of mobile particles is determined for particles with COOH surface groups at different concentrations of KCl, NaCl, $CaCl_2$, and $MgCl_2$. For all ions tested, increasing ion concentrations lead to an increased fraction of mobile particles. However, divalent ions are more efficient in remobilizing trapped particles than monovalent ions. Moreover, at intermediate concentrations of 0.2 M, $MgCl_2$ and $CaCl_2$ differ strongly in their ability to rescue trapped particles. This behavior is reversed when the surface group of the particles is changed to NH_2; here $MgCl_2$ is more efficient than $CaCl_2$ in remobilizing the colloids. For each condition, an ensemble of at least 300 particles has been analyzed.

our observation time. Further increasing the image acquisition rate of our particle tracking experiment is a technically highly challenging task. Instead, we extended our experimental time scale and switched back to standard-speed image acquisition using ∼16 fps. Of course, for those extended observation times geometric hindrance effects as imposed by the hydrogel mesh size will become increasingly important. Thus, to minimize geometrical constraints even on large time scales, we used 300 nm particles, which are 10 times smaller than the mesh size of the hydrogel, for these long-time observation experiments.

So far, we have used HEPES buffer for Matrigel dilution. However, Matrigel is mainly used in cell culture experiments where more physiological conditions are required. In order to replicate those physiological conditions, we next analyzed samples where MEM-α cell culture medium was used as a buffer for Matrigel dilution. MEM-α medium contains a total ion concentration of about 120 mM which mimics physiological conditions (see Materials and Methods for details). Using this MEM-α as a baseline buffer, we test whether we can detect escape and retrapping events of particles at varying KCl concentrations.

We recorded videos and scanned them in fast-forward mode in order to screen for binding and unbinding events. With this fast-forward mode, it is easy to pinpoint particles that suddenly change their behavior, i.e., those that get trapped or are able to escape from a trapped state. Indeed, we found examples for such dynamic trapping or escape events (see Supporting Information). In some rare cases, we even observed diffusing particles which transiently bound to the hydrogel and then unbound again after a few seconds as depicted in Figure 3a.

On top of this dynamic switching between a mobile and a trapped state, a closer examination of individual particle trajectories reveals the existence of an even more complex behavior (see Figure 3b and Supporting Information): At the beginning of the observation, the particle depicted in Figure 3b exhibits rapid diffusion. Yet, after ∼10 s the particle motion becomes confined, indicating that it binds to the hydrogel. Moreover, after ∼250 s, the fluctuation amplitude in the colloid displacement is significantly reduced, indicating that it suddenly becomes even more confined. This suggests a switch from a loosely bound into a tightly bound state. However, about 2 min later the fluctuation amplitude of the particle becomes somewhat larger again, suggesting that it switched back into its loosely bound state. This finding shows that it might be necessary to discriminate between three distinct states for a correct description of colloid mobility in Matrigel: a freely diffusing state, a weakly bound state, and a tightly bound state.

Particle Trapping Efficiency Depends on the Ion Concentration and Species. Having shown that the addition of high concentrations of KCl to the hydrogel buffer can restore the mobility of colloids in Matrigel, we next ask if the trapping efficiency of the gel depends on the ion species. To do so, we subsume weakly and tightly bound particles into an "immobile" subgroup and classify freely diffusing particles as "mobile" (see Materials and Methods). First, we tested increasing concentrations of KCl and observed an increasing fraction of mobile particles with increasing ionic strength (Figure 3c). Such a binary behavior, e.g. finding only immobilized and almost freely diffusing particles even at high ionic strength, is surprising: Given the high salt concentration of the buffer, electrostatic interactions between the particles and the hydrogel macromolecules should be efficiently screened throughout the whole sample. Nevertheless, a high percentage of particles remains trapped in the hydrogel matrix, even at salt concentrations as high as 1.5 M KCl. The same trend is observed when KCl is substituted by NaCl: only a fraction of particles can be remobilized, even at very high ionic strength. One possible explanation for this observation could be a strong variation in the particle properties. However, as the polystyrene particles have a very small polydispersity index of ∼0.15 and since their surface chemistry has not been altered after purchase, the particle properties should be rather homogeneous which renders this explanation unlikely. Another possible scenario might be that even at salt concentrations as high as 1.5 M the particle charge is not sufficiently screened yet. To test this hypothesis, we substitute the monovalent ions Na^+ and K^+ by the divalent ions Mg^{2+} and Ca^{2+} as their screening efficiency is expected to be higher.

When testing increasing concentrations of those divalent cations, we observed a similar general trend as before: At low concentrations of 0.1 M, both Mg^{2+} and Ca^{2+} have a similar effect in remobilizing the colloids: only about 2% of mobile particles are observed. However, at a concentration of 0.5 M of $MgCl_2$ or $CaCl_2$, respectively, the mobility of all particles is fully restored. This is in contrast to monovalent ions where it was not possible to restore the mobility of all colloids even with salt concentrations as high as 1.5 M. So far, $MgCl_2$ and $CaCl_2$ had a comparable influence on the particle trapping efficiency. At intermediate concentrations of 0.2 M, however, the experimental outcome is different: Whereas for $MgCl_2$ about 60% of the particles are still trapped, all particles are remobilized when $CaCl_2$ is used. This demonstrates that not only differences in the ion valency but also differences in the ion species can affect the trapping efficiency of colloids in Matrigel. For a more detailed investigation of those ion-specific effects, it would be helpful if one were able to test another set of cations or, instead, substitute chlorine by another anion. However, this is unfeasible for Matrigel which is a complex biological system that is adapted to a physiological environment and does not endure extreme buffer conditions. For instance, a change in buffer pH below pH 6 or above pH 8 results in a collapse of the gel (data not shown), and gel formation is also inhibited for high concentrations of e.g. fluorine or iodine ions. Still, ordering the four testable cations according to their efficiency in restoring the colloid's mobility yields a sequence that resembles the Hofmeister series. This suggests that ion-specific effects that might be related to the Hofmeister series regulate the trapping of colloids in Matrigel.

However, a generic order of ions according to their Hofmeister effect does not exist. Instead, the specific order of the Hofmeister series depends on the detailed physicochemical parameters of the interacting surfaces. For instance, it has been demonstrated that an inverted order (the so-called indirect Hofmeister series) is obtained when the surface polarity is altered or when the surface charge is inverted from negative to positive.[17−19] Experimentally, the latter can be achieved in our system by altering the charge of the colloids, e.g., by using polystyrene particles terminated with NH_2 groups instead of COOH. When the mobility of amine-terminated polystyrene particles is analyzed in Matrigel, the general trend stays the same as observed for the carboxyl-terminated particles: increasing salt concentrations result in an increasing fraction of mobile particles. However, the mobility of amine-terminated particles is already fully restored at a concentration of 0.2 M $MgCl_2$ or $CaCl_2$. This is in contrast to the colloids with COOH groups where 0.5 M of divalent ions was required to restore the

mobility of all particles. This agrees with the observation that the absolute value of the ζ-potential is lower for the amine particles compared to their carboxylated counterparts. To detect putative differences in the remobilizing efficiency of $MgCl_2$ and $CaCl_2$, we therefore have to compare those ions at lower concentrations. At 0.1 M $MgCl_2$, about 50% of the colloids are mobile. In contrast, when Mg^{2+} is substituted by Ca^{2+}, only about 30% mobile particles are observable. Indeed, at this concentration, the remobilizing efficiency of both divalent ions differs significantly. Yet, this time, Ca^{2+} is more efficient than Mg^{2+}, indicating that the order of those ions is inverted for particles with NH_2 groups.

Discussion. In this study, we have analyzed the diffusive mobility of polystyrene particles in Matrigel by systematically varying the species and concentration of ions added to the hydrogel buffer. In our experiments, we observed that particles with charged surfaces are efficiently trapped at low salt concentrations and that the particle mobility can be restored at high ionic strength. This finding agrees with recent studies which have identified multiple parameters that govern the mobility of colloidal particles in such biological gels. Besides the ratio of particle size with respect to the hydrogel mesh size, mainly the surface properties of the colloids have been observed to determine their diffusion behavior as they give rise to adhesive interactions with the hydrogel matrix.[7,20−22] As a consequence, PEGylation has been put forward as a key strategy to avoid those adhesive interactions—provided that the PEG chains used for chemical passivation of the colloidal surfaces are short enough so that they do not decrease the particle mobility by inducing molecular friction.[23−25] In the absence of such a chemical surface passivation, efficient and rigorous trapping of colloids can occur. Interestingly, the detailed charge distribution and not only the net surface properties of particles or molecules might dictate their diffusion properties in biological gels. First experimental support for this idea was demonstrated recently when the transport of peptides into mucin gels was studied.[26] There, peptide sequences with the same net charge but differences in the local charge distribution showed significant differences in their transport properties. Conversely, local differences in the charge distribution of the hydrogel constituents might also turn out to be the key factor that regulates the trapping of particles and molecules—rather than the net charge of the gel.

For such trapped particles, we here have demonstrated that at sufficiently high ionic strength a particle can dynamically switch between the freely diffusing and the trapped state. From our analysis of long-time particle trajectories we have detected at least two different subsets of trapped states: a weakly and a strongly bound state. At this point it is crucial to recall that at the beginning of our data analysis we have classified all particles with MSD curves exhibiting α-values between 0 and 0.7 as "trapped" (Figure 2). Now, we are able to further refine this classification into loosely bound particles for $0.1 < \alpha < 0.7$ and tightly bound particles for $\alpha < 0.1$. One possible explanation for the occurrence of both loosely and strongly bound particles is schematically depicted in Figure 4.

We suggest that loosely bound particles only engage in binding interactions with single hydrogel macromolecules (or with a few of them), whereas strongly bound particles might interact with multiple hydrogel macromolecules at the same time. The length scale of this process is on the order of the particle size, which underscores our notion that the trapping process should be governed by the local charge density of the hydrogel macromolecules rather than by the net charge of the gel. As a consequence, the thermal fluctuations of particles in the two distinct "trapped" states will represent differences in the microarchitecture of the gel and thus different micromechanical environments. With this picture in mind, the thermal motion of the loosely bound particles can be used to perform a microrheological estimate of the local plateau modulus G_0 of Matrigel.[27] Using the relation $G_0 \sim k_B T/\langle x_p^2\rangle R$, where $\langle x_p^2\rangle$ denotes the plateau value of the MSD and R is the particle radius, we obtain approximately $G_{0,\mathrm{micro}} = 0.1$ Pa, which is a factor of 50 smaller than the macroscopic plateau modulus of the hydrogel, $G_{0,\mathrm{macro}} = 5$ Pa (see Supporting Information for experimental details). Yet, it is important to realize that such a macromechanical parameter cannot directly be used to estimate the mesh size of the hydrogel without additional information on the gel microarchitecture and the mechanical properties of the gel constituents (see Supporting Information for details). On the other hand, the extremely small fluctuation amplitudes of the tightly bound particles demonstrate that there are regions within the hydrogel matrix that are significantly stiffer than 0.1 Pa, indicating that the micromechanical properties of Matrigel are strongly heterogeneous. Such heterogeneity is also observed in other biological gels.[28,29] However, it is very difficult to show if the microarchitecture of the hydrogel is heterogeneous per se or modified by the presence of the particles—which is a common problem in microrheology.[14]

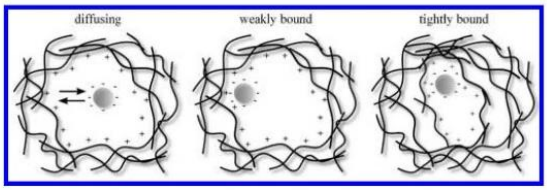

Figure 4. A possible scenario explaining the occurrence of mobile, weakly bound, and strongly bound particles is schematically illustrated (the charge on the hydrogel strands is chosen to be positive for illustrative purposes and is not meant to reflect the overall situation in Matrigel). A loosely bound particle could e.g. be connected to a single or to very few hydrogel strands, whereas a tightly bound particle might bind to several hydrogel macromolecules at the same time. As unbinding and rebinding events occur, a given particle can switch between two neighboring states. In principle, a combination of both long-ranged and short-ranged forces could be responsible for the observed particle trapping process.

By systematically varying the salt species and salt concentration, we have demonstrated for the first time the relevance of ion-specific effects for the diffusive mobility of submicrometer-sized particles in Matrigel. Our observations are consistent with ion-specific effects that have already been reported for many other, yet much simpler systems.[30,31] We here describe that increasing salt concentrations lead to an increasing fraction of mobile particles. One possible explanation for this observation could be that a swelling of the gel, induced by the added ions, causes an increase in the mesh size. This would decrease the probability of particle binding to the hydrogel and would lead to a higher fraction of mobile particles. However, divalent ions are known to cause deswelling of hydrogels and, accordingly, a decrease in the mesh size.[32−34] This agrees with macrorheological results as we observe an increase in the plateau modulus of Matrigel when divalent ions are added (see Supporting Information) which supports the idea that the mesh size of the hydrogel decreases in the

presence of those ions. Yet, in this case, the particle mobility should be decreased rather than increased by divalent ions, which is inconsistent with our findings.

Ion-specific effects are usually obtained at ion concentrations between 0.1 and 2 M since, at those high salt concentrations, the otherwise dominant generic electrostatic interactions are efficiently screened[35]—which agrees with the observations reported here. Yet, the detailed origin of ion-specific effects is still not fully understood because diverse interactions, such as ion−particle, ion−hydrogel, and particle−hydrogel interactions, have to be considered.[35] These interactions are governed by a broad range of parameters, such as charge density, surface tension, structure, and the chemical composition of macromolecules.[35]

One simple model to explain ion-specific effects is the Collins' concept of matching water affinities.[36] Here the concept of "like seeks like" is applied. Yet, whereas this simple model can describe the interactions between individual ions, it already fails to rationalize the much more complex interactions between ions and COOH surface groups of colloids. In fact, a stronger interaction of Na^+ with COOH was described than for K^+ with COOH.[37] This finding suggests a higher efficiency of Na^+ compared with K^+ in remobilizing carboxyl-terminated colloids in Matrigel. Yet, we cannot confirm this prediction from our observations as there are no significant differences for Na^+ and K^+ in our experiments. This might, at least in part, be due to the high degree of complexity of Matrigel that arises from the combination of more than three different biological macromolecules—each with a heterogeneous chemical microstructure.

■ CONCLUSION

Here, we have described a dynamic switching process between freely diffusing and trapped particles in a biological hydrogel environment. We have analyzed this diffusion processes for individual particles on short time scales, i.e., in the range of milliseconds to seconds. Yet, in analogy to the binding and release process of sticky particles to a surface,[38] we expect that the ensemble average of the MSD should become similar to free diffusion when the observation time is increased a lot so that it becomes large compared to the average time a particle spends in the trapped state. Such a behavior was predicted on the basis of Monte Carlo simulation studies, where the impact of inert and sticky obstacles on the time dependence of the MSD of tracer particles was evaluated.[39] There, it has been shown that the subdiffusive character of the MSD is only observable on short time scales and that the ensemble-averaged MSD curve converges toward a linear time dependence on very long observation times. However, such long-time data are very difficult to obtain with single particle tracking. Importantly, the crossover time separating an apparently subdiffusive regime from the well-understood Brownian motion regime at long times is set by the binding energy.[39] For diffusion of colloidal particles in Matrigel, our results demonstrate that this binding energy will depend on both the type and concentration of buffer ions. Thus, this biological hydrogel represents a system in which nature has established a highly complex mechanism to tune the diffusion behavior of particles. By varying the ionic content of Matrigel, the permeability properties of this biological hydrogel can be sensitively tuned. As a consequence, our finding might open new avenues for this biogel to be used as a tunable microfilter in cell culture settings or in nanoseparation applications.

Such a selective regulation of diffusive processes has already been described in several other biological hydrogels, and this selective filtering has previously been demonstrated to depend on a range of parameters.[2] Besides the ratio of particle size and hydrogel mesh size, mainly adhesive interactions between diffusing objects and the hydrogel constituents were suggested to entail a retardation of diffusive processes.[40−43] Here, we have shown the importance of ion-specific effects as an important parameter regulating those adhesive interactions and thus the permeability of biological hydrogels. Because of the highly complex composition of biological hydrogels, a theoretical framework which fully explains our findings and the underlying molecular mechanisms is still lacking. Theoretical studies on hindered diffusion within porous structures incorporating a surface charge distribution are a first step toward a systematic examination of ion-specific effects on the permeability of other biological hydrogel systems.[44] This might help to develop a more detailed understanding of those mechanisms and could also shed new light on the biological function of those hydrogels. For instance, in the presynaptic terminal of neuronal axons, the release of synaptic vesicles is induced by calcium ions but not by sodium or potassium ions, although the latter are abundant in the neuron.[45] Similarly, the Matrigel hydrogel system studied here constitutes a biological example where ion-specific effects allow for "switching on" diffusive processes on demand.

■ ASSOCIATED CONTENT

Supporting Information

MSD curves at low-salt conditions, simulation data, examples for particle binding/unbinding events and tightly/weakly bound particles, viscoelastic frequency spectrum of Matrigel. This material is available free of charge via the Internet at http://pubs.acs.org.

■ AUTHOR INFORMATION

Corresponding Author

*E-mail: oliver.lieleg@TUM.de (O.L.).

Present Address

∥R.B.: Medizinische Physik, Department für Medizinische Physik and Akustik, Universität Oldenburg, Carl-von-Ossietzky Straße 9-11, 26111 Oldenburg, Germany.

Author Contributions

⊥F.A. and R.B. contributed equally.

Notes

The authors declare no competing financial interest.

■ ACKNOWLEDGMENTS

This work was supported by the Deutsche Forschungsgemeinschaft through project B7 "Nanoagents in 3-dimensional biopolymer hydrogels" in the framework of SFB 1032. Regina Baumgärtel acknowledges a short-term scholarship by the German Academic Exchange Services (DAAD). The authors thank Katharina Ribbeck at MIT in whose lab this project was initiated. Steve Wasserman provided the high-speed image acquisition software used in this study which is gratefully acknowledged. Helpful discussions with Andreas Bausch, Thorsten Hugel, and Nadine Schwierz are appreciated.

■ REFERENCES

(1) Einstein, A. Eine neue Bestimmung der Moleküldimensionen. *Ann. Phys. (Berlin, Ger.)* **1906**, *324* (2), 289−306.

(2) Lieleg, O.; Ribbeck, K. Biological Hydrogels As Selective Diffusion Barriers. *Trends Cell Biol.* **2011**, *21* (9), 543−551.
(3) Kleinman, H. K.; Mcgarvey, M. L.; Hassell, J. R.; Star, V. L.; Cannon, F. B.; Laurie, G. W.; Martin, G. R. Basement-Membrane Complexes with Biological-Activity. *Biochemistry* **1986**, *25* (2), 312−318.
(4) Kleinman, H. K.; Mcgarvey, M. L.; Liotta, L. A.; Robey, P. G.; Tryggvason, K.; Martin, G. R. Isolation and Characterization of Type-IV Procollagen, Laminin, and Heparan-Sulfate Proteoglycan from the EHS Sarcoma. *Biochemistry* **1982**, *21* (24), 6188−6193.
(5) Kleinman, H. K.; Martin, G. R. Matrigel: Basement Membrane Matrix with Biological Activity. *Semin. Cancer Biol.* **2005**, *15* (5), 378−386.
(6) Kim, B.; Han, G.; Toley, B. J.; Kim, C. K.; Rotello, V. M.; Forbes, N. S. Tuning Payload Delivery in Tumour Cylindroids Using Gold Nanoparticles. *Nat. Nanotechnol.* **2010**, *5* (6), 465−472.
(7) Lieleg, O.; Baumgärtel, R. M.; Bausch, A. R. Selective Filtering of Particles by the Extracellular Matrix: An Electrostatic Bandpass. *Biophys. J.* **2009**, *97* (6), 1569−1577.
(8) Fridman, R.; Kibbey, M. C.; Royce, L. S.; Zain, M.; Sweeney, T. M.; Jicha, D. L.; Yannelli, J. R.; Martin, G. R.; Kleinman, H. K. Enhanced Tumor-Growth of Both Primary and Established Human and Murine Tumor-Cells in Athymic Mice after Coinjection with Matrigel. *J. Natl. Cancer Inst.* **1991**, *83* (11), 769−774.
(9) Albini, A.; Melchiori, A.; Garofalo, A.; Noonan, D. M.; Basolo, F.; Taraboletti, G.; Chader, G. J.; Giavazzi, R. Matrigel Promotes Retinoblastoma Cell-Growth In Vitro and In Vivo. *Int. J. Cancer* **1992**, *52* (2), 234−240.
(10) Zimrin, A. B.; Villeponteau, B.; Maciag, T. Models of in-Vitro Angiogenesis - Endothelial-Cell Differentiation on Fibrin But Not Matrigel Is Transcriptionally Dependent. *Biochem. Biophys. Res. Commun.* **1995**, *213* (2), 630−638.
(11) Peyton, S. R.; Ghajar, C. M.; Khatiwala, C. B.; Putnam, A. J. The Emergence of ECM Mechanics and Cytoskeletal Tension As Important Regulators of Cell Function. *Cell Biochem. Biophys.* **2007**, *47* (2), 300−320.
(12) Marasanapalle, V.; Li, X. L.; Polin, L.; Jasti, B. R. Novel in Vitro Model Barriers for Evaluation of the Permeability of Antitumor Compounds, Thioxanthones. *Invest. New Drugs* **2006**, *24* (2), 111−116.
(13) Zaman, M. H.; Trapani, L. M.; Siemeski, A.; MacKellar, D.; Gong, H. Y.; Kamm, R. D.; Wells, A.; Lauffenburger, D. A.; Matsudaira, P. Migration of Tumor Cells in 3D Matrices Is Governed by Matrix Stiffness along with Cell-Matrix Adhesion and Proteolysis. *Proc. Natl. Acad. Sci. U. S. A.* **2006**, *103* (29), 10889−10894.
(14) Valentine, M. T.; Perlman, Z. E.; Gardel, M. L.; Shin, J. H.; Matsudaira, P.; Mitchison, T. J.; Weitz, D. A. Colloid Surface Chemistry Critically Affects Multiple Particle Tracking Measurements of Biomaterials. *Biophys. J.* **2004**, *86* (6), 4004−4014.
(15) Schilling, J.; Sackmann, E.; Bausch, A. R. Digital Imaging Processing for Biophysical Applications. *Rev. Sci. Instrum.* **2004**, *75* (9), 2822−2827.
(16) Cheezum, M. K.; Walker, W. F.; Guilford, W. H. Quantitative Comparison of Algorithms for Tracking Single Fluorescent Particles. *Biophys. J.* **2001**, *81* (4), 2378−2388.
(17) Lopez-Leon, T.; Santander-Ortega, M. J.; Ortega-Vinuesa, J. L.; Bastos-Gonzalez, D. Hofmeister Effects in Colloidal Systems: Influence of the Surface Nature. *J. Phys. Chem. C* **2008**, *112* (41), 16060−16069.
(18) Schwierz, N.; Horinek, D.; Netz, R. R. Anionic and Cationic Hofmeister Effects on Hydrophobic and Hydrophilic Surfaces. *Langmuir* **2013**, *29* (8), 2602−2614.
(19) Schwierz, N.; Horinek, D.; Netz, R. R. Reversed Anionic Hofmeister Series: The Interplay of Surface Charge and Surface Polarity. *Langmuir* **2010**, *26* (10), 7370−7379.
(20) Lieleg, O.; Vladescu, I.; Ribbeck, K. Characterization of Particle Translocation through Mucin Hydrogels. *Biophys. J.* **2010**, *98* (9), 1782−1789.
(21) Xu, Q. G.; Boylan, N. J.; Suk, J. S.; Wang, Y. Y.; Nance, E. A.; Yang, J. C.; McDonnell, P. J.; Cone, R. A.; Duh, E. J.; Hanes, J. Nanoparticle Diffusion in and Microrheology of the Bovine Vitreous Ex Vivo. *J. Controlled Release* **2013**, *167* (1), 76−84.
(22) Cu, Y.; Saltzman, W. M. Mathematical Modeling of Molecular Diffusion through Mucus. *Adv. Drug Delivery Rev.* **2009**, *61* (2), 101−114.
(23) Wang, Y. Y.; Lai, S. K.; So, C.; Schneider, C.; Cone, R.; Hanes, J., Mucoadhesive Nanoparticles May Disrupt the Protective Human Mucus Barrier by Altering Its Microstructure. *PLoS One* **2011**, *6*, (6).
(24) Doane, T. L.; Cheng, Y.; Babar, A.; Hill, R. J.; Burda, C. Electrophoretic Mobilities of PEGylated Gold NPs. *J. Am. Chem. Soc.* **2010**, *132* (44), 15624−15631.
(25) Hill, R. J.; Li, F. Hydrodynamic Drag Coefficient for Soft Core-Shell Nanoparticles in Hydrogels. *Chem. Eng. Sci.* **2013**, *89*, 1−9.
(26) Li, L. D.; Crouzier, T.; Sarkar, A.; Dunphy, L.; Han, J.; Ribbeck, K. Spatial Configuration and Composition of Charge Modulates Transport into a Mucin Hydrogel Barrier. *Biophys. J.* **2013**, *105* (6), 1357−1365.
(27) Mason, T. G.; Weitz, D. A. Optical Measurements of Frequency-Dependent Linear Viscoelastic Moduli of Complex Fluids. *Phys. Rev. Lett.* **1995**, *74* (7), 1250−1253.
(28) Luan, Y.; Lieleg, O.; Wagner, B.; Bausch, A. R. Micro- and Macrorheological Properties of Isotropically Cross-Linked Actin Networks. *Biophys. J.* **2008**, *94* (2), 688−693.
(29) Lai, S. K.; Wang, Y. Y.; Hida, K.; Cone, R.; Hanes, J. Nanoparticles Reveal That Human Cervicovaginal Mucus Is Riddled with Pores Larger Than Viruses. *Proc. Natl. Acad. Sci. U. S. A.* **2010**, *107* (2), 598−603.
(30) Hofmeister, F. Zur Lehre von der Wirkung der Salze. *Arch. Exp. Pathol. Pharmakol.* **1888**, *25* (1), 1−30.
(31) Lo Nostro, P.; Ninham, B. W. Hofmeister Phenomena: An Update on Ion Specificity in Biology. *Chem. Rev.* **2012**, *112* (4), 2286−2322.
(32) Muta, H.; Miwa, M.; Satoh, M. Ion-Specific Swelling of Hydrophilic Polymer Gels. *Polymer* **2001**, *42* (14), 6313−6316.
(33) Tang, Q. W.; Wu, J. H.; Lin, J. M.; Li, Q. H.; Fan, S. J. Two-Step Synthesis of Polyacrylamide/Polyacrylate Interpenetrating Network Hydrogels and Its Swelling/Deswelling Properties. *J. Mater. Sci.* **2008**, *43* (17), 5884−5890.
(34) Choi, H. J.; Kunioka, M. Preparation Conditions and Swelling Equilibria of Hydrogel Prepared by Gamma-Irradiation from Microbial Poly(Gamma-Glutamic Acid). *Radiat. Phys. Chem.* **1995**, *46* (2), 175−179.
(35) Kunz, W. Specific Ion Effects in Colloidal and Biological Systems. *Curr. Opin. Colloid Interface Sci.* **2010**, *15* (1−2), 34−39.
(36) Collins, K. D. Ions from the Hofmeister Series and Osmolytes: Effects on Proteins in Solution and in the Crystallization Process. *Methods* **2004**, *34* (3), 300−311.
(37) Vlachy, N.; Jagoda-Cwiklik, B.; Vacha, R.; Touraud, D.; Jungwirth, P.; Kunz, W. Hofmeister Series and Specific Interactions of Charged Headgroups with Aqueous Ions. *Adv. Colloid Interface Sci.* **2009**, *146* (1−2), 42−47.
(38) Xu, Q.; Feng, L.; Sha, R.; Seeman, N. C.; Chaikin, P. M. Subdiffusion of a Sticky Particle on a Surface. *Phys. Rev. Lett.* **2011**, *106*, 22.
(39) Saxton, M. J. Anomalous Diffusion Due to Binding: A Monte Carlo Study. *Biophys. J.* **1996**, *70* (3), 1250−1262.
(40) Lai, S. K.; Wang, Y. Y.; Hanes, J. Mucus-Penetrating Nanoparticles for Drug and Gene Delivery to Mucosal Tissues. *Adv. Drug Delivery Rev.* **2009**, *61* (2), 158−71.
(41) Ribbeck, K.; Görlich, D. The Permeability Barrier of Nuclear Pore Complexes Appears to Operate via Hydrophobic Exclusion. *EMBO J.* **2002**, *21* (11), 2664−2671.
(42) Rusu, L.; Lumma, D.; Rädler, J. O. Charge and Size Dependence of Liposome Diffusion in Semidilute Biopolymer Solutions. *Macromol. Biosci.* **2010**, *10* (12), 1465−1472.
(43) Boehm, H.; Mundinger, T. A.; Boehm, C. H. J.; Hagel, V.; Rauch, U.; Spatz, J. P.; Curtis, J. E. Mapping the Mechanics and

Macromolecular Organization of Hyaluronan-Rich Cell Coats. *Soft Matter* **2009**, *5* (21), 4331−4337.
(44) Phillips, R. J. The Effect of Surface Charge Distribution on Hindered Diffusion in Pores. *J. Colloid Interface Sci.* **2009**, *338* (1), 250−260.
(45) Sudhof, T. C. The Synaptic Vesicle Cycle. *Annu. Rev. Neurosci.* **2004**, *27*, 509−547.

A.4 Supporting Information: Ion-Specific Effects Modulate the Diffusive Mobility of Colloids in an Extracellular Matrix Gel

Table S1. The main constituents of Matrigel and their corresponding pI values calculated from expasy.

Protein	pI
Laminin subunit α	6.26
Laminin subunit β	4.82
Laminin subunit γ	5.08
Heparan sulfate proteoglycan core protein	5.88
Collagen IV	8.85
Nidogen	5.22

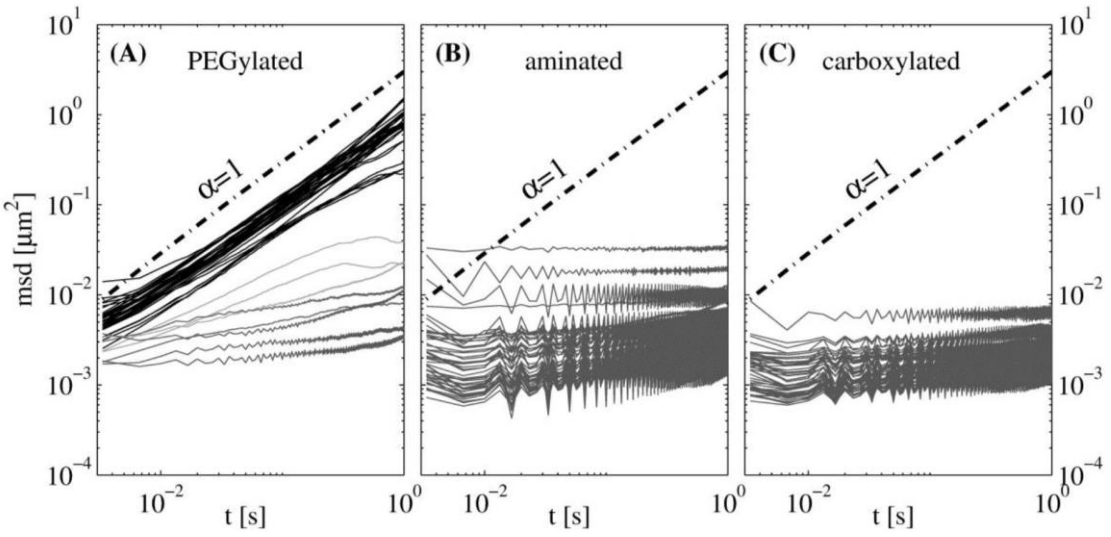

Figure S1. Diffusion behavior of 1 μm polystyrene particles in Matrigel diluted with HEPES buffer (pH 7.5) at an ionic strength of 100 mM KCl. From the particle trajectories, mean square displacement curves are calculated for **(A)** PEGylated, **(B)** amine-terminated and **(C)** carboxyl-terminated polystyrene particles.

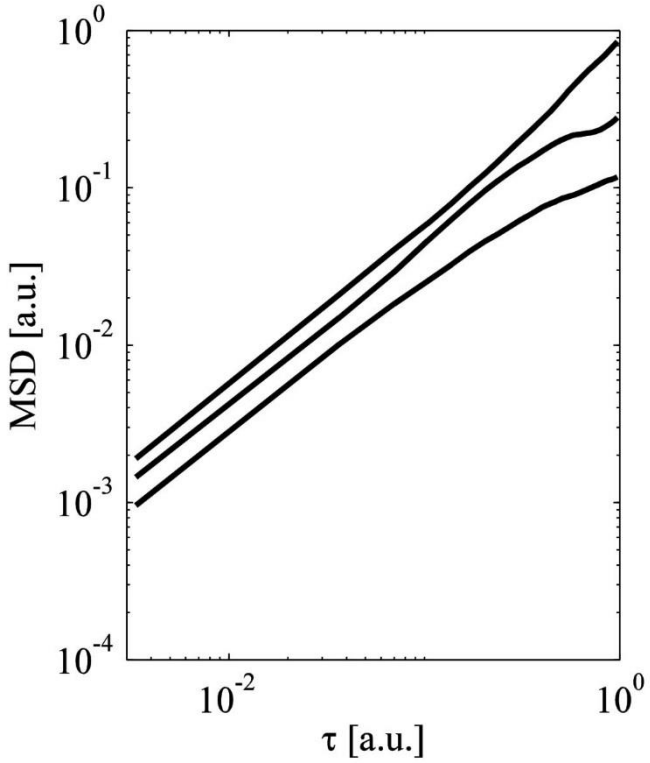

Figure S2. Three exemplary MSD curves with an exponent α ranging from 0.7 to 1.2 obtained from simulations of free diffusion (curves are shifted for clarity). The exponent α is defined by $\langle x^2 \rangle \propto \tau^{\alpha}$ as described in the manuscript. The amount of data points matches the number of data points collected in our single particle tracking experiments.

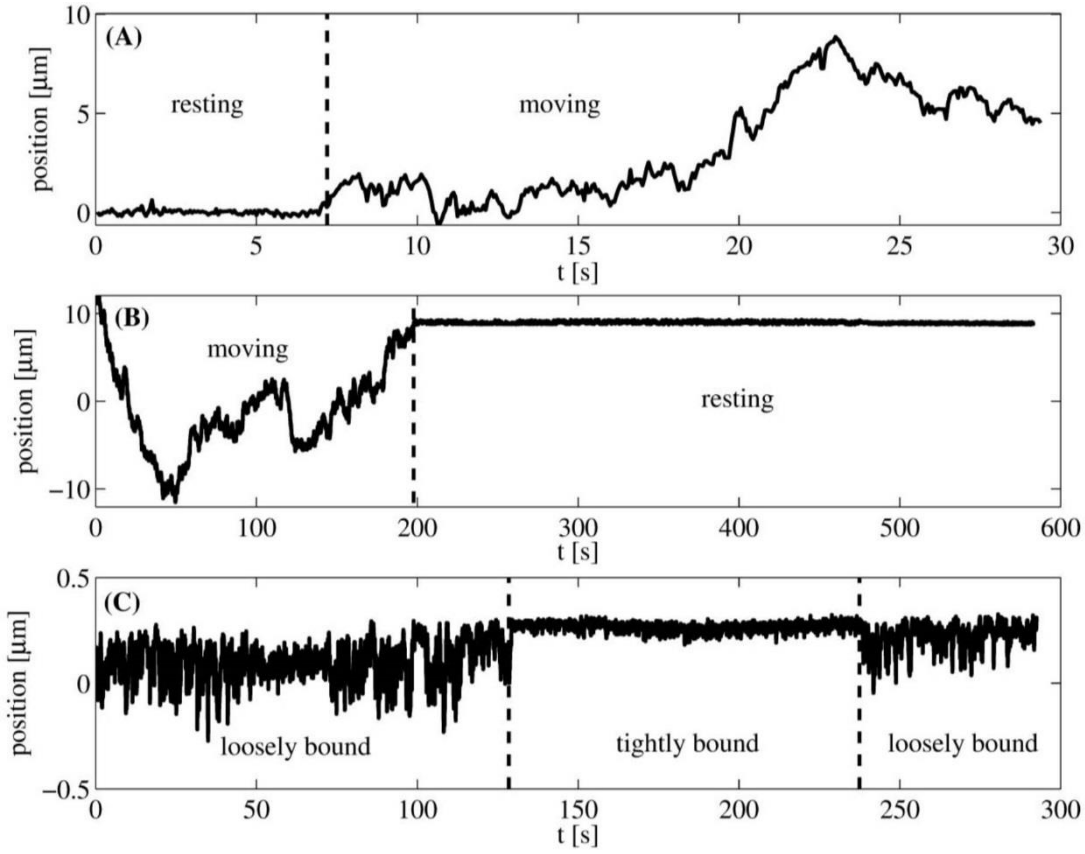

Figure S3. Further examples for trapping/release events observed for 300 nm-sized particles in Matrigel. **(A)** shows the x-coordinate of a particle trajectory obtained for a 300 nm carboxyl-terminated polystyrene particle in Matrigel at a salt concentration of 0.5 M KCl. At first, the particle is bound to the hydrogel but starts diffusing after ~7 s. **(B)** The particle diffuses for the first 3 min of the observation but then it becomes trapped as it binds to the hydrogel. **(C)** Two types of binding can be observed: at the beginning and at the end of the observation, the particle is loosely bound as reflected the high fluctuation amplitude of the particle displacement. In between those loosely bound states, the particle is tightly bound as indicated by the smaller fluctuation amplitude. **(B)** and **(C)** were both obtained for 300 nm carboxyl-terminated polystyrene particles in Matrigel supplemented with 1.5 M KCl.

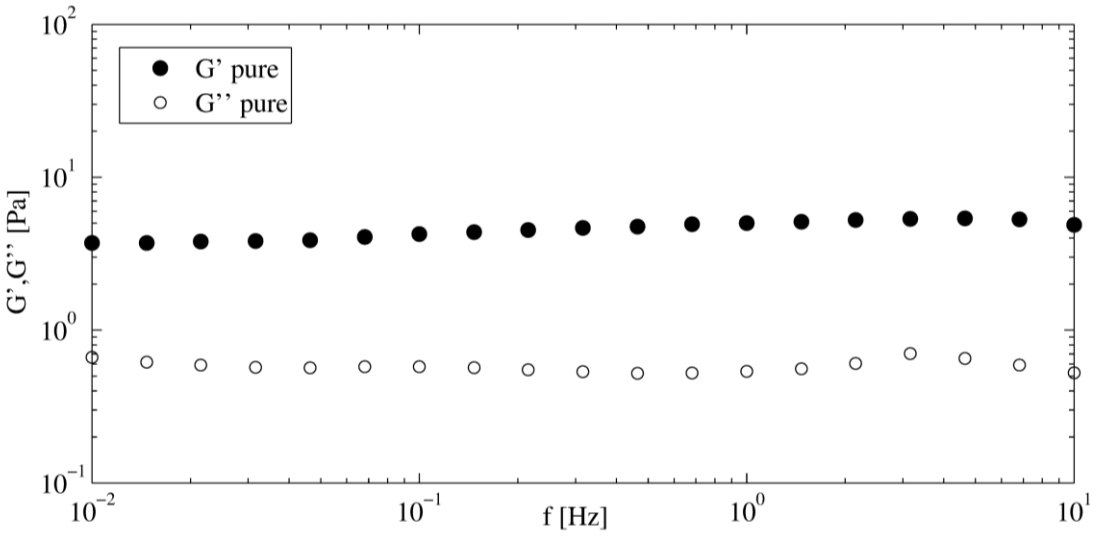

Figure S4. Viscoelastic frequency spectrum obtained for Matrigel which has been diluted 1:1 with MEM-α cell media. The storage modulus G' (filled circles) as well as the loss modulus G'' (open circles) are nearly constant over three decades of frequency. This allows us to define a plateau modulus $G_0 = G' \sim 5$ Pa. It is tempting to calculate a mesh size from this plateau value, however, the plateau modulus of a biopolymer network depends on a range of parameters: First, the bending stiffness of the biopolymer is a crucial parameter: scaling relations for the plateau modulus are markedly different for networks of flexible, semi-flexible or stiff polymers. Second, it is important to distinguish between an entangled solution and a cross-linked polymer network, respectively. For a cross-linked polymer network, as it is the case for Matrigel, the concentration of cross-linking points mainly sets the value of the plateau modulus. Tharmann et al (PRL 98, 088103 (2007)) have shown that the plateau modulus of an actin network can be increased by two orders of magnitude while the mesh size is kept constant. The weak frequency

dependence of the loss modulus G'' is an indication for suppressed macromolecule reptation which is probably due to cross-linking interactions of laminin with other laminin macromolecules. The measurement was performed on a stress-controlled macrorheometer (MCR 102, Anton Paar, Graz, Austria) with a 25 mm plate-plate geometry at a plate separation of 175 µm after 30 min gelation time at 37°C.

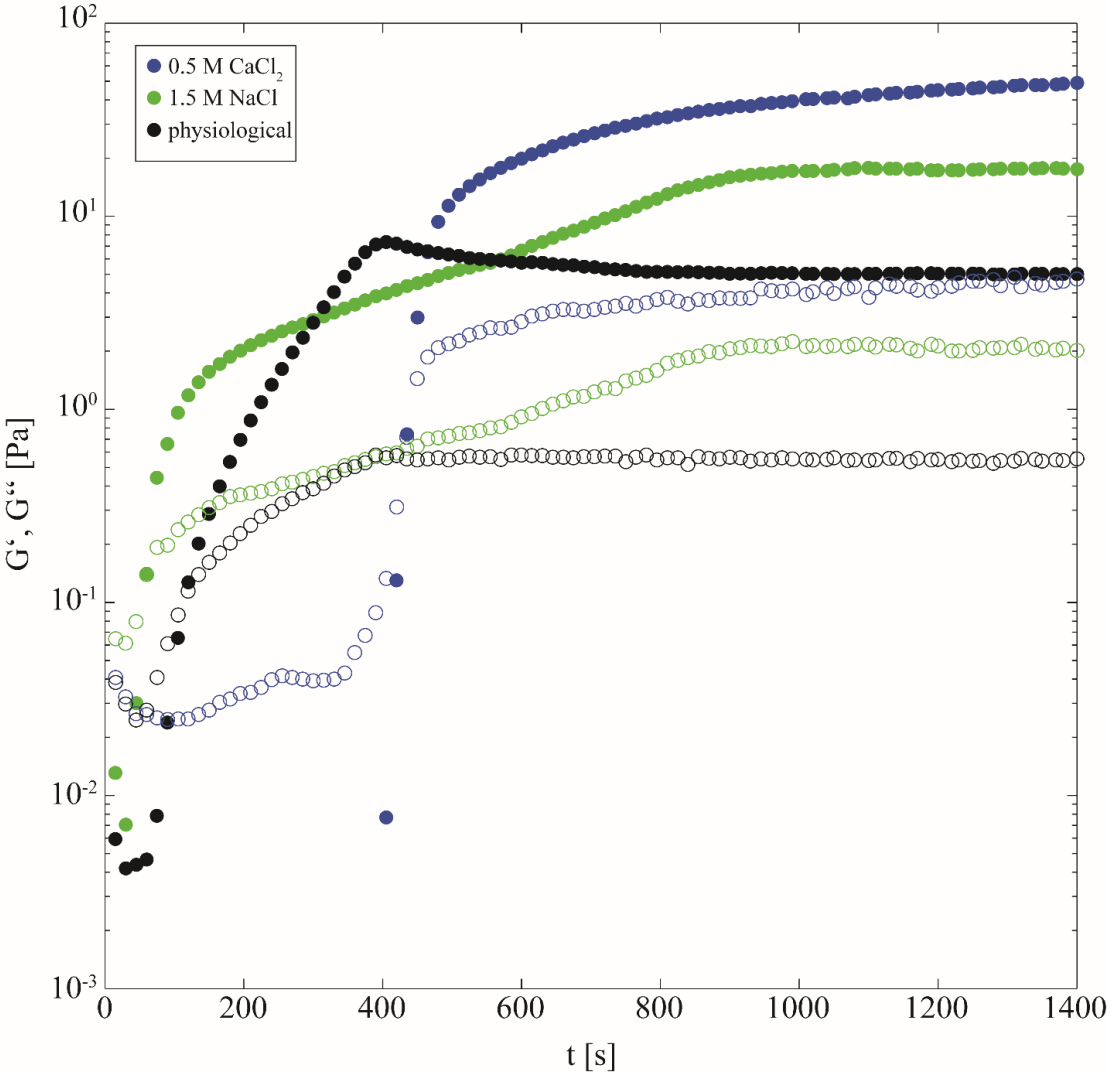

Figure S5. Gelation curve for Matrigel which has been diluted 1:1 with MEM-α cell media without further addition of ions (black) and with either additional 0.5 M $CaCl_2$ (blue) or 1.5 M NaCl (green). The storage modulus G' (filled circles) as well as the loss modulus G'' (open circles) approach a plateau for all conditions. The final storage

modulus of Matrigel with additional $CaCl_2$ is the highest of the three conditions tested. This finding supports the idea of deswelling of the gel at higher divalent ion concentrations. The measurement was performed on a stress-controlled macrorheometer (MCR 102, Anton Paar, Graz, Austria) with a 25 mm plate-plate geometry at a plate separation of 175 μm and at 37°C.

A.5 A microfluidics approach to study the accumulation of molecules at basal lamina interfaces

Lab on a Chip

PAPER

View Article Online
View Journal

Cite this: DOI: 10.1039/c5lc00561b

A microfluidics approach to study the accumulation of molecules at basal lamina interfaces†

Fabienna Arends,[ab] Sabine Sellner,[c] Philipp Seifert,[d] Ulrich Gerland,[d] Markus Rehberg[c] and Oliver Lieleg*[ab]

For an efficient distribution of drugs and drug carriers through biological barriers such as the vascular system, the size and surface properties of nanoparticles and molecules play a key role. To screen for important parameters which determine the ability of drugs or drug carriers to translocate through complex biological barriers, an *in vitro* assay which correctly predicts the behavior of those objects *in vivo* would be highly desirable. Here, we present a microfluidic setup to probe the diffusive spreading of molecules with different net charges and molecular weights through a basal lamina interface – a biopolymer system which contributes to the barrier function of the vascular system and the skin. From our data, we find a charge dependent accumulation of molecules at the gel interface which is consistent with transient binding of those molecules to the gel constituents. We also observe a similar charge-dependent accumulation of molecules in living mice where the test molecules colocalize with collagen IV, a key component of the basal lamina. Our assay may serve as a platform to perform penetration experiments with even more complex interfaces combining cellular barriers with biopolymer coatings.

Received 19th May 2015,
Accepted 2nd July 2015

DOI: 10.1039/c5lc00561b

www.rsc.org/loc

Introduction

In the human body, complex biological barriers prevent the entrance and distribution of pathogens and other foreign compounds. In addition to their protective function, these barriers also regulate the passage of beneficial molecules such as nutrients, growth factors, proteins, hormones or polysaccharides.[1–3] Examples for such complex biological barriers in the human body include the blood–brain-barrier,[4] the skin,[5] the gastrointestinal tract,[6] the oral cavity[7] and the vascular system.[8] All these examples share a common structure: they consist either of endothelial cells (blood–brain barrier and vascular system) or epithelial cells (oral cavity, skin and gastrointestinal tract) which are coated by a biopolymer matrix. This extracellular matrix (ECM) can be located on the outer side of the cell layer where it constitutes the first line of defense against pathogens as in the oral cavity or the gastrointestinal tract.[9] Alternatively, the ECM may also be located on the basolateral side of the cell layer as it is the case for the basal lamina surrounding blood vessels. Here, the passage of molecules and cells from the blood stream into the adjoining tissue is primarily regulated by the endothelial cells. However, compared to physiologic conditions, the ECM layer becomes more accessible for molecules when the endothelium becomes leaky *e.g.* during inflammation, infection, or in the presence of a tumor.[10,11] Moreover, macromolecules which are bi-directionally exchanged between the blood stream and the interstitium by transcytosis, a mechanism particularly prominent in vascular endothelial cells,[12] need to pass the basal lamina. Similarly, if molecules from the connective tissue are supposed to enter into the blood stream, *e.g.* in the case of subcutaneous injection of heparin or insulin, they need to cross the basal lamina from the basolateral side of the blood vessel wall. In those cases, the basal lamina acts as the primary barrier.

Advanced drug delivery methods make use of the leaky endothelium for the specific targeting of tumors.[13] The efficiency of drug carriers to pass the endothelium and the ECM barrier can depend on several parameters *e.g.* particle size, shape and surface modification. Experiments conducted in bulk systems showed that ECM gels show a high selectivity for nanoparticles based on their charge and hydrophobicity.[14,15] However, the diffusive entry of particles into the ECM

[a] *Institute of Medical Engineering IMETUM, Technische Universität München, Boltzmannstrasse 11, 85748 Garching, Germany. E-mail: oliver.lieleg@TUM.de*
[b] *Department of Mechanical Engineering, Technische Universität München, Boltzmannstrasse 15, 85748 Garching, Germany*
[c] *Walter Brendel Centre of Experimental Medicine, Ludwig-Maximilians-Universität München, Marchioninistr. 15, 81377 Munich, Germany*
[d] *Department of Physics, Technische Universität München, James-Franck-Str.1, 85748 Garching, Germany*
† Electronic supplementary information (ESI) available. See DOI: 10.1039/c5lc00561b

at the interface between the basal lamina and a liquid phase (such as the blood stream) cannot be characterized in those bulk experiments. In addition to the diffusion behavior of nanoparticles also the spreading of encapsulated drug molecules, once they are released, is of great interest.[16] To investigate both, two approaches are possible: *in vivo* experiments in mammals such as mice, rats, rabbits or *in vitro* testing in an appropriate tissue-on-a-chip setup. A pre-screening for important parameters in a robust *in vitro* setup which reliably predicts the diffusive spreading of pharmaceuticals *in vivo* would be highly desirable since it would reduce the need of animal tests.[17]

One promising approach for the realization of such predictive *in vitro* experiments is microfluidics.[18,19] There are already a broad range of experimental settings in which such an approach is used, *e.g.* for the design of a cardiac tissue model,[20] for the investigation of nanoparticle translocation across a permeable endothelium[21] or through a endothelial/epithelial double layer simulating the biological interface in alveoli.[22] Those chips are able to reproduce key results obtained in living tissue in an *in vitro* setting although their setup is strongly simplified: to date, most of those microfluidic penetration assays mainly focus on the barrier function of the cell layer and neglect the influence of the adjacent biopolymer matrix. This is partly due to the fact that it is technically challenging to deposit a soft biopolymer gel on a microfluidics chip in such a way that a stable gel/liquid interface is generated which can be used for a penetration experiment. First realizations of such a molecular penetration experiment with a biopolymer gel have been achieved for mucin gels,[23,24] but are still lacking for other gels such as the basal lamina.

Here, we present a microfluidic assay for the quantification of the diffusive transport of molecules across basal lamina interfaces. As a model system for the basal lamina, we use an extracellular matrix gel which has been purified from the Engelbreth–Holm–Swarm sarcoma of mice. We compare the penetration efficiency of different fluorescent molecules such as dextrans with different molecular weights and net charges as well as customized peptides. In our microfluidics setup, those molecules accumulate at the gel/buffer interface in a charge selective manner in full agreement with model calculations considering transient binding of molecules to the gel components. *In vivo* microinjection experiments conducted in mice show a similar charge selective accumulation of those molecules around blood vessels and a colocalization with collagen IV, a key component of the basal lamina. Thus, our *in vitro* setup successfully predicts the selective transport of molecules across this biological barrier.

Results and discussion

Generating a stable gel/liquid interface on chip

To study the diffusion of different solutes across an extracellular matrix gel we first design a microfluidic chip which allows us to generate a stable gel/liquid interface. As shown in Fig. 1 (for more details see Fig. S1†), this chip has one outlet and two inlets, one for inserting the ECM and one for inserting buffer with fluorescent solutes. Liquid (*i.e.* ice-cold) ECM is filled into the chip through inlet 1. Here, at half the channel length, a "finger-like" structure begins where five pillars divide the main channel into six smaller channels of identical width.

When liquid ECM is filled into inlet 1, it can be carefully pushed into this finger-like structure until, at the end of the pillars, surface tension effects ensure stopping of the liquid (see inset of Fig. 1) and prevent it from entering into the buffer channel which is oriented perpendicular to the pillars. With this setup, a well-defined liquid/air interface is created which is important for the following experiments. As the ECM is inserted into the chip in its liquid state, gelation has to be induced on chip. Such a gelation of ECM is usually achieved by a heating step to 37 °C for 30 minutes (see Methods). However, we here induce gelation at room temperature since all following experiments are conducted at this temperature. During gel formation, it is important to prevent

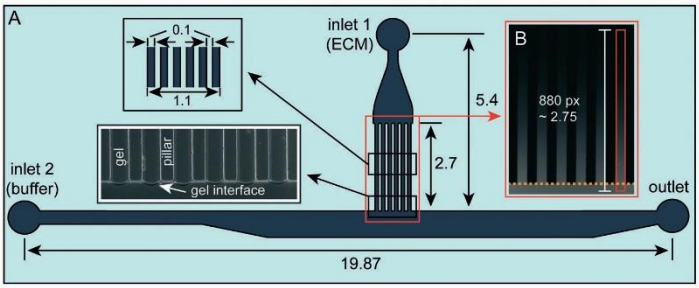

Fig. 1 (A) The microfluidic chip has two inlets: inlet 1 for inserting the ECM and inlet 2 for inserting buffer together with fluorescent molecules of interest. The pillar structure prevents the injected ECM from entering the lower channel due to surface tension. (B) For data analysis, the fluorescence intensity within each channel is measured within a rectangular area with a length of 880 pixels corresponding to 2.75 mm. The lower end of the rectangle is placed 50 pixels into the lower channel so that the bulk intensity in the buffer channel is obtained as well. The orange dotted line denotes the position of the gel/buffer interface. All dimensions in the shown scheme are given in mm.

drying of the ECM – especially at the interface to the compartment which will be filled with fluorescent solutes. A naive approach to avoid such drying of the ECM interface might be to induce gel formation at a water interface. This could be achieved by inserting an aqueous solution, *e.g.* buffer, through inlet 2 directly after loading the chip with the liquid ECM. However, as gelation requires some time, the mechanical strength of the ECM is still weak when the buffer is inserted, and thus the integrity of the ECM compartment is disturbed by buffer influx. Furthermore, when placed at an aqueous interface during gelation, the ECM tends to swell and locally dissolves which in turn results in a diffuse gel interface. A better solution would be to perform gelation at an interface with a hydrophobic fluid that is immiscible with the ECM (and thus does not dissolve the ECM matrix) but still prevents drying. We chose a polydimethylsiloxane oil (PDMS) which fulfills those requirements and is based on the same polymer used for crafting the microfluidic chip. We insert the PDMS oil through inlet 2 into the lower channel and keep it in this compartment until ECM gelation is finished. The oil is then removed from the chip through the outlet and replaced by PBS buffer which is inserted through inlet 2. When the PBS is inserted into the channel, a clear interface between PBS and PDMS oil is visible under the microscope. This feature allowed us to monitor the proper removal of the oil from the channel. With this approach, we are able to generate intact gel/buffer interfaces with which we obtain reproducible penetration profiles with different test molecules.

DEAE-dextrans accumulate at the ECM/buffer interface

We first investigate the correlation between the diffusion efficiency of molecules across an ECM interface and their net charge. We use two variants of FITC-labeled dextrans with a molecular weight of 150 kDa, and those dextrans carry a certain percentage of either diethylaminoethyl (DEAE) or carboxymethyl groups (CM). For the experiments, both sorts of dextrans are dissolved in PBS at a concentration of 10 mg mL^{-1}. Since the pH of the solution is neutral, the DEAE groups are protonated and therefore positively charged, whereas the CM groups are deprotonated and thus negatively charged (see also Table 1). The PBS-dextran solution is inserted into the microfluidic chip through inlet 2 and the results of the experiment 60 min after dextran insertion are shown in Fig. 2: negatively charged CM-dextrans (Fig. 2A) enter the gel without showing noticeable accumulation at the ECM/buffer interface whereas DEAE-dextrans do accumulate (Fig. 2B, white arrows). This difference is somewhat astonishing as previous experiments have demonstrated that both negatively and positively charged objects can be trapped in ECM gels.[14,15,25] However, it is important to recall that ECM gels immobilize positively charged particles more efficiently than negatively charged ones – a behavior which was suggested to arise from the high concentration of negatively charged heparan sulfate in ECM gels.[14] The higher tolerance of the ECM gel for negatively charged nanoparticles could also explain why DEAE-dextrans, which have a net charge of +200e, and CM-dextrans with a net charge of −165e show a different behavior at the gel/buffer interface.

In the bulk volume of the ECM gel, the intensity profiles obtained for the two 150 kDa dextran variants are very similar (Fig. 2C, solid lines and Fig. S2†) and suggest diffusive spreading of those molecules throughout the ECM. Transient binding events as reported for polystyrene particles[15] and growth factors[26] in ECM gels might also occur between the dextran molecules and the ECM components within the bulk volume of the gel, but are likely to take place on the time scale of seconds or below. Thus, on the time scales studied here, these transient binding events of single molecules might give rise to a bulk transport that resembles that of a freely diffusing particle ensemble. Considering that dextrans, which have a hydrodynamic radius of a few nm,[27] are several orders of magnitude smaller than the mesh size of the ECM gel (which is in the μm range[14]), molecule-polymer interactions will be rare both in the bulk volume of the ECM as well as at the ECM/buffer interface. However, we speculate that the high concentration of dextran molecules in the buffer compartment balances the rareness of the binding events giving rise to the observed accumulation of molecules at the gel/liquid interface. To test this hypothesis, we model the diffusive entry of molecules into a gel compartment. For this model, we make the following assumptions: in the buffer compartment the DEAE-dextrans are present at high concentrations and diffuse freely. However, as soon as they reach the buffer/ECM interface they can transiently bind to the ECM network which temporarily interrupts their diffusive penetration of the gel (see Methods and ESI† for details). The results obtained for such calculated penetration profiles are shown in Fig. 3A. Indeed, our simple model returns a penetration profile with a clear accumulation peak at the liquid/gel interface. However, in the bulk volume of the gel phase, the calculated penetration profiles are largely independent from whether or not transient binding events to the gel matrix are considered. This is in agreement with the results from our *in vitro* experiments where we obtained similar penetration profiles for DEAE- and CM-dextrans in the bulk part of the gel.

Table 1 Properties of dextrans and peptides used in the study. The molecular weight was given by the supplier and the charge was calculated assuming that all carboxyl- and amine-groups are charged

Name	Molecular weight [kDa]	Fluorophore type, fluorophore charge [e]	Maximum charge [e]
CM-dextran	150	FITC, −1	−165
DEAE-dextran	150	FITC, −1	+200
CM-dextran	4	FITC, −1	−4
DEAE-dextran	4	FITC, −1	+5
$(KKK)_8$	4	TAMRA, 0	+23
$(QQK)_8$	4	TAMRA, 0	+7
$(EEE)_8$	4	TAMRA, 0	−25
$(QQE)_8$	4	TAMRA, 0	−9

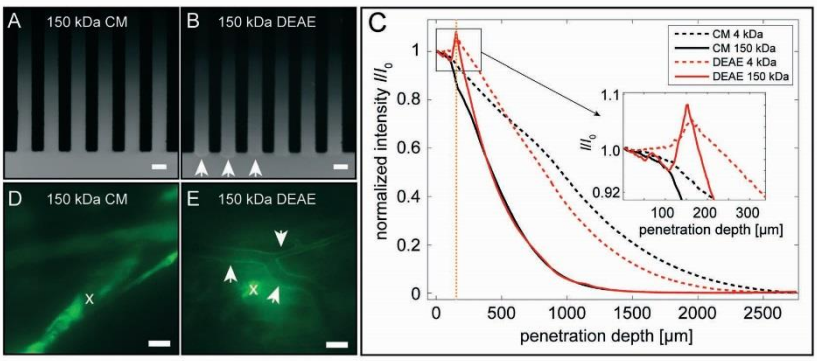

Fig. 2 Fluorescence images of negatively charged CM- (A) and positively charged DEAE-dextrans (B) (MW = 150 kDa) *in vitro* 60 min after their insertion into the chip. The white arrows point at accumulation sites of DEAE-dextran at the buffer/gel interface. The scale bar denotes 100 μm. (C) The corresponding intensity profiles are plotted for positively and negatively charged dextrans of two different molecular weights each. The orange dotted line marks the gel-buffer interface. (D) and (E) show representative images of the spatial distribution of dextrans 60 min after they have been microinjected into the cremaster muscle of a mouse. The CM-dextrans rapidly spread from the injection site (white cross) next to muscle fibers (D) whereas DEAE-dextrans accumulate around blood vessels (white arrows) (E). Scale bar: 50 μm.

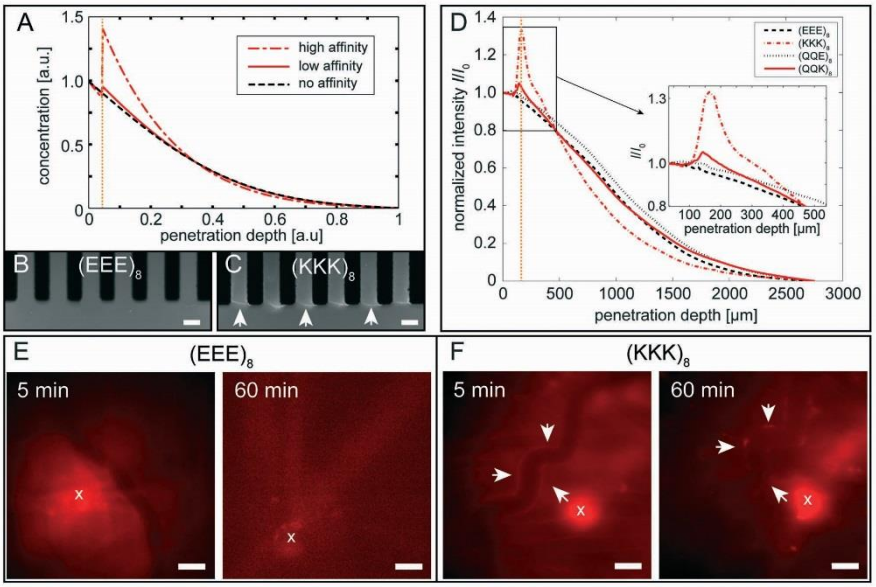

Fig. 3 Molecular penetration profiles are calculated from a model that assumes transient binding of diffusing molecules to the gel components (A). If this binding affinity is set to zero, normal diffusive spreading is obtained. Conversely, the model predicts an accumulation peak at the buffer/gel interface with the height of this peak depending on the strength of the binding affinity. Fluorescence images of negatively $(EEE)_8$ (B) and positively charged $(KKK)_8$ (C) peptides *in vitro* 60 min after buffer insertion are consistent with the model prediction. The white arrows indicate accumulation of peptides at the interface. The scale bar denotes 100 μm. (D) The corresponding intensity profiles are plotted for negatively charged $(EEE)_8$ and $(QQE)_8$ peptides and for positively charged $(KKK)_8$ and $(QQK)_8$ peptides. The orange dotted line marks the gel-buffer interface. (E) and (F) show representative images of $(EEE)_8$ and $(KKK)_8$ peptides microinjected into the mouse cremaster muscle 5 min and 60 min post-injection The negatively charged $(EEE)_8$ peptides rapidly leave the site of injection (white crosses, E) whereas the positively charged $(KKK)_8$ show increased intensity around the blood vessel and at the microinjection site (white crosses, F). Scale bar: 50 μm.

Next, we ask if this charge-selective accumulation also occurs for smaller molecules. To answer this question, we compare the penetration profiles of the 150 kDa DEAE- or CM-dextrans to variants of those molecules with a molecular weight of only 4 kDa. The smaller size of the 4 kDa dextrans will result in a higher diffusion coefficient in water. Thus, within the fixed duration of our experiments, we expect the smaller dextrans to enter more deeply into the channel than the 150 kDa dextrans. Indeed, after a time span of 60 min the 4 kDa dextrans diffuse further into the channel than their 150 kDa counterparts (see the dashed lines in Fig. 2C). Furthermore, we observe that also the positively charged 4 kDa dextrans accumulate at the interface whereas negatively charged dextrans do not. Also, the height of the accumulation peak seems to be similar for both DEAE-dextran variants.

150 kDa DEAE-dextrans accumulate around blood vessels in murine tissue

Of course, in our microfluidic assay many simplifications had to be introduced compared to the *in vivo* situation we aim to mimic. Thus, we next test whether a similar charge-dependent accumulation of dextrans also occurs in living tissue. For this purpose, we perform experiments in living mice and deposit differently sized and charged FITC-labeled dextrans into the mouse cremaster muscle by microinjection. As injection sites, we choose locations in close proximity to blood vessels (*i.e.* postcapillary venules). The venular basement membrane maintains the integrity of the blood vessel and, due to the dense network of matrix proteins, it constitutes a barrier for diffusing macromolecules and emigrating leukocytes.[28]

First, the distribution of injected 150 kDa DEAE-dextrans is investigated. From our *in vitro* experiments, we expect that those dextrans accumulate at the basolateral side of blood vessels where endothelial cells secrete basal lamina components. Indeed, within 5 min after microinjection (Fig. S3†) we observe a pronounced accumulation of 150 kDa DEAE-dextrans around nearby blood vessels, and this accumulation remains stable during the whole observation time of 60 min (Fig. 2E, white arrows). If this accumulation is also charge selective *in vivo*, then the CM-dextrans should exhibit a different behavior. Indeed, in contrast to the DEAE-dextrans, the CM-dextrans do not accumulate around blood vessels within the observation time of 60 min (Fig. 2D). They do, however, seem to concentrate in muscle fibers close to the injection site. We assume that, if the muscle is pierced by the glass capillary during microinjection, a fraction of the 150 kDa CM-dextrans is brought in direct contact with this muscle fiber and remains trapped there. For the 4 kDa dextran variants, this charge selective accumulation behavior is not as pronounced *in vivo* as it was in our *in vitro* setup (Fig. S4†).

The net charge of a molecule sets its accumulation propensity

It was suggested previously that the surface properties of diffusing particles and molecules, *e.g.* their net charge, might play a key role in determining their immobilization efficiency in extracellular matrices.[14,29,30] Polystyrene particles and liposomes trapped in the bulk volume of ECM gels possess a net charge of up to $\pm 10^{10}$e and $\pm 10^{5}$e, respectively. In contrast, the net charge is only +200e for the 150 kDa DEAE-dextrans and −165e for the 150 kDa CM-dextrans and +5e and −4e, respectively, for the 4 kDa dextran variants (Table 1). A direct comparison of nanoparticles and molecules is, of course, difficult. However, also comparing dextrans of different molecular weight is not trivial as those molecules carry different amounts of fluorophores in addition to their DEAE and CM functionalization.

To investigate the influence of the net charge of a molecule on its diffusion across ECM interfaces, we switch from dextran molecules to customized peptides. These synthetic peptides all have the same length, *i.e.* 24 amino acids, and carry one TAMRA label at the N-terminus. We compare the diffusion of four different amino acid sequences, which were designed to differ in terms of their net charge but have similar molecular weights: $(KKK)_8$ (high positive charge), $(QQK)_8$ (low positive charge), $(EEE)_8$ (high negative charge) and $(QQE)_8$ (low negative charge) (see Materials & methods for details). Representative images for the penetration profiles of $(EEE)_8$ and $(KKK)_8$ are shown in Fig. 3B and C.

Also with those peptides, we observe a clear difference between the behavior of positively charged molecules and their negatively charged counterparts at the gel/buffer interface (white arrows in Fig. 3C). In Fig. 3D, the penetration profiles are shown for the four different peptides 60 min after insertion through inlet 2 (see Fig. S5† for profiles after 5 min). The two negatively charged peptides, $(EEE)_8$ and $(QQE)_8$, show a very similar behavior: they do not accumulate at the buffer-gel interface and their fluorescent intensity decreases as a function of the penetration depth as one would expect for diffusive transport according to Fick's law. $(KKK)_8$ and $(QQK)_8$ accumulate both at the gel/buffer interface, yet the intensity of this accumulation peak is higher for $(KKK)_8$ than for $(QQK)_8$. However, the distribution profile of those peptides within the gel region is comparable to the negatively charged peptides. In contrast to the dextrans, the accumulation propensity of the two positively charged peptide variants can now directly be compared. We measure an accumulation peak intensity of 105% for $(QQK)_8$ and 133% for $(KKK)_8$, respectively, compared to the fluorescent intensity of the peptides in the buffer compartment. It is reasonable to assume that the binding affinity of the strongly charged $(KKK)_8$ peptide to the ECM gel is larger than for the weakly charged $(QQK)_8$ peptide. Indeed, reducing the binding affinity in our model by an order of magnitude reproduces the decrease in the height of the accumulation peak observed in our *in vitro* experiments (Fig. 3A).

Charged molecules accumulate at the basolateral side of blood vessel walls

To better specify which subsection of the tissue is responsible for the charge selective accumulation of molecules, we repeat

the microinjection with the different peptide variants and perform a colocalization test with key components from blood vessels. Already 5 min post-injection, negatively charged $(EEE)_8$ peptides spread from the injection site into the surrounding connective tissue and, after 60 min, a spatially homogeneous fluorescence signal is obtained (Fig. 3E). In contrast, when the $(KKK)_8$ peptide is injected into the muscle an accumulation around blood vessels is observed already 5 min post-injection (Fig. 3F, white arrows). At the end of our observation time, *i.e.* 60 min after injection, this locally increased intensity can still be detected around the blood vessel and is concentrated in perivascular (cellular) spots. Large parts of the positively charged $(KKK)_8$ peptides also remain at the injection site but no accumulation is observed in other areas of the connective tissue. This suggests that the peptides do not interact with collagen I, the main component of the connective tissue, which is supported by *in vitro* experiments conducted with collagen I gels (see Fig. S6†). Compared to the FITC-label of the dextrans, the TAMRA-label of the peptides exhibits a much higher photostability, which allows for an investigation of the $(KKK)_8$ peptide localization by means of immunohistochemical staining.

Consistent with the results obtained by microfluidics, $(KKK)_8$ peptides penetrate the connective tissue and accumulate around blood vessels. The evaluation of the images obtained by immunostaining shows that the accumulation sites of peptides colocalize with collagen IV fibers which constitute the basal lamina of blood vessels and thereby indicate the localization of the basal lamina (Fig. 4A–D). CD31 positive endothelial cells, lining the interior surface of blood vessels, do not colocalize with $(KKK)_8$ (Fig. 4E and H) which suggests that the peptides encounter a barrier that prevents them from reaching the inner volume of the blood vessel. Immunostaining with TO-PRO 3, a marker for cell nuclei, demonstrates a cellular uptake of peptides already 5 min after injection; however, internalization of peptides by endothelial cells is not observed (Fig. 4). Moreover, positively charged $(KKK)_8$ peptides exhibit a strong affinity for muscle fibers (Fig. 4A and D) and unspecified fibrous components (Fig. 4E) of the interstitial space within the cremaster muscle. Immunostaining of samples obtained 60 min after microinjection (Fig. S7†) is consistent with the findings shown in Fig. 4.

Conclusion

Here, we have introduced a microfluidic chip which allows for quantifying the diffusive transport of molecules across a liquid/ECM interface. The results obtained with this *in vitro* setup are in good agreement with *in vivo* experiments performed in the cremaster muscle of mice. Our findings suggest that the selective permeability properties of the extracellular matrix layer surrounding blood vessels contribute to regulating the diffusive entry of nanoparticles and molecules from the blood stream into the connective tissue or *vice versa*. In conclusion, for an even better approximation of complex biological barriers in a microfluidics setup, both the cellular monolayer as well as the adjoining biopolymer matrix should be incorporated into the chip. Such an approach might even open new avenues for creating predictive penetration tests that help us gaining a better understanding of highly complex biological interfaces such as the blood–brain-barrier.

Experimental section

Microfluidic channel

Soft lithography was used to fabricate the microfluidic chips. The channel geometry was designed using AutoCAD (Autodesk, Munich, Germany) and the mask was printed at a resolution of 64 000 dpi (Zitzmann, Eching, Germany). The master was fabricated on a silicon wafer (Siegert Wafer, Aachen, Germany) with EpoCore (micro resist technology, Berlin, Germany) as a negative photoresist. After spin coating (Laurell, North Wales, USA) onto the silicon wafer for 35 s at

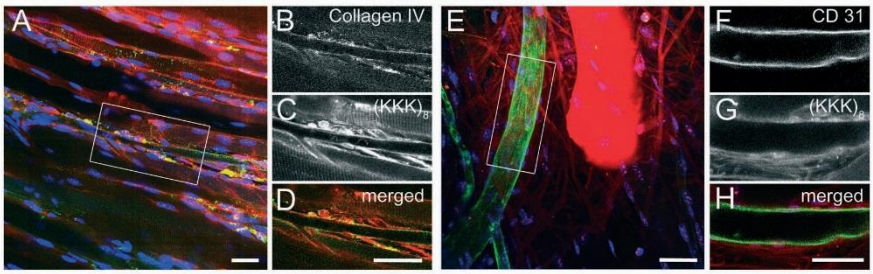

Fig. 4 Confocal immunofluorescence images of $(KKK)_8$ peptides 5 min after microinjection into the murine cremaster muscle. 20 optical slices each were used to obtain a 3-dimensional rendering of blood vessels (A, E). A single confocal *z*-plane from the regions indicated in (A) and (E) are shown in (B–D) and (F–H). The tissue is immunostained for cell nuclei (TO-PRO3, blue), collagen IV (green; Fig. 4A, B and D) and endothelial cells (CD31; green; Fig. 4E, F and H). The $(KKK)_8$ peptide (red) strongly colocalizes with collagen IV at the basolateral side of endothelial cells of blood vessels. Scale bar: 30 μm.

1000 rpm two prebake steps were conducted: first at 65 °C for 5 min, second at 95 °C for 10 min. After cooling down, the photoresist was exposed to UV light for 7 min to ensure cross-linking. Post-exposure baking were conducted at 65 °C for 5 min and subsequently at 95 °C for 20 min. The wafer was developed using mr-Dev 600 (micro resist technology, Berlin, Germany) to remove all remaining uncrosslinked photoresist. Finally, the master was rinsed with isopropanol to remove remaining developer. For the microfluidic channel fabrication Sylgard 184 (Dow Corning, Midland, MI, USA) elastomer was mixed at a 10 : 1 ratio with curing agent, degassed for 30 min, poured onto the master and cured at 80 °C for 1 h. The cured PDMS was peeled off and bonded to a glass slide using oxygen plasma at 20 W for 30 s. The bonded device was stored in an oven at 120 °C overnight to regain its hydrophobic properties.

ECM, dextrans and polypeptides

Growth factor reduced extracellular matrix gel (ECM) with a protein concentration of 7.37 mg mL^{-1} purified from the Engelbreth–Holm–Swarm sarcoma of mice was obtained from Sigma-Aldrich. For experiments, ECM was thawed on ice for several hours and afterwards a volume of 2 μL was inserted into the microfluidic device through inlet 1. Fluorescein isothiocyanate-diethylaminoethyl (FITC-DEAE) and fluorescein isothiocyanate-carboxymethyl (FITC-CM) dextrans with an average molecular weight of 4 kDa and 150 kDa, respectively, was obtained from Sigma-Aldrich and dissolved in PBS at a concentration of 10 mg mL^{-1}. Customized peptides were obtained from PEPperPRINT (Heidelberg, Germany) and used without further purification. The length of the customized peptides was chosen to match the molecular weight of the 4 kDa dextrans which leads to a peptide consisting of 24 amino acids. The diffusive transport of the peptides is evaluated by fluorescence microscopy, thus a carboxytetramethylrhodamine (TAMRA) label was conjugated to the N-termini of each peptide. In total, four different peptides were designed: a highly negatively charged, a highly positively charged, a moderate negatively charged, and a moderate positively charged peptide variant. The corresponding amino acid sequences are: TAMRA-$(EEE)_8$, TAMRA-$(KKK)_8$, TAMRA-$(QQE)_8$ and TAMRA-$(QQK)_8$. Here, E represents glutamic acid, K denotes lysine and Q denotes glutamine (according to the 1-letter amino acid coding). Glutamic acid has a molecular weight of 147.13 g mol^{-1}, and the free side-chain carboxylic acid group of this amino acid has a pK_a of 4.1. This results in a negatively charged group at physiological pH which is used in our experiments. Lysine has a molecular weight of 146.19 g mol^{-1}, and the pK_a of the side chain amino group is 10.5; as a consequence, this amino acid is positively charged at neutral pH. Glutamine has a molecular weight of 146.15 g mol^{-1} and a zwitterionic side chain. Glutamine therefore assumed to be net neutral at pH 7. For the experiments, the peptides were dissolved in PBS and used at a concentration of 1 mg mL^{-1}.

Buffer containing test molecules was carefully inserted into inlet 2 with a Hamilton syringe (1702 sleeve type), which ejects a volume of 0.33 μL per rotation. When the channel was completely filled with buffer the flow was stopped to match the *in vivo* situation where the test molecules are injected into the connective tissue. Thus, after a short time of equilibration no flow of test molecules is present.

Data acquisition and evaluation

Images were acquired with a digital camera (Orca Flash 4.0 C11440, Hamamatsu, Japan) using the software Hokawo provided by Hamamatsu on an AxioVert 200 (Zeiss, Oberkochen, Germany) microscope using a 4× objective (Zeiss, Oberkochen, Germany). The exposure time was chosen such that no pixel saturation occurred. Each of the six channels was analyzed individually with ImageJ. A rectangle with a height of 880 pixels corresponding to 2.75 mm and a width of 30 pixels (0.09 mm) was placed in the channel such that 50 (0.16 mm) pixels of this rectangle were located in the lower channel (Fig. 1B). This procedure allows us to account for the bleaching of the fluorescent label of the test molecules. Since no continuous flow was applied, the fluorophores in the buffer compartment are subjected to same rate of bleaching as the molecules within the ECM. Therefore, the fluorescence intensity in the buffer channel (calculated from the 50 pixels of the rectangle in the lower channel) was used as a reference to normalize the intensity in the finger-like structure. This ensures the comparability of the calculated intensity profiles at different time points during the experiments.

The intensity within the chosen rectangle was averaged per pixel line with a function implemented in ImageJ. Thus, one intensity value per line was obtained. In a next step, these average intensity values per line were averaged again, first over the six finger channels of a chip and then over three different microfluidic chips.

Animals and surgical procedure

Male C57BL/6 mice at the age of 10–12 weeks were purchased from Charles River (Sulzfeld, Germany). Animals were housed under conventional conditions with free access to food and water. All experiments were performed according to German legislation for the protection of animals. The surgical preparation was performed as described by Baez[31] with minor modifications. Briefly, mice were anesthetized by intraperitoneal injection of a ketamine/xylazine mixture (100 mg kg^{-1} ketamine and 10 mg kg^{-1} xylazine). The right cremaster muscle was exposed through a ventral incision of the scrotum. The muscle was opened ventrally in a relatively avascular zone, using careful electrocautery to stop any bleeding, and spread over the pedestal of a custom-made microscopy stage. Epididymis and testicle were detached from the cremaster muscle and placed into the abdominal cavity. Throughout the procedure as well as after surgical preparation during *in vivo* microscopy, the muscle was superfused with warm

buffered saline. The body temperature was maintained at 37 °C using a heating pad placed under the mouse. After *in vivo* microscopy, tissue samples of the cremaster muscle were prepared for immunohistochemistry. Anaesthetized animals were then euthanized by an intra-arterial pentobarbital overdose (Narcoren, Merial, Hallbergmoos, Germany).

In vivo microscopy

The setup for *in vivo* microscopy was centered around an VisiScope.A1 imaging system (Visitron Systems GmbH, Puchheim, Germany), equipped with a LED light source for fluorescence epi-illumination. For excitation of dextrans the 470 nm, for the excitation of peptides the 550 nm LED modules (exposure time 100 ms), and for transillumination the 655 nm LED module (exposure time 10 ms) were used in a fast simultaneous mode. Light was directed onto the specimen *via* a triple dichroic filter NC316973 (z 405/488/561 rpc; Chroma Technology Corp., Bellows Falls, VT, USA). Images were obtained with a water dipping objective (20×, NA 1.0). Light from the specimen was separated with a beam splitter (T 580 lpxxr Chroma Technology Corp., Bellows Falls, VT, USA) and acquired with two Rolera EM2 cameras and VisiView Imaging software (Visitron).

Microinjection of dextran and peptides

Local administration of 250 ± 100 pL of fluorescently labeled dextran (2 mg mL^{-1}) or peptides (1 mg mL^{-1}) into the cremaster muscle was performed *via* perivenular microinjection in regions at a distance of 25 to 50 μm from a postcapillary venule.[32] Venules with diameters ranging between 25 and 35 μm were selected for the experiments. Microinjection was performed under visual control of the intravital microscope, with a long distance air objective (20×, NA 0.4 Olympus), using borosilicate glass micropipettes (GB150TF-8P, Science Products GmbH, Hofheim, Germany) – pulled with a micropipette puller (PC 10, Narishige, London, United Kingdom) – which were connected to the injection system consisting of a micromanipulator (PatchStar Micromanipulator, Scientifica, Uckfield, United Kingdom) and a microinjector (FemtoJet, Eppendorf, Hamburg, Germany). The tip pressure during injection was 3000 hPa and the tip diameter <1 μm. The vessel and the surrounding tissue were visualized during a time period from 1 min to 60 min after injection.

Mice (n = 3 each group) received 150 kDa CM-dextran, 150 kDa DEAE-dextran, $(KKK)_8$ peptides and $(EEE)_8$ peptides *via* microinjection 20 min after the preparation of the cremaster muscle. The animals were randomly assigned to the experimental groups.

Immunostaining

To determine the charge dependent localization of peptides, immunostaining of the cremaster muscle was performed. After dissection, the tissue was fixed with 2% paraformaldehyde for 15 min at room temperature, then blocked and permeabilized in PBS, supplemented with 2% bovine serum albumin (Sigma Aldrich, Munich, Germany) and 0.5% Triton X-100 (Sigma Aldrich, Munich, Germany) for 1 h at room temperature. After incubation with a rabbit polyclonal Collagen IV antibody (ab6586, Abcam, Cambridge, UK) or rat anti mouse CD31 (Clone MEC 13.3, 553 370, BD Pharmingen, Heidelberg, Germany) at room temperature for 2 h, the tissues were washed with PBS and incubated with an Alexa-Fluor 488-linked goat anti-rabbit or Alexa-Fluor 488-linked goat anti-rat antibody (Life Technologies, Darmstadt, Germany) and TO-PRO3®-Iodide (Invitrogen, Carlsbad, CA, USA) for another 2 h at room temperature in the dark. Immunostained cremaster muscles were mounted in PermaFluor (Beckman Coulter, Krefeld, Germany) on glass slides. Images were obtained using a Leica SP5 confocal laser-scanning microscope, equipped with a GaAsP hybrid detection system (Leica HyD), with an oil-immersion lens (63×; NA 1.40; Leica Microsystems, Wetzlar, Germany). Images were processed with ImageJ software and figures for publication were assembled in Photoshop 9 (Adobe Systems, Mountain View, California, US).

Numerical simulations

For the simulation of molecular penetration across an ECM gel, we used a standard diffusion–reaction model in one dimension that includes the binding and unbinding processes to the gel (see ESI† for a detailed description). Two coupled partial differential equations were numerically solved by discretizing space and time. The solution was propagated stepwise in time by an Euler-forward scheme, with a fixed time step chosen to ensure numerical stability.

Funding sources

This work was supported by the Deutsche Forschungsgemeinschaft through project B7 "Nanoagents in 3-dimensional biopolymer hydrogels", project B10 "Spatiotemporal control of immune cell trafficking by multifunctional nanoconstructs *in vivo*" and project A3 "Spatially orchestrated stochastic enzyme kinetics in multienzyme complexes" in the framework of SFB 1032.

References

1 K. Y. Tsang, M. C. Cheung, D. Chan and K. S. Cheah, The developmental roles of the extracellular matrix: beyond structure to regulation, *Cell Tissue Res.*, 2010, **339**, 93–110.
2 S. M. Gabe, Gut barrier function and bacterial translocation in humans, *Clin. Nutr.*, 2001, **20**, 107–112.
3 O. Lieleg and K. Ribbeck, Biological hydrogels as selective diffusion barriers, *Trends Cell Biol.*, 2011, **21**, 543–551.
4 R. Cecchelli, V. Berezowski, S. Lundquist, M. Culot and M. Renftel, *et al.*, Modelling of the blood–brain barrier in drug discovery and development, *Nat. Rev. Drug Discovery*, 2007, **6**, 650–661.
5 E. Proksch, J. M. Brandner and J. M. Jensen, The skin: an indispensable barrier, *Exp. Dermatol.*, 2008, **17**, 1063–1072.

6 M. A. McGuckin, S. K. Linden, P. Sutton and T. H. Florin, Mucin dynamics and enteric pathogens, *Nat. Rev. Microbiol.*, 2011, **9**, 265–278.

7 B. J. Teubl, M. Absenger, E. Frohlich, G. Leitinger and A. Zimmer, *et al.*, The oral cavity as a biological barrier system: Design of an advanced buccal *in vitro* permeability model, *Eur. J. Pharm. Biopharm.*, 2013, **84**, 386–393.

8 A. M. Alkilany, A. Shatanawi, T. Kurtz, R. B. Caldwell and R. W. Caldwell, Toxicity and Cellular Uptake of Gold Nanorods in Vascular Endothelium and Smooth Muscles of Isolated Rat Blood Vessel: Importance of Surface Modification, *Small*, 2012, **8**, 1270–1278.

9 J. R. Turner, Intestinal mucosal barrier function in health and disease, *Nat. Rev. Immunol.*, 2009, **9**, 799–809.

10 K. Maruyama, O. Ishida, T. Takizawa and K. Moribe, Possibility of active targeting to tumor tissues with liposomes, *Adv. Drug Delivery Rev.*, 1999, **40**, 89–102.

11 S. K. Hobbs, W. L. Monsky, F. Yuan, W. G. Roberts and L. Griffith, *et al.*, Regulation of transport pathways in tumor vessels: Role of tumor type and microenvironment, *Proc. Natl. Acad. Sci. U. S. A.*, 1998, **95**, 4607–4612.

12 M. Simionescu, D. Popov and A. Sima, Endothelial transcytosis in health and disease, *Cell Tissue Res.*, 2009, **335**, 27–40.

13 T. M. Allen and P. R. Cullis, Drug delivery systems: Entering the mainstream, *Science*, 2004, **303**, 1818–1822.

14 O. Lieleg, R. M. Baumgärtel and A. R. Bausch, Selective Filtering of Particles by the Extracellular Matrix: An Electrostatic Bandpass, *Biophys. J.*, 2009, **97**, 1569–1577.

15 F. Arends, R. Baumgartel and O. Lieleg, Ion-specific effects modulate the diffusive mobility of colloids in an extracellular matrix gel, *Langmuir*, 2013, **29**, 15965–15973.

16 W. H. De Jong and P. J. A. Borm, Drug delivery and nanoparticles: Applications and hazards, *Int. J. Nanomed.*, 2008, **3**, 133–149.

17 L. G. Griffith and M. A. Swartz, Capturing complex 3D tissue physiology *in vitro*, *Nat. Rev. Mol. Cell Biol.*, 2006, **7**, 211–224.

18 E. Esch, A. Bahinski and D. Huh, Organs-on-chips at the frontiers of drug discovery, *Nat. Rev. Drug Discovery*, 2015, **14**, 248–260.

19 K. Ziolkowska, R. Kwapiszewski and Z. Brzozka, Microfluidic devices as tools for mimicking the *in vivo* environment, *New J. Chem.*, 2011, **35**, 979–990.

20 Z. Ma, S. Koo, M. A. Finnegan, P. Loskill and N. Huebsch, *et al.*, Three-dimensional filamentous human diseased cardiac tissue model, *Biomaterials*, 2014, **35**, 1367–1377.

21 Y. Kim, M. E. Lobatto, T. Kawahara, B. L. Chung and A. J. Mieszawska, *et al.*, Probing nanoparticle translocation across the permeable endothelium in experimental atherosclerosis, *Proc. Natl. Acad. Sci. U. S. A.*, 2014, **111**, 1078–1083.

22 D. Huh, B. D. Matthews, A. Mammoto, M. Montoya-Zavala and H. Y. Hsin, *et al.*, Reconstituting Organ-Level Lung Functions on a Chip, *Science*, 2010, **328**, 1662–1668.

23 L. Li, O. Lieleg, S. Jang, K. Ribbeck and J. Han, A microfluidic *in vitro* system for the quantitative study of the stomach mucus barrier function, *Lab Chip*, 2012, **12**, 4071–4079.

24 L. D. Li, T. Crouzier, A. Sarkar, L. Dunphy and J. Han, *et al.*, Spatial Configuration and Composition of Charge Modulates Transport into a Mucin Hydrogel Barrier, *Biophys. J.*, 2013, **105**, 1357–1365.

25 F. Arends, C. Nowald, K. Pflieger, K. Boettcher, S. Zahler and O. Lieleg, The Biophysical Properties of Basal Lamina Gels Depend on the Biochemical Composition of the Gel, *PLoS One*, 2015, **10**(2), e0118090.

26 C. J. Dowd, C. L. Cooney and M. A. Nugent, Heparan sulfate mediates bFGF transport through basement membrane by diffusion with rapid reversible binding, *J. Biol. Chem.*, 1999, **274**, 5236–5244.

27 E. G. Atkinson, S. Jones, B. A. Ellis, D. C. Dumonde and E. Graham, Molecular size of retinal vascular leakage determined by FITC-dextran angiography in patients with posterior uveitis, *Eye*, 1991, **5**(Pt 4), 440–446.

28 M. B. Voisin, D. Probstl and S. Nourshargh, Venular Basement Membranes Ubiquitously Express Matrix Protein Low-Expression Regions Characterization in Multiple Tissues and Remodeling during Inflammation, *Am. J. Pathol.*, 2010, **176**, 482–495.

29 R. G. Thorne, A. Lakkaraju, E. Rodriguez-Boulan and C. Nicholson, In vivo diffusion of lactoferrin in brain extracellular space is regulated by interactions with heparan sulfate, *Proc. Natl. Acad. Sci. U. S. A.*, 2008, **105**, 8416–8421.

30 S. Lelu, S. P. Strand, J. Steine and C. D. Davies, Effect of PEGylation on the Diffusion and Stability of Chitosan-DNA Polyplexes in Collagen Gels, *Biomacromolecules*, 2011, **12**, 3656–3665.

31 S. Baez, Open Cremaster Muscle Preparation for Study of Blood-Vessels by *in-vivo* Microscopy, *Microvasc. Res.*, 1973, **5**, 384–394.

32 S. Sellner, S. Kocabey, K. Nekolla, F. Krombach and T. Liedl, *et al.*, DNA nanotubes as intracellular delivery vehicles in vivo, *Biomaterials*, 2015, **53**, 453–463.

A.6 Supporting Information: A microfluidics approach to study the accumulation of molecules at basal lamina interfaces

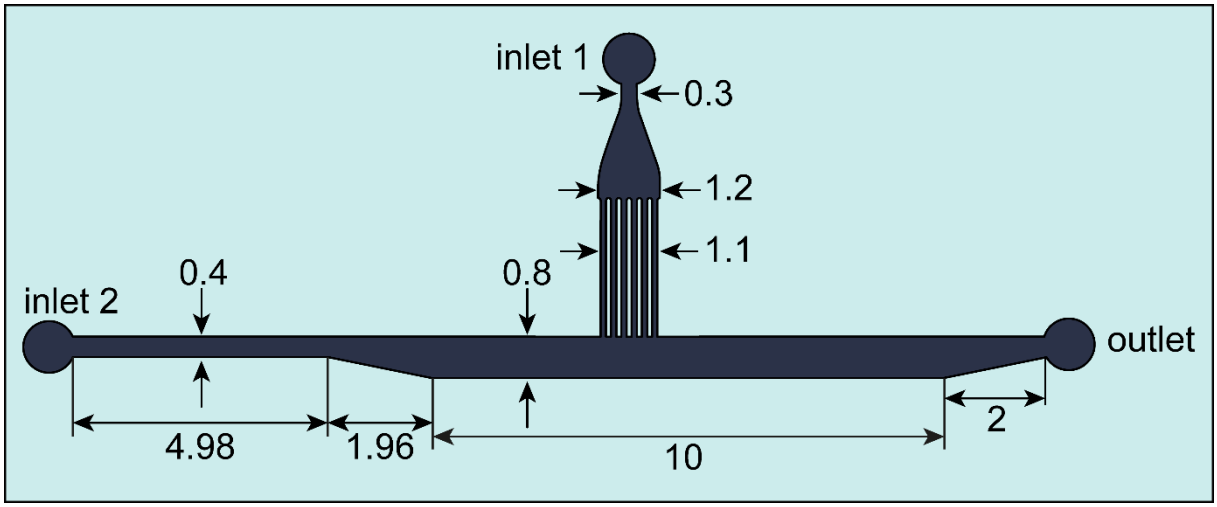

Figure S1. Detailed scheme of the microfluidic setup; all dimensions are given in mm.

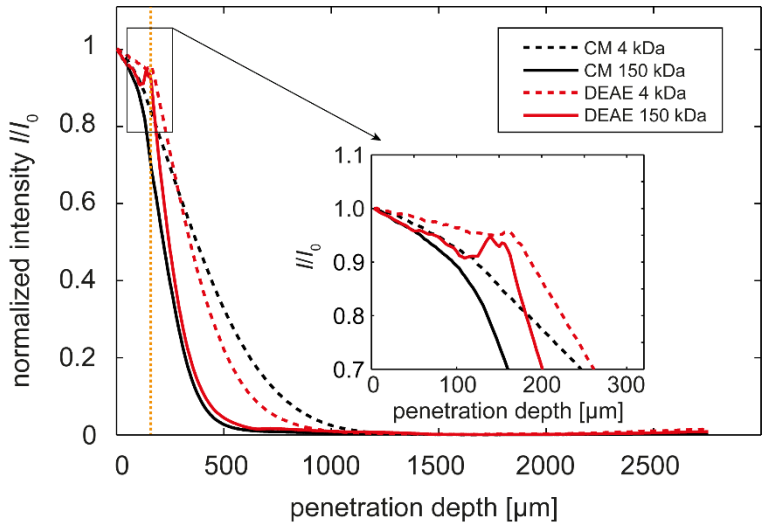

Figure S2. Intensity profiles for dextrans 5 min after insertion into the microfluidic channel. The 4 kDa dextrans (dashed lines) penetrate deeper into the channel than the 150 kDa variants. We observe a small accumulation peak at the ECM/buffer interface (marked by the orange dotted line) for both positively charged DEAE-dextrans (red dashed line 4 kDa, red line 150 kDa), whereas no accumulation is observed for the negatively charged CM-dextrans.

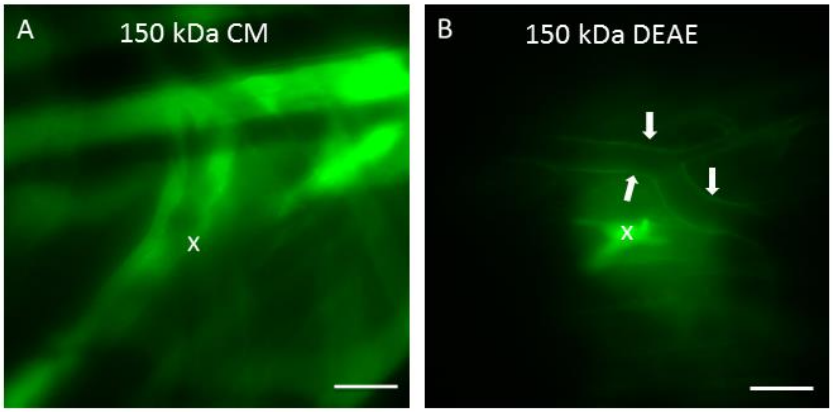

Figure S3. Fluorescence images showing the distribution of negatively charged CM (A) and positively charged DEAE (B) dextrans (MW = 150 kDa) 5 min after microinjection into the cremaster muscle of a mouse. The CM-dextrans rapidly spread from the injection site (white cross) next to muscle fibers (A) whereas the DEAE-dextrans accumulate around blood vessels (white arrows, B). Scale bar: 50 µm.

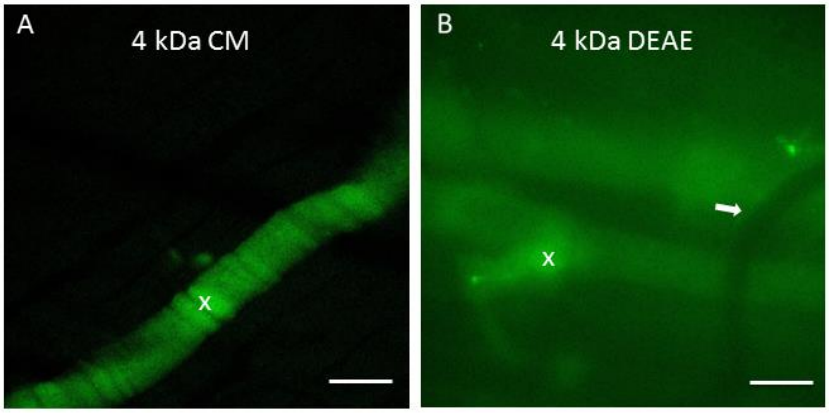

Figure S4. Fluorescence images showing the distribution of negatively charged CM (A) and positively charged DEAE (B) dextrans (MW = 4 kDa) 60 min after microinjection into the murine cremaster muscle. The CM-dextrans accumulate at the injection site (white cross) along muscle fibers (A) whereas the DEAE-dextrans remain in the interstitial space and around blood vessels (white arrows, B). Scale bar: 50 µm.

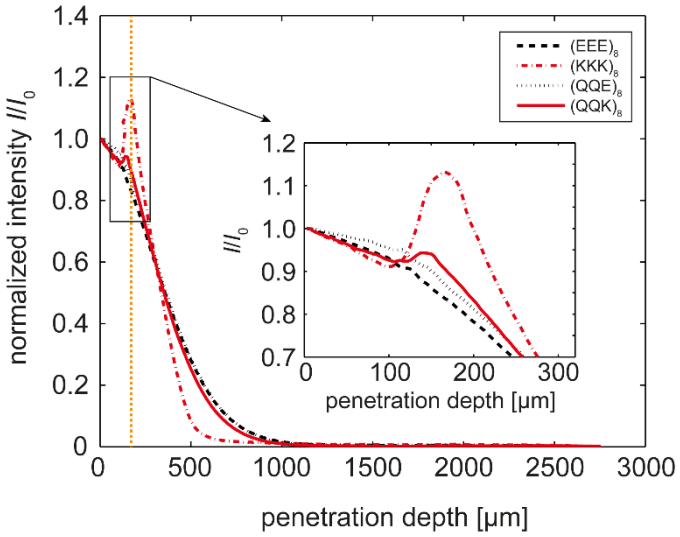

Figure S5. Intensity profiles for peptides 5 min after insertion into the microfluidic channel. The penetration profiles are similar for all peptide variants. For the $(QQK)_8$ peptides, we observe a small accumulation peak at the ECM/buffer interface (marked by the orange dotted line). We measure an accumulation peak intensity of 94 % of the channel intensity. For the higher positively charged $(KKK)_8$ peptides, the accumulation is stronger with a peak intensity of 113 %. Negatively charged $(EEE)_8$ and $(QQE)_8$ peptides show no accumulation at the interface.

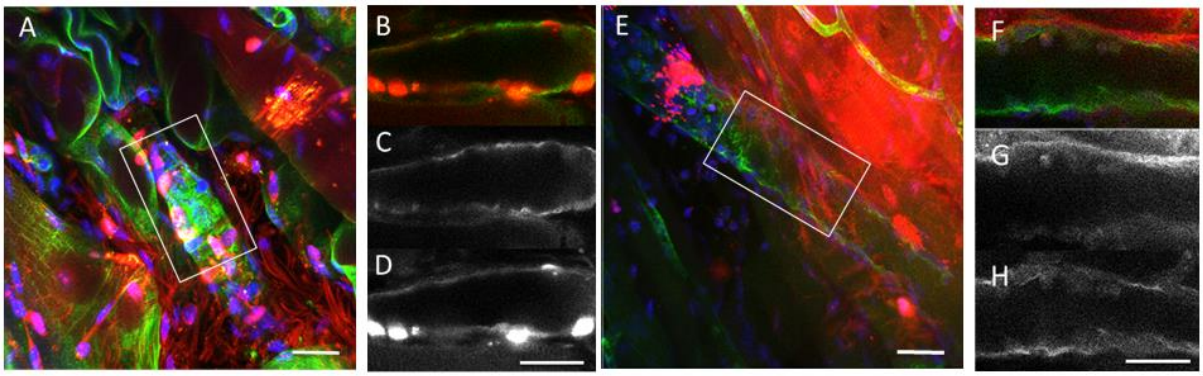

Figure S6. Confocal immunofluorescence images of $(KKK)_8$ peptides 60 min after microinjection into the murine cremaster muscle. (A) and (E) show 3D rendered images of 20 confocal z-planes (1 µm distance) of postcapillary venules in the muscle tissue. Single confocal z-planes from the regions indicated in (A) and (E) are shown in (B-D) and (F-H). Cell nuclei are depicted in blue (TO-PRO3), Collagen IV green (A, B and D) and CD31, which marks endothelial cells green in (E, F and H). The $(KKK)_8$ peptide (red A, B, D, E, F and G) co-localizes with collagen IV at the basolateral side of endothelial cells. Scale bar: 30 µm.

Simulation of diffusion and binding to the gel

As a general description of the diffusive process we used a standard reaction-diffusion model in one dimension that includes the binding and unbinding processes to the gel. We set up a system of two coupled partial differential equations for the time dependent evolution of the corresponding concentrations of the bound and the unbound part:

$$\frac{\partial c_u}{\partial t} = D\frac{\partial^2 c_u}{\partial x^2} + R$$
$$\frac{\partial c_b}{\partial t} = -R$$

Here, c_u and c_b denote the unbound and the bound concentration, respectively, and D is the diffusion coefficient. The reaction part $\pm R$ of the equations describes the binding to and the unbinding from the gel.

In the simulation, we assumed that a reservoir of infinite size with concentration $c_u = 1$ is coupled to a small intermediate buffer region at position $x = 0$. The gel extends from $x = 0.05$ to the right boundary at $x = L$, where we applied absorbing boundary conditions (i.e. an infinitely large reservoir of concentration $c_u = c_b = 0$). Since binding and unbinding rates are directly proportional to the corresponding concentrations we obtain linear reactions terms:

$$R = k^{off} c_b - k^{on} c_u$$

The rate constants for binding and unbinding are given by k^{on} and k^{off}, respectively. To take into account that both, binding and unbinding processes can only take place in the gel (i.e. in the region $0.05 < x < 1$), the rate constants have to be chosen such that:

$$k^{on} = k^{off} = 0 \text{ for } x < 0.05$$

By inserting the reaction part into the reaction-diffusion we obtain:

$$\frac{\partial c_u}{\partial t} = D \frac{\partial^2 c_u}{\partial x^2} + k^{off} c_b - k^{on} c_u \tag{1}$$

$$\frac{\partial c_b}{\partial t} = -k^{off} c_b + k^{on} c_u \tag{2}$$

These partial differential equations describe the full time evolution of the reaction-diffusion system in the gel. The total concentration is given by the sum of the bound and the unbound part:

$$c_{tot}(x,t) = c_u(x,t) + c_b(x,t)$$

For a numerical simulation of the reaction-diffusion model, the equations (1) and (2) have to be discretized in space and time. Therefore, a grid of N_x equally spaced points with distance $\Delta x = l / N_x$ is introduced. From considerations of numerical stability a fixed time step is chosen. The solution is propagated stepwise in time by an Euler-Forward scheme. The discretized equations read:

$$c_{u,j}^{k+1} = c_{u,j}^{k} + \Delta t \left(\frac{D}{\Delta x^2} \left[c_{u,j+1}^{k} - 2c_{u,j}^{k} + c_{u,j-1}^{k} \right] + k^{off} c_{b,j}^{k} - k^{on} c_{u,j}^{k} \right)$$

$$c_{b,j}^{k+1} = c_{b,j}^{k} + \Delta t \left(-k^{off} c_{b,j}^{k} + k^{on} c_{u,j}^{k} \right)$$

where $x = j\Delta x$ and $t = k\Delta t$. This was implemented in Matlab and calculated for the parameters shown in Table S1.

Table S1: Parameter choice for the calculation of penetration profiles.

Parameter	Value	Description
D	$2*10^{-5}$	Diffusion coefficient
k^{on}	(1) $2*10^{-4}$ (2) $2*10^{-5}$	on rate (red dash-dotted line in Fig. 3 of the main paper) on rate (red line in Fig. 3 of the main paper)
k^{off}	(1) $2*10^{-5}$ (2) $2*10^{-6}$	off rate (red dash-dotted line in Fig. 3 of the main paper) off rate (red line in Fig. 3 of the main paper)

The model allows for a continuous fast diffusion of molecules to the interface. However, when the molecules reach the interface, the binding affinity of the molecules to the gel results in a "slowed down" diffusion from the interface back into the buffer compartment due to binding events. This results in an effective asymmetric diffusion and gives rise to the concentration peak at the interface.

References

1. Proksch E, Brandner JM, Jensen JM (2008) The skin: an indispensable barrier. Experimental Dermatology 17: 1063-1072.
2. Teubl BJ, Absenger M, Frohlich E, Leitinger G, Zimmer A, et al. (2013) The oral cavity as a biological barrier system: Design of an advanced buccal in vitro permeability model. European Journal of Pharmaceutics and Biopharmaceutics 84: 386-393.
3. Rowlands BJ, Soong CV, Gardiner KR (1999) The gastrointestinal tract as a barrier in sepsis. British Medical Bulletin 55: 196-211.
4. McGuckin MA, Linden SK, Sutton P, Florin TH (2011) Mucin dynamics and enteric pathogens. Nature Reviews Microbiology 9: 265-278.
5. Cecchelli R, Berezowski V, Lundquist S, Culot M, Renftel M, et al. (2007) Modelling of the blood-brain barrier in drug discovery and development. Nature Reviews Drug Discovery 6: 650-661.
6. Lieleg O, Ribbeck K (2011) Biological hydrogels as selective diffusion barriers. Trends in Cell Biology 21: 543-551.
7. Alberts B, et al. (2002) Molecular Biology of the Cell: Garland Science.
8. Ballabh P, Braun A, Nedergaard M (2004) The blood-brain barrier: an overview - Structure, regulation, and clinical implications. Neurobiology of Disease 16: 1-13.
9. Tsang KY, Cheung MC, Chan D, Cheah KS (2010) The developmental roles of the extracellular matrix: beyond structure to regulation. Cell Tissue Res 339: 93-110.
10. Gabe SM (2001) Gut barrier function and bacterial translocation in humans. Clinical Nutrition 20: 107-112.
11. Yurchenco PD, Orear JJ (1994) Basal Lamina Assembly. Current Opinion in Cell Biology 6: 674-681.
12. Timpl R (1996) Macromolecular organization of basement membranes. Current Opinion in Cell Biology 8: 618-624.
13. Aumailley M (2013) The laminin family. Cell Adh Migr 7: 48-55.
14. Aumailley M, Pesch M, Tunggal L, Gaill F, Fassler R (2000) Altered synthesis of laminin 1 and absence of basement membrane component deposition in beta 1 integrin-deficient embryoid bodies. Journal of Cell Science 113: 259-268.
15. Khoshnoodi J, Pedchenko V, Hudson BG (2008) Mammalian collagen IV. Microscopy Research and Technique 71: 357-370.
16. Mouw JK, Ou G, Weaver VM (2014) Extracellular matrix assembly: a multiscale deconstruction. Nat Rev Mol Cell Biol 15: 771-785.
17. Kalluri R (2003) Basement membranes: structure, assembly and role in tumour angiogenesis. Nat Rev Cancer 3: 422-433.
18. Tilling T, Korte D, Hoheisel D, Galla HJ (1998) Basement membrane proteins influence brain capillary endothelial barrier function in vitro. Journal of Neurochemistry 71: 1151-1157.
19. Yanagishita M (1993) Function of Proteoglycans in the Extracellular-Matrix. Acta Pathologica Japonica 43: 283-293.
20. Iozzo RV (1998) Matrix proteoglycans: From molecular design to cellular function. Annual Review of Biochemistry 67: 609-652.
21. Kresse H, Schonherr E (2001) Proteoglycans of the extracellular matrix and growth control. Journal of Cellular Physiology 189: 266-274.
22. Allen TM, Cullis PR (2004) Drug delivery systems: Entering the mainstream. Science 303: 1818-1822.

23. Farokhzad OC, Langer R (2009) Impact of Nanotechnology on Drug Delivery. Acs Nano 3: 16-20.
24. Elsabahy M, Wooley KL (2012) Design of polymeric nanoparticles for biomedical delivery applications. Chem Soc Rev 41: 2545-2561.
25. Maruyama K, Ishida O, Takizawa T, Moribe K (1999) Possibility of active targeting to tumor tissues with liposomes. Advanced Drug Delivery Reviews 40: 89-102.
26. Hobbs SK, Monsky WL, Yuan F, Roberts WG, Griffith L, et al. (1998) Regulation of transport pathways in tumor vessels: Role of tumor type and microenvironment. Proceedings of the National Academy of Sciences of the United States of America 95: 4607-4612.
27. Kobayashi H, Watanabe R, Choyke PL (2014) Improving Conventional Enhanced Permeability and Retention (EPR) Effects; What Is the Appropriate Target? Theranostics 4: 81-89.
28. Benton G, Kleinman HK, George J, Arnaoutova I (2011) Multiple uses of basement membrane-like matrix BME/Matrigel) in vitro and in vivo with cancer cells. International Journal of Cancer 128: 1751-1757.
29. Petros RA, DeSimone JM (2010) Strategies in the design of nanoparticles for therapeutic applications. Nature Reviews Drug Discovery 9: 615-627.
30. Hughes CS, Postovit LM, Lajoie GA (2010) Matrigel: A complex protein mixture required for optimal growth of cell culture. Proteomics 10: 1886-1890.
31. Kleinman HK, Mcgarvey ML, Liotta LA, Robey PG, Tryggvason K, et al. (1982) Isolation and Characterization of Type-Iv Procollagen, Laminin, and Heparan-Sulfate Proteoglycan from the Ehs Sarcoma. Biochemistry 21: 6188-6193.
32. Kleinman HK, Mcgarvey ML, Hassell JR, Star VL, Cannon FB, et al. (1986) Basement-Membrane Complexes with Biological-Activity. Biochemistry 25: 312-318.
33. Lieleg O, Baumgärtel RM, Bausch AR (2009) Selective Filtering of Particles by the Extracellular Matrix: An Electrostatic Bandpass. Biophysical Journal 97: 1569-1577.
34. De Jong WH, Borm PJA (2008) Drug delivery and nanoparticles: Applications and hazards. International Journal of Nanomedicine 3: 133-149.
35. Esch E, Bahinski, A., Huh, D. (2015) Organs-on-chips at the frontiers of drug discovery. Nature Reviews Drug Discovery 14: 248-260.
36. Ziolkowska K, Kwapiszewski R, Brzozka Z (2011) Microfluidic devices as tools for mimicking the in vivo environment. New Journal of Chemistry 35: 979-990.
37. Ma Z, Koo S, Finnegan MA, Loskill P, Huebsch N, et al. (2014) Three-dimensional filamentous human diseased cardiac tissue model. Biomaterials 35: 1367-1377.
38. Kim Y, Lobatto ME, Kawahara T, Chung BL, Mieszawska AJ, et al. (2014) Probing nanoparticle translocation across the permeable endothelium in experimental atherosclerosis. Proceedings of the National Academy of Sciences of the United States of America 111: 1078-1083.
39. Huh D, Matthews BD, Mammoto A, Montoya-Zavala M, Hsin HY, et al. (2010) Reconstituting Organ-Level Lung Functions on a Chip. Science 328: 1662-1668.
40. Li L, Lieleg O, Jang S, Ribbeck K, Han J (2012) A microfluidic in vitro system for the quantitative study of the stomach mucus barrier function. Lab on a Chip 12: 4071-4079.
41. Li LD, Crouzier T, Sarkar A, Dunphy L, Han J, et al. (2013) Spatial Configuration and Composition of Charge Modulates Transport into a Mucin Hydrogel Barrier. Biophysical Journal 105: 1357-1365.
42. Kleinman HK, Martin GR (2005) Matrigel: Basement membrane matrix with biological activity. Seminars in Cancer Biology 15: 378-386.
43. Arends F, Nowald, C., Pflieger, K., Boettcher, K., Zahler, S. and Lieleg, O. (2015) The Biophysical Properties of Basal Lamina Gels Depend on the Biochemical Composition of the Gel. PLoS One.
44. Arends F, Baumgartel R, Lieleg O (2013) Ion-specific effects modulate the diffusive mobility of colloids in an extracellular matrix gel. Langmuir 29: 15965-15973.

45. Schuster BS, Suk JS, Woodworth GF, Hanes J (2013) Nanoparticle diffusion in respiratory mucus from humans without lung disease. Biomaterials 34: 3439-3446.
46. Hunter RJ (1989) Zeta Potential in Colloid Science: Principles and Applications: Academic Press.
47. Hiemenz P, Rajagopalan, R. (1997) Principles of Colloid and Surface Chemistry: CRC Press.
48. Einstein A (1905) Über die von der molekularkinetischen Theorie der Wärme geforderte Bewegung von in ruhenden Flüssigkeiten suspendierten Teilchen. Annalen der Physik 322: 549-560.
49. Qian H, Sheetz MP, Elson EL (1991) Single particle tracking. Analysis of diffusion and flow in two-dimensional systems. Biophys J 60: 910-921.
50. Hillborg H, Ankner JF, Gedde UW, Smith GD, Yasuda HK, et al. (2000) Crosslinked polydimethylsiloxane exposed to oxygen plasma studied by neutron reflectometry and other surface specific techniques. Polymer 41: 6851-6863.
51. Bhattacharya S, Datta A, Berg JM, Gangopadhyay S (2005) Studies on surface wettability of poly(dimethyl) siloxane (PDMS) and glass under oxygen-plasma treatment and correlation with bond strength. Journal of Microelectromechanical Systems 14: 590-597.
52. Kim J, Chaudhury MK, Owen MJ (2000) Hydrophobic recovery of polydimethylsiloxane elastomer exposed to partial electrical discharge. Journal of Colloid and Interface Science 226: 231-236.
53. Streuli C (1999) Extracellular matrix remodelling and cellular differentiation. Current Opinion in Cell Biology 11: 634-640.
54. Werb Z (1997) ECM and cell surface proteolysis: Regulating cellular ecology. Cell 91: 439-442.
55. Gu ZZ, Cui J, Brown S, Fridman R, Mobashery S, et al. (2005) A highly specific inhibitor of matrix metalloproteinase-9 rescues laminin from proteolysis and neurons from apoptosis in transient focal cerebral ischemia. Journal of Neuroscience 25: 6401-6408.
56. Wang CX, Shuaib A (2007) Critical role of microvasculature basal lamina in ischemic brain injury. Progress in Neurobiology 83: 140-148.
57. Kitajewski J (2011) Endothelial laminins underlie the tip cell microenvironment. Embo Reports 12: 1087-1088.
58. Timpl R, Brown JC (1994) The Laminins. Matrix Biology 14: 275-281.
59. Kang SH, Kramer JM (2000) Nidogen is nonessential and not required for normal type IV collagen localization in Caenorhabditis elegans. Mol Biol Cell 11: 3911-3923.
60. Murshed M, Smyth N, Miosge N, Karolat J, Krieg T, et al. (2000) The absence of nidogen 1 does not affect murine basement membrane formation. Mol Cell Biol 20: 7007-7012.
61. Schymeinsky J, Nedbal S, Miosge N, Poschl E, Rao C, et al. (2002) Gene structure and functional analysis of the mouse nidogen-2 gene: nidogen-2 is not essential for basement membrane formation in mice. Mol Cell Biol 22: 6820-6830.
62. Willem M, Miosge N, Halfter W, Smyth N, Jannetti I, et al. (2002) Specific ablation of the nidogen-binding site in the laminin gamma1 chain interferes with kidney and lung development. Development 129: 2711-2722.
63. Gresham HD, Graham IL, Griffin GL, Hsieh JC, Dong LJ, et al. (1996) Domain-specific interactions between entactin and neutrophil integrins - G2 domain ligation of integrin alpha(3)beta(1) and E domain ligation of the leukocyte response integrin signal for different responses. Journal of Biological Chemistry 271: 30587-30594.
64. Uria JA, Werb Z (1998) Matrix metalloproteinases and their expression in mammary gland. Cell Res 8: 187-194.
65. Sires UI, Griffin GL, Broekelmann TJ, Mecham RP, Murphy G, et al. (1993) Degradation of entactin by matrix metalloproteinases. Susceptibility to matrilysin and identification of cleavage sites. J Biol Chem 268: 2069-2074.

66. Lai SK, Wang YY, Hanes J (2009) Mucus-penetrating nanoparticles for drug and gene delivery to mucosal tissues. Adv Drug Deliv Rev 61: 158-171.
67. Lieleg O, Vladescu I, Ribbeck K (2010) Characterization of Particle Translocation through Mucin Hydrogels. Biophysical Journal 98: 1782-1789.
68. Xu QG, Boylan NJ, Suk JS, Wang YY, Nance EA, et al. (2013) Nanoparticle diffusion in, and microrheology of, the bovine vitreous ex vivo. Journal of Controlled Release 167: 76-84.
69. Jeong B, Bae YH, Kim SW (2000) Drug release from biodegradable injectable thermosensitive hydrogel of PEG-PLGA-PEG triblock copolymers. Journal of Controlled Release 63: 155-163.
70. Vila A, Gill H, McCallion O, Alonso MJ (2004) Transport of PLA-PEG particles across the nasal mucosa: effect of particle size and PEG coating density. Journal of Controlled Release 98: 231-244.
71. Manning GS (1969) Limiting Laws and Counterion Condensation in Polyelectrolyte Solutions .I. Colligative Properties. Journal of Chemical Physics 51: 924-933.
72. von Stockar U (2013) Biothermodynamics: The role of Thermodynamics in Biochemical Engineering.
73. Rant U, Arinaga K, Fujiwara T, Fujita S, Tornow M, et al. (2003) Excessive counterion condensation on immobilized ssDNA in solutions of high ionic strength. Biophysical Journal 85: 3858-3864.
74. Hofmeister F (1888) Zur Lehre von der Wirkung der Salze. Archiv für experimentelle Pathologie und Pharmakologie 25: 1-30.
75. Lo Nostro P, Ninham BW (2012) Hofmeister Phenomena: An Update on Ion Specificity in Biology. Chemical Reviews 112: 2286-2322.
76. Kunz W (2010) Specific ion effects in colloidal and biological systems. Current Opinion in Colloid & Interface Science 15: 34-39.
77. Hess B, van der Vegt NFA (2009) Cation specific binding with protein surface charges. Proceedings of the National Academy of Sciences of the United States of America 106: 13296-13300.
78. Heyda J, Hrobarik T, Jungwirth P (2009) Ion-Specific Interactions between Halides and Basic Amino Acids in Water. Journal of Physical Chemistry A 113: 1969-1975.
79. Aziz EF, Ottosson N, Eisebitt S, Eberhardt W, Jagoda-Cwiklik B, et al. (2008) Cation-specific interactions with carboxylate in amino acid and acetate aqueous solutions: X-ray absorption and ab initio calculations. Journal of Physical Chemistry B 112: 12567-12570.
80. Uejio JS, Schwartz CP, Duffin AM, Drisdell WS, Cohen RC, et al. (2008) Characterization of selective binding of alkali cations with carboxylate by x-ray absorption spectroscopy of liquid microjets. Proceedings of the National Academy of Sciences of the United States of America 105: 6809-6812.
81. Binnig G, Quate CF, Gerber C (1986) Atomic force microscope. Phys Rev Lett 56: 930-933.
82. Colton RJ, Baselt DR, Dufrene YF, Green JB, Lee GU (1997) Scanning probe microscopy. Curr Opin Chem Biol 1: 370-377.
83. Tsao YH, Evans DF, Wennerstrom H (1993) Long-range attractive force between hydrophobic surfaces observed by atomic force microscopy. Science 262: 547-550.
84. Burnham NA, Colton RJ (1989) Measuring the nanomechanical properties and surface forces of materials using an atomic force microscope. Journal of Vacuum Science & Technology A 7: 2906-2913.
85. Stetter FW, Cwiklik L, Jungwirth P, Hugel T (2014) Single lipid extraction: the anchoring strength of cholesterol in liquid-ordered and liquid-disordered phases. Biophys J 107: 1167-1175.
86. Rounsevell R, Forman JR, Clarke J (2004) Atomic force microscopy: mechanical unfolding of proteins. Methods 34: 100-111.

87. Galbraith CG, Skalak R, Chien S (1998) Shear stress induces spatial reorganization of the endothelial cell cytoskeleton. Cell Motil Cytoskeleton 40: 317-330.
88. Gouverneur M, Spaan JAE, Pannekoek H, Fontijn RD, Vink H (2006) Fluid shear stress stimulates incorporation of hyaluronan into endothelial cell glycocalyx. H458-H452 p.
89. Bai K, Wang W (2014) Shear stress-induced redistribution of the glycocalyx on endothelial cells in vitro. Biomechanics and Modeling in Mechanobiology 13: 303-311.
90. Zeng Y, Tarbell JM (2014) The adaptive remodeling of endothelial glycocalyx in response to fluid shear stress. PLoS One 9: e86249.

Acknowledgements

Ich möchte mich herzlich bei allen bedanken, die zum Gelingen dieser Arbeit beigetragen haben. Besonderer Dank gebührt:

- Prof. Lieleg für die Möglichkeit in seiner Gruppe diese Arbeit anzufertigen und dafür, dass er das Risiko eingegangen ist, eine Theoretikerin ohne praktische Erfahrungen anzustellen. Es war toll, dass seine Tür immer für Fragen und Diskussionen offen war.
- Tin für die vielen Diskussionen und seinem ewigen Versuch mir die Biochemie näher zu bringen.
- Benni für die harten Kickerspiele und für die Verbesserung meiner Boulderfähigkeiten.
- Der gesamten Arbeitsgruppe für viel Spaß, Feedback und tollen Diskussionen.
- Krackina für die gemeinsamen Stunden im Quietroom.

Zum Schluss möchte ich mich noch bei Vreni bedanken. Du bist der wichtigste Mensch in meinem Leben und ich bin unendlich glücklich, dass ich dich habe.

List of publications

- B. Käsdorf, **FA**, O. Lieleg,
  Diffusion regulation in the vitreous humor,
  Biophysical Journal, **109**, 2171-2181, doi: 10.1016/j.bpj.2015.10.002 (2015)

- **FA**, S. Sellner, P. Seifert, U. Gerland, M. Rehberg, O. Lieleg,
  A microfluidics approach to study the accumulation of molecules at basal lamina interfaces,
  Lab on a Chip, **15**, 3326-3334, doi: 10.1039/C5LC00561B (2015)

- **FA**, C. Nowald, K. Pflieger, K. Boettcher, S. Zahler, O. Lieleg,
  The biophysical properties of basal lamina gels depend on the biochemical composition of the gel
  PLoS ONE 10(2): e0118090. doi: 10.1371/journal.pone.0118090 (2015)

- **FA**, R. Baumgärtel, O. Lieleg,
  Ion-specific effects modulate the diffusive mobility of colloids in an extracellular matrix gel,
  Langmuir, 29, 15965-15973, doi: 10.1021/la404016y (2013)